





**LEONID DOROGIN**

Structural and  
tribological properties  
of zero- and one-dimensional  
nanocrystals



Institute of Physics, Faculty of Science and Technology, University of Tartu, Estonia.

#### Dissertation in Material Science

The dissertation was admitted on May 6, 2012 in partial fulfillment of the requirements for the degree of Doctor of Philosophy (material science), and allowed for defense by the Scientific Council on Material Science of the Faculty of Science and Technology of the University of Tartu.

#### Supervisors:

Dr. Ilmar Kink, Institute of Physics, University of Tartu;  
Prof. Dr. Alexey Romanov, Institute of Physics, University of Tartu.

#### Opponents:

Dr. Sci. Karim Mynbaev, Ioffe Physical-Technical Institute  
of the Russian Academy of Sciences, Saint-Petersburg, Russia;

Ass. Prof. Dr. Arvo Mere, Faculty of Science,  
Department of Physics, Tallinn University of Technology, Tallinn,  
Estonia.

Defense: June 29, 2012, University of Tartu (Tartu, Estonia).

This work has been /partially/ supported by Graduate School „Functional materials and technologies“ receiving funding from the European Social Fund under project 1.2.0401.09–0079 in University of Tartu, Estonia



European Union  
European Social Fund



Investing in your future

ISSN 2228–0928

ISBN 978–9949–32–022–6 (trükis)

ISBN 978–9949–32–023–3 (PDF)

Autoriõigus: Leonid Dorogin, 2012

Tartu Ülikooli Kirjastus

[www.tyk.ee](http://www.tyk.ee)

Tellimus nr. 244

# CONTENTS

LIST OF ORIGINAL PUBLICATIONS .....	7
ABBREVIATIONS .....	9
PREFACE .....	10
1. BACKGROUND .....	12
1.1. Experimental observation, structure and morphology of pentagonal multiply-twinned nanocrystals .....	12
1.2. Disclination model of pentagonal nanocrystals .....	14
1.2.1. Disclination model of pentagonal nanorod .....	14
1.2.2. Disclination model of icosahedral nanoparticle .....	16
1.3. Relaxation of mechanical stresses in pentagonal nanocrystals .....	18
1.4. Friction at the nanoscale and experimental manipulation of nanocrystals .....	21
1.5. Simulation of nanomanipulations for tribological studies .....	24
1.6. Elastic beam theory for modeling of nanowires .....	28
1.7. Coupling of elastic and tribological properties of nanowires on flat substrate .....	30
2. AIM OF THE STUDY .....	32
3. STRUCTURAL PROPERTIES OF PENTAGONAL 0D AND 1D NANOCRYSTALS .....	33
3.1. Pentagonal nanorods with crystal lattice mismatch layer .....	33
3.1.1. Solution for disclination in two-phase cylinder. Stresses and energy .....	35
3.1.2. Solution for cylinder with mismatched phases. Stresses and energy .....	38
3.1.3. Conditions for mismatched crystal lattice layer formation in PNR .....	39
3.1.4. The role of core/shell interface energy .....	41
3.1.5. Threshold radius for mismatched crystal lattice layer formation in PNR .....	41
3.2. Pentagonal nanoparticles with crystal lattice mismatch layer .....	43
3.2.1. Solution for distributed disclination in two-phase spheroid. Stresses and energy .....	44
3.2.2. Solution for spheroid with crystal lattice mismatched layer. Stresses and energy .....	46
3.2.3. Conditions for mismatched layer formation in INP .....	47
3.2.4. Threshold radius for mismatched crystal lattice layer formation in INP .....	48
3.3. Nanowhisker growth triggered by disclination .....	49
3.3.1. Single dislocation loop in presence of a disclination source ...	50

3.3.2. A pair of dislocation loops in presence of a disclination source .....	53
3.4. Summary .....	55
4. TRIBOLOGICAL PROPERTIES OF 0D AND 1D NANOCRYSTALS..	57
4.1. Simulation of icosahedral nanoparticles manipulation.....	57
4.1.1. Computer program for numerical simulation .....	57
4.1.2. Results of the simulations .....	59
4.2. Nanomanipulation experimental setup and force sensor.....	61
4.3. Manipulation of nanoparticles employed for tribological measurements .....	63
4.3.1. Manipulation of gold nanoparticles in SEM .....	63
4.3.2. Structure and tribology of gold nanoparticles .....	66
4.4. Manipulation of nanowires employed for tribological measurements .....	69
4.4.1. Half-suspended nanowire loaded at the end.....	70
4.4.2. Young modulus measurements for ZnO nanowires .....	71
4.4.3. Nanowire loaded at the midpoint and balanced by uniformly distributed kinetic friction forces .....	73
4.4.4. Measurement of kinetic friction of ZnO nanowires on a flat surface .....	74
4.4.5. Nanowire loaded at the end and balanced by combined distributed kinetic and static friction forces .....	76
4.4.6. Combined measurements of the kinetic and static friction forces of a ZnO nanowire on a flat surface .....	78
4.4.7. Nanowire self-balanced by distributed static friction forces on a flat surface .....	82
4.4.8. Measurements of a self-balanced ZnO nanowire static friction on a flat surface .....	84
4.5. Summary .....	88
MAIN RESULTS AND CONCLUSION.....	91
SUMMARY IN ESTONIAN .....	95
REFERENCES.....	96
ACKNOWLEDGEMENTS .....	101
APPENDIX .....	102
PUBLICATIONS .....	109

## LIST OF ORIGINAL PUBLICATIONS

- I. L.M. Dorogin, A.L. Kolesnikova, A.E. Romanov, “Misfit layer formation in icosahedral nanoparticles”, *Technical Physics Letters*, Vol. 34 (2008), pp. 779–781, DOI: 10.1134/S1063785008090198.
- II. L.M. Dorogin, S. Vlassov, A.L. Kolesnikova, I. Kink, R. Löhmus, A.E. Romanov, “Crystal mismatched layers in pentagonal nanorods and nanoparticles”, *Physica Status Solidi (b)*, Vol. 247 (2010), pp. 288–298, DOI: 10.1002/pssb.200945385.
- III. L.M. Dorogin, S. Vlassov, A.L. Kolesnikova, I. Kink, R. Löhmus, A.E. Romanov, “Pentagonal nanorods and nanoparticles with mismatched shell layers”, *Journal of Nanoscience and Nanotechnology*, Vol. 10 (2010), pp. 6136–6143, DOI: 10.1166/jnn.2010.2563.
- IV. S. Vlassov, B. Polyakov, L.M. Dorogin, A. Löhmus, A.E. Romanov, I. Kink, E. Gnecco, R. Löhmus, “Real-time manipulation of gold nanoparticles inside a scanning electron microscope”, *Solid State Communications*, Vol. 151 (2011), pp. 688–692, DOI: 10.1016/j.ssc.2011.02.020.
- V. B. Polyakov, L.M. Dorogin, S. Vlassov, I. Kink, A. Löhmus, A.E. Romanov, R. Lohmus, “Real-time measurements of sliding friction and elastic properties of ZnO nanowires inside a scanning electron microscope”, *Solid State Communications*, Vol. 151 (2011), pp. 1244–1247, DOI: 10.1016/j.ssc.2011.05.045.
- VI. L.M. Dorogin, B. Polyakov, A. Petruhins, S. Vlassov, R. Löhmus, I. Kink, A.E. Romanov, “Modeling of kinetic and static friction between an elastically bent nanowire and a flat surface”, *Journal of Materials Research*, Vol. 27 (2012), pp. 580–585, DOI: 10.1557/jmr.2011.339.
- VII. A.E. Romanov, A.A. Vikarchuk, A.L. Kolesnikova, L.M. Dorogin, I. Kink, E.C. Aifantis, “Structural transformations in nano- and microobjects triggered by disclinations”, *Journal of Materials Research*, Vol. 27 (2012), pp. 545–551, DOI: 10.1557/jmr.2011.372.
- VIII. B. Polyakov, L. M. Dorogin, A. Löhmus, A. E. Romanov and R. Löhmus “In situ measurement of the kinetic friction of ZnO nanowires inside a scanning electron microscope”, *Applied Surface Science*, Vol. 258 (2012), pp. 3227–3231, DOI: 10.1016/j.apsusc.2011.11.069.
- IX. B. Polyakov, L. M. Dorogin, S. Vlassov, A. E. Romanov and R. Löhmus, “Simultaneous measurement of static and kinetic friction of ZnO nanowires in situ a Scanning Electron Microscope”, *Micron* (2012) in press, DOI:10.1016/j.micron.2012.01.009.

### Author’s contribution

Papers I, II and III: the author is responsible for theoretical analysis and calculations.

Paper IV: the author has programmed software for manipulation and force registration, and has performed theoretical estimations.

Paper V: the author has performed theoretical calculations of the elastic and friction properties.

Paper VI: the author has developed the theoretical model and performed the calculations.

Paper VII: the author is responsible for the theoretical calculations of micro-/nano- whiskers formation.

Paper VIII and IX: the author has developed the theoretical model and carried out the theoretical calculation of static and kinetic friction.

## ABBREVIATIONS

AFM	atomic force microscopy
CNT	carbon nanotube
DMT	Derjaguin-Muller-Toporov
DNP	decahedral nanoparticle
EBT	elastic beam theory
FCC	face centered cubic
INP	icosahedral nanoparticle
JKR	Johnson-Kendall-Roberts
NC	nanocrystal
NP	nanoparticle
NW	nanowire
PNC	pentagonal nanocrystal
PNP	pentagonal nanoparticle
PNR	pentagonal nanorod
PP	pentagonal particle
PR	pentagonal rod
QTF	quartz tuning fork
SEM	scanning electron microscope
TB	twin boundary

## PREFACE

The present dissertation is related to a set of important research fields: theory of defects in solid matter, nanotribology and nanomechanics. Nevertheless, the topics of the research are strongly linked together. Each part is dedicated to the common goal of investigation of external and internal mechanical properties of nanocrystals (NCs). Therefore the research can be considered as multidisciplinary.

The “pivot” connecting all the topics are crystalline objects having 3 nanometer sized dimensions (so-called 0D nanocrystal, nanoparticle) and 2 nanometer sized dimensions (1D nanocrystal, nanorod, nanowire), whereas the other dimensions are macroscopic. Intrinsic and exterior properties of the both kinds are often closely related to each other. Thus the consideration of 0D and 1D nanostructures in a pair is rather reasonable.

Among various kinds of nanostructures, so-called multiply-twinned pentagonal nanoparticles and nanorods appealed the author’s interest. Due to specific internal crystalline structure and morphology, these objects possess remarkable properties that are important from both fundamental and practical points of view. In particular, structural transformations in pentagonal nanocrystals (PNCs) had been theoretically predicted in 80’s and then experimentally observed. The first part of the thesis is dedicated to the theoretical analysis of certain pathways of such structural transformations.

Nanoscale materials have extremely high surface-to-volume ratio in comparison with bulk materials. The influence of NC’s surface on physical properties can hardly be overestimated. Therefore investigation of interfacial and surface phenomena in 0D and 1D NCs is of crucial importance for modern materials science and technology. Particularly, friction at the nanoscale (i.e. nanotribology) is one of the most significant fields of research in nanoscience and nanotechnology. The attention in the second part of the thesis is called to the problems of nanotribology in application to nanoparticles and nanowires. Frictional properties were investigated by various methods – numerical simulation, experiments and consequent theoretical interpretation of the results with use of *ad hoc* models.

The dissertation is divided into 4 chapters.

The first chapter gives a brief overview of experimental methods and theoretical models that lie in the basement of the conducted research. That includes the experimental observation of PNCs, the disclination model, nanoscale friction and nanomanipulations, elastic beam theory used for modeling of nanowires.

The chapter 2 presents the aims of the research described in the dissertation.

The chapter 3 invokes the properties of pentagonal zero- and one-dimensional nanocrystals related to their specific structure. In particular, PNRs and INPs are theoretically investigated in the framework of the disclination model. Two possible mechanism of stress relaxation in them are proposed: formation crystal lattice mismatch layer and growth of a whisker on the surface.

The chapter 4 deals with certain tribological properties of zero- and one-dimensional nanocrystals. Theoretical simulation of INP during manipulation is discussed. Then the nanomanipulation experimental setup elaborated in the Institute of Physics is presented, followed by description of the manipulation experiments performed. The experimental manipulations of both NPs and NWs are presented together with theoretical models and discussions.

Finally, the last section summarizes all the results and provides the conclusions for the thesis.

# I. BACKGROUND

## I.1. Experimental observation, structure and morphology of pentagonal multiply-twinned nanocrystals

In physics of solid state matter it is well known that the size of the physical object is an important characteristic substantially determining its properties. Nearly each physical phenomenon has its own critical size beyond which the main characteristics of the observed phenomenon start to change drastically. Such properties are usually considered to be size effects. In this section one of the most specific size effects is considered, i.e. the formation of five-fold symmetry axis in NCs, which is forbidden according to the classic laws of crystallography [1].

Crystalline materials with face-centered cubic (FCC) crystal structure often demonstrate morphologies with axes of five-fold (pentagonal) symmetry. Micro- and nano-size crystals with such morphologies are under investigation for more than four decades. The most recent experimental results can be found in [2–6]. For example, Hofmeister in [2] studied the structure of silver pentagonal nanorods and nanoparticles, whereas Koga and Sugawara [4] showed a large fraction of decahedral and icosahedral gold particles against usual FCC morphology at the nanoscale range of sizes.

The origin of pentagonal symmetry in PNRs and PNPs follows from the schematics given in Fig. 1. As shown in Fig. 1a PNR is a polycrystal consisting of five FCC monocrystalline regions divided by five twin boundaries (TBs). Lateral faces of this multiple-twinned PNR are crystallographic planes of  $\{100\}$ -type, whereas cup faces are of  $\{111\}$ -type. The axis of fivefold symmetry is parallel to  $\langle 100 \rangle$ -type direction. The internal structure of PNRs can be understood from the schematics of Figs. 1b,c [7]. In the top-view of Fig. 1b five undistorted parts of the PNR are aligned along four TBs, which in FCC crystals are  $\{111\}$ -type planes, see, for example [1]. Because of FCC crystal geometry there is a small angular gap  $\omega$  preventing the formation of a completely connected and undistorted PNR. This angular gap however can be eliminated by mutual rotation of the gap faces with the formation of the fifth TB. It leads to the so-called *disclination model* of PNR [1, 7–9] that will be considered in details below.

In the case of PNPs, the standard morphology is an icosahedra with  $\{111\}$ -type crystallographic facets only [8, 9]. Here and below PNP will be considered only icosahedral and referred to as an icosahedral nanoparticle. The intrinsic structure of INP is comprised of 20 monocrystalline regions divided by TBs. FCC crystallographic structure requires those regions to be strictly tetrahedral to form TBs. However the icosahedral shape dictates the regions to be slightly different from tetrahedrons. The geometry of icosahedron and 20 exact tetrahedron assembled to form an icosahedron are depicted in Fig. 1e and 1f. Appearance of a solid angular gap is obvious. The angular gap can be eliminated by

rotational procedures in a way similar to PNRs in the framework of the *disclination model*.

PNRs and PNPs share the property of having “inconsistency” of the crystallographic structure and morphology that was evidenced by the appearance of angular gaps. Since PNCs have a closed structure and the angular gaps are not present, and if one assumes that monocrystalline regions preserve FCC crystal lattice, PNCs must be strained in order to eliminate the angular gaps. The procedure of elimination of angular gaps by rotations of gap faces is equivalent to the introducing a *disclination* defect into the crystal. The disclination model enables to explain the morphology and structure of PNCs and investigate their mechanical properties.

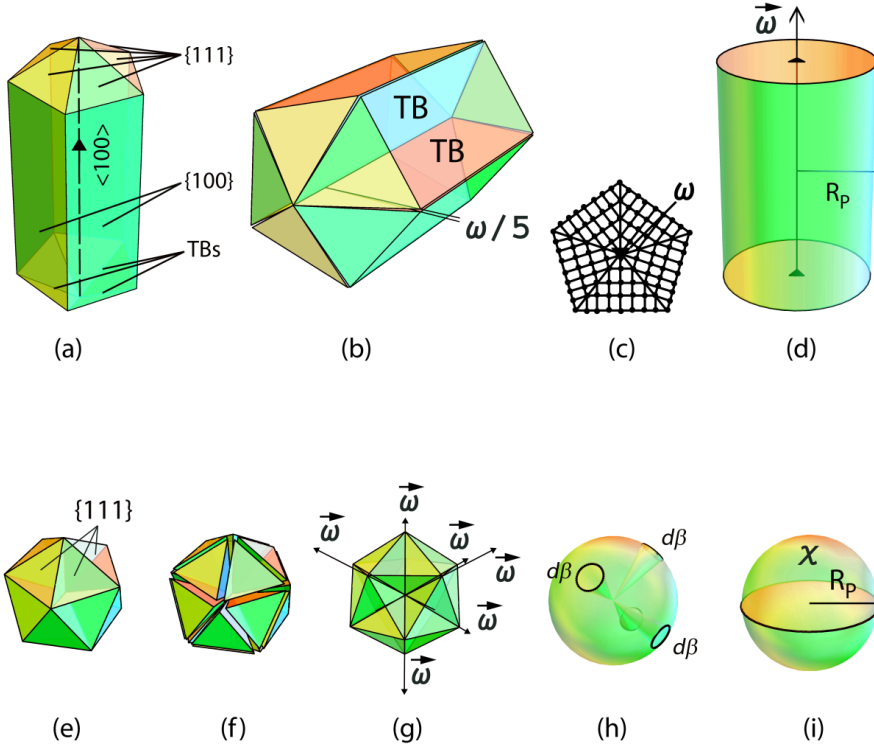


**Figure 1.** Disclination models for PNRs and PNPs: (a) PNR with internal twin boundaries, (b) angular gap  $\omega$  in a PNR, (c) twinned crystal lattice of PNR, (d) PNR modeled as cylinder of radius  $R_p$  having positive wedge disclination of strength  $\omega$ , (e) icosahedral NP, (f) INP with solid angle deficiency, (g) INP with six wedge disclinations of strength  $\omega$ , (h) INP with infinitesimal solid cones  $d\beta$ , (i) INP modeled as spheroid with eigenstrain components  $\varepsilon^*_{\theta\theta}=\varepsilon^*_{\varphi\varphi}$  of magnitude  $\chi$ .

## 1.2. Disclination model of pentagonal nanocrystals

### 1.2.1. Disclination model of pentagonal nanorod

Disclination is a linear defect in solid materials. Together with dislocation it belongs to the 6 elementary distortions introduced by Vito Volterra back in 1905. In the Fig. 2 the entire set of Volterra's distortions is presented and the corresponding types of defect are named. The procedure of making a Volterra's defect starts from an undistorted hollowed cylinder. Then a cut is done in through the cylinder's axis. The axis of the cylinder defines the defect line  $\mathbf{l}$ . The faces of the cut may undergo different kinds of displacements which determine the type of the defect.

Three translational displacements along the vector  $\mathbf{b}$  are possible (Fig. 2a-c) that correspond to edge and screw dislocation with Burgers vector  $\mathbf{b}$ . In addition, three rotational displacements can be made as shown in Fig. 2d-f. They are called *disclinations* and characterized by vector  $\boldsymbol{\omega}$  (Frank's vector). Burgers vector  $\mathbf{b}$  together with the line vector  $\mathbf{l}$ , or Frank vector  $\boldsymbol{\omega}$  together with the line vector  $\mathbf{l}$  define a dislocation or disclination, respectively. The concept of wedge disclination (Fig. 2f) is primarily important for the disclination model of PNCs and used throughout the dissertation.

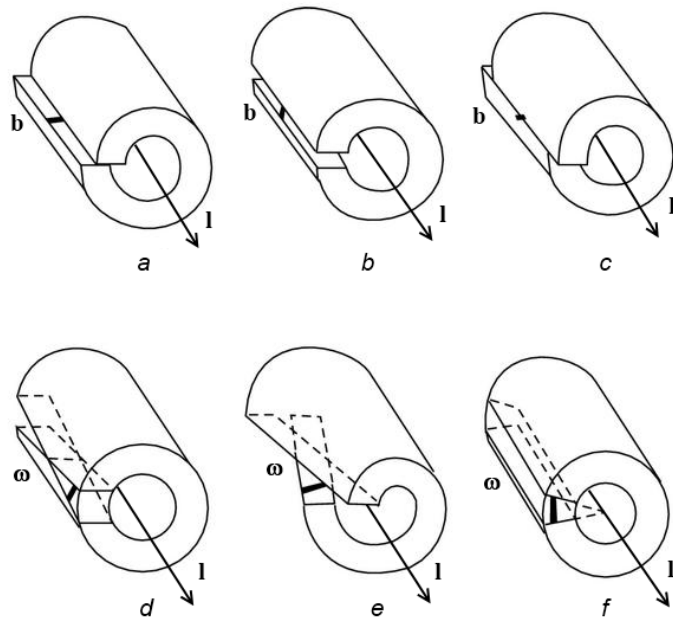


**Figure 2.** Six elementary Volterra's distortions in a hollowed elastic cylinder by the line  $\mathbf{l}$ : edge (a, b) and screw (c) dislocations with Burgers vector  $\mathbf{b}$ , twist (d, e) and wedge (f) disclinations with Frank vector  $\boldsymbol{\omega}$ .

The closing of the angular gap in PNR (Fig. 1b) is equivalent to the introduction of the positive wedge disclination of the strength  $\omega$  along the PNR axis [7, 10]. The resulting configuration of the crystal lattice in the PNR cross-section (which is the plane of the  $\{110\}$ -type) is shown in Fig. 1c where a triangle designates a wedge disclination. The disclination strength  $\omega$  is related to the twinning angle  $\alpha_{twin}$  in FCC lattice (see, for example, [7]):

$$\omega = 2\pi - 5\alpha_{twin} = 2\pi - 10\sin^{-1}\left(\frac{\sqrt{3}}{3}\right) \approx 0.128 \approx 7^{\circ}20'. \quad (1)$$

The presence of the disclination leads to elastic distortions of the crystal lattice in the bulk of PNR (Fig. 1a). In the continuum mechanics model, which is suitable for the calculation of elastic fields and energies, a PNR can be described as an elastic cylinder of radius  $R_p$  with coaxial positive wedge disclination as shown in Fig. 1d. For experimentally observed PNRs  $R_p$  varies from 10 nm to 1  $\mu\text{m}$  [1, 3, 11].

Elastic fields can be analytically found in the framework of linear isotropic model. Non-zero components of stress tensor in cylindrical coordinate system  $(r, \varphi, z)$  associated with axis of PNR are [7]:

$$\begin{aligned} \sigma_{rr} &= \frac{\omega G}{2\pi(1-\nu)} \ln\left(\frac{r}{R_p}\right) \\ \sigma_{\varphi\varphi} &= \frac{\omega G}{2\pi(1-\nu)} \left[ 1 + \ln\left(\frac{r}{R_p}\right) \right] \\ \sigma_{zz} &= \frac{\omega G \nu}{2\pi(1-\nu)} \left[ 1 + 2 \ln\left(\frac{r}{R_p}\right) \right], \end{aligned} \quad (2a,b,c)$$

where  $G$  is a shear modulus,  $\nu$  is Poisson's ratio.

The elastic energy per unit length of PNR is [7]:

$$E_{\omega} = \frac{\omega^2 G R_p^2}{16\pi(1-\nu)}. \quad (3)$$

The energy given by Eq. (3) rapidly increases with the PNR radius. Therefore the development of relaxation processes, which can diminish the stored energy, should be expected. Those relaxation processes include formation of crystal lattice defects such as dislocations, disclinations, pores and other [1–3, 9, 12]. Some of possible mechanism of stress relaxation in PNR is studied in the framework of the present dissertation and considered in chapter 3.

### 1.2.2. Disclination model of icosahedral nanoparticle

A similar approach can be applied to the modeling of INP internal structure (Fig. 1e-i). INP crystal geometry includes FCC monocrystalline regions divided by TBs confined by 20 tetrahedrons. Due to the FCC crystal geometry an angular gap exists (Fig. 1f). The gap is of more complicated shape than in the case of PNR. This gap can be closed by introducing 6 positive wedge disclinations of strength  $\omega$  like shown in Fig. 1g.

Since consideration of a finite size body with 6 disclinations is mathematically difficult, a special kind of a defect can be used instead as an approximation. This defect occupies the whole region of the particle. It is also referred to as Marks-Yoffe disclination [8].

The procedure of constructing Marks-Yoffe disclination can be started with an infinite set of small radial cones with solid angle  $d\omega$  filling uniformly the volume of spheroid. Then those cones are used to remove material from within the cones, and surfaces of them are “glued” to form a solid spheroid again. In the limit  $d\omega \rightarrow 0$  as the eigenstrain is uniformly distributed and described by the following tensor:

$$\begin{aligned}\varepsilon_{\theta\theta}^* &= \varepsilon_{\phi\phi}^* = \chi \\ \varepsilon_{\theta\phi}^* &= \varepsilon_{r\phi}^* = \varepsilon_{r\theta}^* = \varepsilon_{rr}^* = 0 \\ \chi &= \frac{3}{2\pi}\omega \approx 0.0613.\end{aligned}\tag{4a,b,c}$$

in spherical coordinate  $(r, \theta, \phi)$  with the origin in center of the INP.

Note that it would be convenient to use term “inclusion” for Marks-Yoffe disclination. In such approach it is possible to consider an inclusion having the eigenstrain defined as  $\varepsilon_{\theta\theta}^* = \varepsilon_{\phi\phi}^* = -\chi\delta(\Omega)$ , where  $\delta(\Omega)$  is delta-function determined in the volume of inclusion  $\Omega$ .

The elastic strains of the Marks-Yoffe disclination can be written as:

$$\begin{aligned}\varepsilon_{rr} &= \frac{\partial u_r}{\partial r} \\ \varepsilon_{\theta\theta} &= \varepsilon_{\phi\phi} = \frac{u_r}{r} + \chi,\end{aligned}\tag{5a,b}$$

where  $u_r$  is the radial displacement field. The components of the stress tensor corresponding to those strains must satisfy the equations of equilibrium:

$$\frac{\partial \sigma_{rr}}{\partial r} + \frac{2\sigma_{rr} - \sigma_{\theta\theta} - \sigma_{\phi\phi}}{r} = 0.\tag{6}$$

That gives for the total displacements  $u_r$ :

$$u_r = \frac{2\chi}{3} \left( \frac{1-2\nu}{1-\nu} \right) r \ln r + Br + C/r^2, \quad (7)$$

where constants  $B$  and  $C$  are determined from the boundary conditions at free surfaces and absence of displacement in the center. The displacement field in Eq. (7) must be used to calculate strain and stress fields (see Appendix A1 for details) and conform the boundary conditions:

$$\sigma_{rr} \Big|_{r=R_p} = 0. \quad (8)$$

That yields for the coefficients  $B$  and  $C$ :

$$B = -\frac{2\chi}{3} \left( \frac{1-2\nu}{1-\nu} \right) \ln R_p - \frac{2\chi}{3} \quad (9a,b)$$

$$C = 0,$$

where  $R_p$  is radius of the spheroid.

Finally, non-zero components of the elastic strains [8]

$$\varepsilon_{rr} = \frac{2\chi}{3} \left( \frac{1-2\nu}{1-\nu} \right) \left[ \ln \left( \frac{r}{R_p} \right) + 1 \right] - \frac{2\chi}{3} \quad (10a,b)$$

$$\varepsilon_{\theta\theta} = \varepsilon_{\phi\phi} = \frac{2\chi}{3} \left( \frac{1-2\nu}{1-\nu} \right) \ln \left( \frac{r}{R_p} \right) + \frac{\chi}{3}.$$

Stress components are [8]:

$$\sigma_{rr} = \frac{4\chi G(1+\nu)}{3(1-\nu)} \ln \left( \frac{r}{R_p} \right) \quad (11a,b)$$

$$\sigma_{\theta\theta} = \sigma_{\phi\phi} = \frac{2\chi G(1+\nu)}{3(1-\nu)} \left[ 1 + 2 \ln \left( \frac{r}{R_p} \right) \right].$$

The elastic energy of INP is [8]:

$$E_\chi = \frac{8\pi\chi^2 G(1+\nu)R_p^3}{27(1-\nu)}. \quad (12)$$

In Eqs. (11), (12) we use the same notations as in Eqs. (3).

It is easy to see that the stress components of the PNR and INP in Eqs. (2),(11) change sign with the radius, so in the surface region of the PNR and INP a tensile stress takes place and in the core region there is a compressive stress. The distributions of the stress components are shown schematically in Fig. 3.

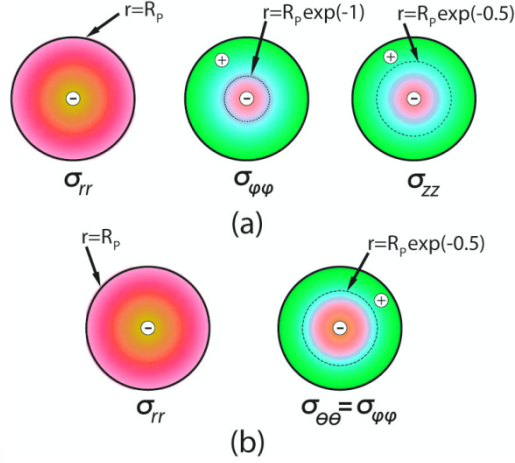


**Figure 3.** Stress distributions in PNRs and INPs schematically. (a) Stress components  $\sigma_{rr}$ ,  $\sigma_{\varphi\varphi}$  and  $\sigma_{zz}$  in PNR in cylindrical coordinate system  $(r, \varphi, z)$  associated with PNR axis; (b) Stress components  $\sigma_{rr}$ ,  $\sigma_{\theta\theta}$  and  $\sigma_{\varphi\varphi}$  in INP in spherical coordinate system  $(r, \theta, \varphi)$  associated with INP center. The radii  $r$  of a sign change of stresses are shown;  $R_p$  is the radius of PNR or INP.

### 1.3. Relaxation of mechanical stresses in pentagonal nanocrystals

The relaxation of elastic stresses due to disclinations is the cause of the transformations of PNR and PNP internal structure that occur as they grow [1, 13]. One of the aims of this dissertation is to demonstrate the possibility of particular relaxation processes in PNRs and PNPs and to provide disclination models describing the observed phenomena.

Over the past two decades stress relaxation models for PNRs and PNPs have been developed and designed. Fig. 4 presents schematics of these models. In the analysis of the models the energy criterion for starting the relaxation process is used:

$$E_{\text{final}} \leq E_{\text{initial}}, \quad (13)$$

where  $E_{\text{initial}}$  and  $E_{\text{final}}$  are the energies of PNP or PNR before relaxation and after relaxation, respectively.

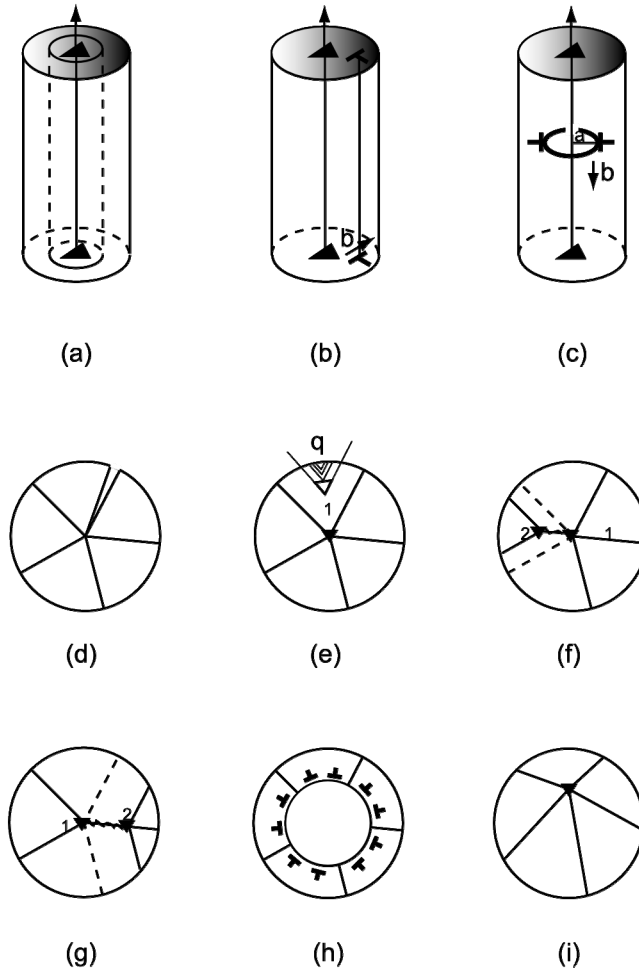


**Figure 4.** The channels of stress relaxation in PNRs and PNPs: (a) appearance of a hollow center; (b) formation of the straight-line dislocation; (c) formation of the vacancy-type dislocation loop; (d) opening of a gap; (e) origination of a negative disclination of power  $\omega_1$  with a system of stacking faults; (f, g) different ways of decomposing the disclination of power  $\omega$  into two others linked by a “disclinal” stacking fault; (h) formation of a region without a disclination; (i) shifting of the pentagonal axis towards the periphery. For simplicity, the channels of relaxation are depicted for the case of PNRs.

It has been shown that the following processes contribute to diminishing elastic energy of PNRs and PNPs: appearance of an empty channel (Fig. 4a) [10, 14]; formation of a straight-line dislocation (Fig. 4b) [1, 15] or vacancy-type

dislocation loop (Fig. 4c) [12]; opening of a crack-like gap (Fig. 4d) [1]; appearance of a negative disclination of power  $\omega_1$  with a system of stacking faults (Fig. 4e) [1]; different ways of decomposing the disclination with power  $\omega$  into two others linked by a “disclinational” stacking fault (Fig. 4f,g) [1]; formation of a region without a disclination (Fig. 4h) [1]; shifting of the pentagonal axis towards the periphery (Fig. 4i) [1]. In addition, molecular dynamics simulation showed that the core of a disclination in a crystal has a “loose” structure, leading to the formation of an empty channel [16].

For several models, critical size of pentagonal particles was evaluated (see, for example [12, 15, 17]). Starting from the critical size the relaxation processes in PNRs and PNPs are triggered by disclinations.

Consistency of the proposed relaxation models with experimental observations was discussed in detail in [1].

Let us now consider some results of experimental studies of nano- and microscale PNRs and PNPs made by electrodeposition of copper in Togliatti State University (method described in [18]). In Fig. 5 pentagonal Cu microrods and microparticles are presented. It also shows the microparticles with a defective external shape: with a hole inside the PR or PP and the nanowhisker growing from the particle. These imperfections are formed during the electrodeposition of the particles with subsequent heating to 400 °C and above in air, which can lead to the formation of cavities, channels and the growth of different whiskers on the surface of the initially seemingly perfect particles.

The following observations should be noted:

- During the electrodeposition nanowhiskers are often formed in the places, where TBs junctions emerge from the surface. These nanowhiskers have mainly pentagonal symmetry, i.e. nanowhiskers are PNRs.
- The holes and empty channels are formed during the PP and PR growth. The growth and formation of the nanowhisker from the particle is accompanied by the formation of internal cavities within the particle.
- After annealing in air or in vacuum, all microparticles tend to lose faceting. Icosahedra annealed in air become overgrown by numerous nanowhiskers, but pentagonal rods do not.

Formation of metallic nanowhiskers on the surface of polycrystals is often referred to as a relaxation of mechanical stresses stored in the material. Various theoretical models of metallic one-dimension nanowhisker growth have been proposed [19–24]. However in only one of those works, namely in [21], were prismatic dislocation loops taken into consideration. One should note that namely prismatic dislocation loops (on the contrary to the case of shear dislocation loops) are related to the condensation of point defects, e.g. in the form of vacancy or interstitial disks. In a new model proposed below in the section 3.3 is combined this idea with the advantages of the disclination approach.

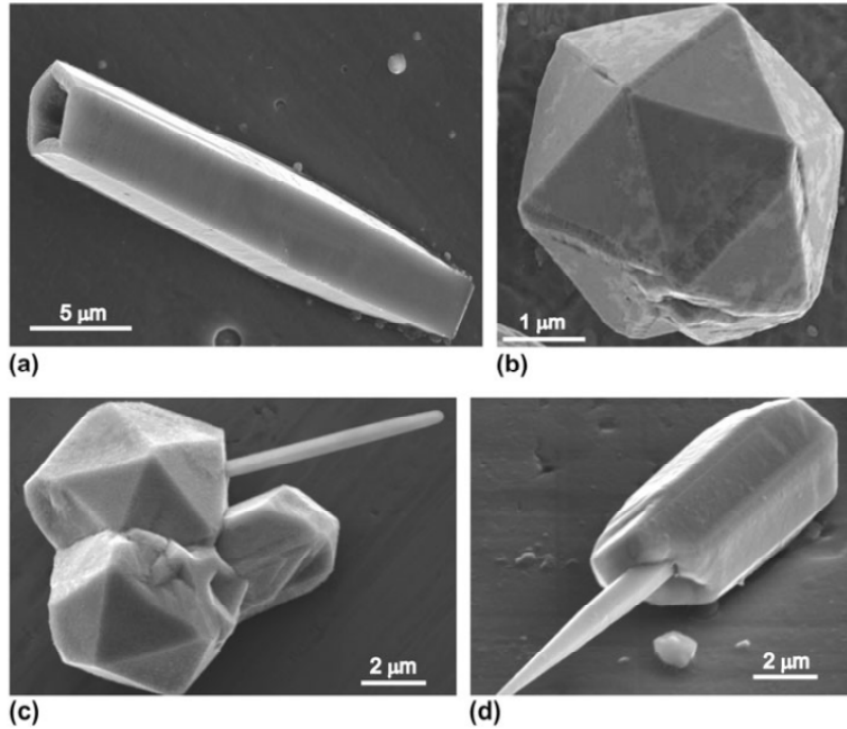


**Figure 5.** Pentagonal microrods and microparticles with cavities (a, b) and whiskers (c, d) obtained by electrodeposition of Cu.

#### **1.4. Friction at the nanoscale and experimental manipulation of nanocrystals**

Friction had been a big challenge for physicists of all times starting from Leonardo Da Vinci and till modern advanced studies. Various theoretical and experimental approaches were employed to get an insight to the friction phenomenon. The theoretical methods ranged from primitive Amontons' laws further to Prandtl-Tomlinson model [25, 26] and computer simulations. Incredibly amount of experimental data on friction had been collected for tribological databases and usage in industry. However the prediction and explanation of friction forces still have not been fully accomplished. The reason for that is natural complexity of the phenomenon involving large amounts of materials and many degrees of freedom. Ordinary statistical mechanical approaches are not sufficient due to essential nonequilibrium of the system and presence of the interface. On the other hand, friction is important in everyday life and crucial in most of engineering problems. Controlling of friction at different scales is becoming more and more significant in the prospects of miniaturization of devices. Particularly, manipulation experiments at the nanoscale are an appealing

technique in order to give an insight on the friction processes at the most fundamental level.

Nanoparticle manipulation experiments have two general purposes: contributing to the understanding of friction mechanisms by providing information about interactions at the nanoscale and practical benefits such as the development of precise positioning and assembly methods for applications in nano-electronics, digital information storage [27], etc.

The most commonly used tool for the manipulation of nanoparticles is the atomic force microscope (AFM, see Fig. 6). The basic principle of AFM is illustrated in Fig. 6 and for more details the reader is referred to [28, 29]. Several different approaches have been applied in AFM manipulation strategies. In dynamic mode, particles can be moved during the scanning process when amplitude of the tip oscillations is increased above a certain threshold value [30], and the frictional force is estimated from the dissipated power [31]. Increasing the scan rate above a certain value rather than increasing oscillation amplitude yields similar results [32]. Another approach consists of switching the feedback off during manipulation [33]. In this case, the tip pushes particles and oscillations are not essential for the manipulation process; cantilever deflection is recorded.

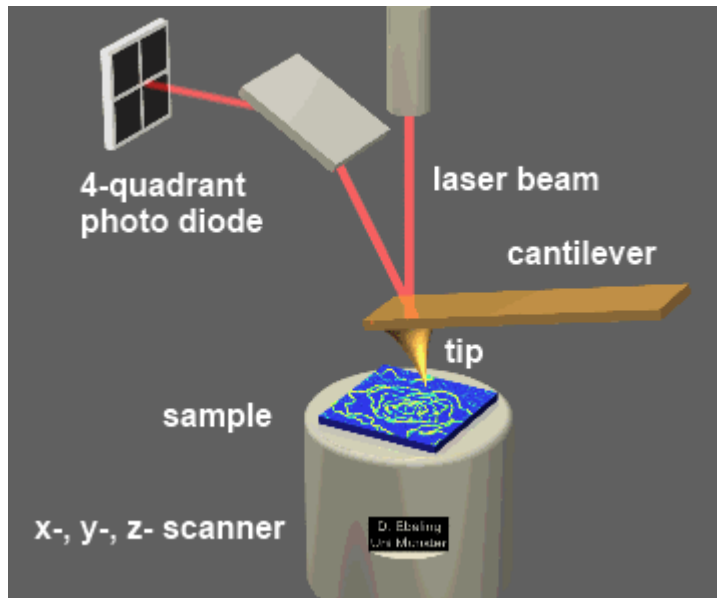


**Figure 6.** Illustration of the basic principle of AFM. Interaction between the sample and the tip affects the motion of the cantilever (in contact or non-contact mode). The deflection of the cantilever is detected by 4-quadrant photo diode capturing the reflected laser beam. The sample is moved relative to the tip via a precise 3D scanning system.

Particles can also be moved in the contact mode. For example, Dietzel *et al.* [34] introduced a so-called “tip-on-top” strategy. In this method, the tip is first positioned on top of the nanoparticle approximately at its center. The nanoparticle then follows the tip motion. The measured torsional signal is directly proportional to the interfacial friction between the particle and the substrate.

AFM manipulations have certain limitations. First, there is no real-time visual feedback concerning the contact geometry or the particle position and behavior during manipulation (i.e., whether it is rolling or sliding). Only indirect conclusions can be drawn based on the shape of the force curves [35]. Additionally, many AFM experiments are made in ambient conditions, meaning that a considerable amount of water is present on all surfaces under investigation, complicating the interpretation of the forces.

Another problem is the “aging” of a sample exposed to ambient conditions, resulting in sticking of the particles to the substrate [36]. Sticking increases significantly with time. Given that AFM manipulation experiments are time consuming, adhesion can increase even within single experimental series.

To overcome these obstacles, manipulation experiments should be performed in a vacuum environment with real-time visual control. Such conditions require more advanced equipment and competence than regular AFM manipulations, however enable to achieve more defined results and ease their interpretation. It is important to note that the above described methods are applicable and widely used also for nanorods and nanowires.

NWs are defined to be 1D crystalline structures with characteristic diameter ranging from 1 to 100 nm. Semiconducting nanowires (NWs) are an important class of nanoscale materials for modern industry. For instance, zinc oxide NWs possess piezoelectric and piezoresistive properties [37, 38], they are a promising material for energy harvesting and micro-/nano- electromechanical systems. Investigation of elastic properties of NWs is therefore crucial for development of innovative devices.

The simplest possible physical system for studies of NW mechanical properties consists of a NW upon a flat surface (substrate) and external manipulator. Physical phenomena in such system may include elasticity of NW (and substrate), adhesion and friction between NW and substrate, static electric forces [39] and conductivity [38]. Despite the simplicity, this system addresses many real-world cases in application scope. However, the state of the art still shows a plenty of “white spots” in the interpretation of the experimental data. Large scattering of experimental data, lack of theoretical explanations, in some cases unpredictable behavior of the system are common for the present. Since the objects are classical, this can be referred to as indefiniteness of the physical system. NWs inherit some degree of “bad” properties of macro- and microscales such as surface defects, possible contaminations and impurities.

Theoretical methods used for investigation of NW’s mechanical and tribological properties range from classical approach continuum models [40], finite element method (FEM) calculations [41] to molecular dynamics simulations [42]. In the studies dedicated to elastic deformation of NWs Timoshenko elastic

beam theory [43, 44] has shown to be fruitful for modeling of elastic strains and interpretation of experimental data [40, 45].

## 1.5. Simulation of nanomanipulations for tribological studies

Control of friction at the nanoscale is of a great importance for science and technology. In some technological applications an usage of conventional lubricants is limited and for this purpose Feynman's concept of nanobearings that "run dry" [46] comes into play. In particular, a simple system where a nanoparticle is clutched between two flat surfaces and the nanoparticle may exhibit rolling motion with low friction seems perspective from applications point of view. One possible system of this kind was proposed by Evstigneev *et al.* in [47], where rolling and sliding of a nanoparticle between two planes was investigated numerically in the framework of a planar model. Let us now briefly consider that model generalized to 3D space since it will be used later on in the paragraph 4.1.

The physical system for a nanoparticle clutched between two planes is depicted in the Fig. 7. The overall geometric configuration is determined by the nanoparticle's center of mass  $\mathbf{r}=xe_x+ye_y+ze_z$ , its rotation that can be represented by an unit quaternion  $q$  (see Appendix A2), and the position  $\mathbf{R}=Xe_x+Ye_y+Ze_z$  of some reference atom from the top plane, where  $\mathbf{e}_{x,y,z}$  are the unit vectors in the  $x$ ,  $y$  and  $z$  directions. The top plane is assumed to be horizontal in each moment of time. If the nanoparticle and the planes are assumed to be rigid bodies, than the state of the entire system is described by  $\mathbf{r}$ ,  $q$ , momentum  $\mathbf{p}$  and angular momentum  $\mathbf{l}$  of the nanoparticle and momentum  $\mathbf{P}$  of the top plane. The momenta yield  $\mathbf{p}=m\dot{\mathbf{r}}$  and  $\mathbf{P}=M\dot{\mathbf{R}}$ , where  $m$  and  $M$  are nanoparticle and top plane masses, respectively. The angular momentum  $\mathbf{l}$  is connected to the angular velocity  $\boldsymbol{\omega}$

$$\mathbf{l} = I\boldsymbol{\omega}, \quad (14)$$

where  $I$  is the tensor of inertia.

The complete system of equations of motion can be written as:

$$\begin{aligned} \dot{\mathbf{p}} &= \mathbf{f}_T + \mathbf{f}_B \\ \dot{\mathbf{l}} &= \boldsymbol{\tau}_T + \boldsymbol{\tau}_B \\ \dot{\mathbf{P}} &= -\mathbf{f}_T + \kappa(X - Vt)\mathbf{e}_x - f_N\mathbf{e}_z. \end{aligned} \quad (15a,b,c)$$

Here  $\mathbf{f}_T$  and  $\mathbf{f}_B$  are external forces acting on a nanoparticle from the top and bottom planes,  $\boldsymbol{\tau}_T$  and  $\boldsymbol{\tau}_B$  are corresponding torques.

The spring is pulled at the constant velocity  $V$ . The last term describes the upper plane under the normal load  $f_N$ . Let us define the instantaneous friction equal to the elastic force of the spring:

$$f = -\kappa(X - Vt). \quad (16)$$

In the present model it is also assumed that the separation between the two planes is sufficiently large, so that the interaction energy between them is negligibly small.

One special case, when there is no top plane can be considered. Then the nanoparticle is driven by a point force  $\mathbf{f}_P$  acting on a point  $\mathbf{r}_P$  and torque  $\boldsymbol{\tau}_P = \mathbf{r}_P \times \mathbf{f}_P$ . Thus the equations of motion are rewritten as

$$\begin{aligned} \dot{\mathbf{p}} &= \mathbf{f}_P + \mathbf{f}_B \\ \dot{\mathbf{l}} &= \boldsymbol{\tau}_P + \boldsymbol{\tau}_B. \end{aligned} \quad (17a,b)$$

Below in the text of this paragraph only the main case with two planes is considered, however all the equations can be easily adapted for the point force case.

Actually the atoms of the nanoparticle and the planes are not rigidly coupled, and they exhibit certain complicated kind of stochastic motion. If the time scale of individual atom's motion is much faster than the time scale of the global degrees of freedom  $\mathbf{r}$ ,  $q$  and  $\mathbf{R}$ , then the effect of atomistic motion can be taken into account by the following modifications of the equations of motion (see [48]): (a) renormalization of the forces and torques acting on the global degrees of freedom; (b) introduction of velocity-dependent dissipation forces corresponding to energy loss in form of heat; (c) introduction of noise force corresponding to energy transfer from atomistic vibrations into the global degrees of freedom.

First modification (a) can be realized by reinterpreting of the interaction energies  $U_{B,T}$  as free energies. This incorporates the system with global degrees of freedom into a statistical ensemble with defined temperature and chemical potential.

Consider the interaction of each atom of the nanoparticle. The interaction potential of the bottom and top planes, respectively

$$\begin{aligned} U_B(\mathbf{r}) &= u_0(z) - u_1(z) \cos\left(\frac{2\pi x}{a}\right) \cos\left(\frac{2\pi y}{a}\right) \\ U_T(\mathbf{r}) &= u_0(Z - z) - u_1(Z - z) \cos\left(\frac{2\pi(x - X)}{a}\right) \cos\left(\frac{2\pi(y - Y)}{a}\right) \end{aligned} \quad (18a,b)$$

These potential are specially constructed to reflect the total potential force of the whole surface acting on a particular single atom in the nanoparticle. To account for the possibility of adhesion, the zero-order term is taken to be the Lennard-Jones potential

$$u_0(z) = \varepsilon \left( \left( \frac{\sigma}{z} \right)^{12} - 2 \left( \frac{\sigma}{z} \right)^6 \right), \quad (19)$$

where  $\varepsilon$  is the adhesion energy and  $\sigma$  the equilibrium separation of the atom from the surface.

The function  $u_1(z)$  in Eq. (18) corresponds to the corrugation amplitude in  $x$  and  $y$  directions. That is assumed to decrease exponentially upon detaching the surface:

$$u_1(z) = \Delta U \exp\left(-\frac{z-\sigma}{\lambda}\right), \quad (20)$$

where  $\Delta U$  is corrugation amplitude and decay length is  $\lambda$ . Other components of the force are dissipative forces (b) due to the internal degrees of freedom. They are proportional to corresponding relative velocities of the nanoparticle's atom to a surface, with coefficients represented by

$$\begin{aligned} \eta_B(r) &= \eta_0 \exp\left(-\frac{z-\sigma}{\xi}\right) \\ \eta_T(r) &= \eta_0 \exp\left(-\frac{(Z-z)-\sigma}{\xi}\right), \end{aligned} \quad (21a,b)$$

where  $\eta_0$  is damping coefficient and  $\xi$  is damping decay length. The external forces  $\mathbf{f}_B$ ,  $\mathbf{f}_T$  or  $\mathbf{f}_P$  and their corresponding torques are the sum over pairwise interaction of each atom of the nanoparticle:

$$\begin{aligned} \mathbf{f}_T &= \sum_i \mathbf{f}_T^{(i)} - \sum_i \eta_T^{(i)} (\dot{\mathbf{r}}_i - \dot{\mathbf{R}}) \\ \mathbf{f}_B &= \sum_i \mathbf{f}_B^{(i)} - \sum_i \eta_B^{(i)} \dot{\mathbf{r}}_i \\ \boldsymbol{\tau}_T &= \sum_i \mathbf{r}'_i \times \mathbf{f}_T^{(i)} - \sum_i \eta_T^{(i)} \mathbf{r}'_i \times (\dot{\mathbf{r}}_i - \dot{\mathbf{R}}) \\ \boldsymbol{\tau}_B &= \sum_i \mathbf{r}'_i \times \mathbf{f}_B^{(i)} - \sum_i \eta_B^{(i)} \mathbf{r}'_i \times \dot{\mathbf{r}}_i. \end{aligned} \quad (22a,b,c,d)$$

Finally, the external forces  $\mathbf{f}_B$  and  $\mathbf{f}_T$  are constructed as a superposition of conservative forces  $\mathbf{f}_B^{(i)}$  and  $\mathbf{f}_T^{(i)}$  described by potentials  $U_B$  and  $U_T$ , and dissipative forces described by  $\eta_B$  and  $\eta_T$ .

In our numerical calculations, we assume that the dissipation effects are much stronger than the inertia effects, allowing us to consider the overdamped limit by formally setting the nanoparticle's mass and moment of inertia to zero:  $m=0$ ,  $I=0$ . Likewise, we assume that the spring attached to the upper plane is overdamped, allowing us to set  $M=0$ . Finally, since the potential energies from Eq. (18) represent an effect of many atoms, noise effects can be assumed extremely small in comparison to the interaction forces and the normal load. Therefore, we neglect thermal noise and in the overdamped zero-temperature limit equation of motions:

$$\begin{aligned}\mathbf{f}_T + \mathbf{f}_B &= 0 \\ \boldsymbol{\tau}_T + \boldsymbol{\tau}_B &= 0.\end{aligned}\tag{23a,b}$$

Keeping in mind Eqs. (22) and  $\dot{\mathbf{r}}_i = \dot{\mathbf{r}} + \boldsymbol{\omega} \times \mathbf{r}'_i$ , we yield

$$\begin{aligned}\sum_i (\eta_T^{(i)} + \eta_B^{(i)}) \dot{\mathbf{r}} + \sum_i (\eta_T^{(i)} + \eta_B^{(i)}) \boldsymbol{\omega} \times \mathbf{r}'_i - \sum_i \eta_T^{(i)} \dot{\mathbf{R}} &= \sum_i (\mathbf{f}_T^{(i)} + \mathbf{f}_B^{(i)}) \\ \left[ \sum_i (\eta_T^{(i)} + \eta_B^{(i)}) \dot{\mathbf{r}}_i' \right] \times \dot{\mathbf{r}} + \left[ \sum_i (\eta_T^{(i)} + \eta_B^{(i)}) \dot{\mathbf{r}}_i' \right] \times (\boldsymbol{\omega} \times \mathbf{r}'_i) - \left[ \sum_i \eta_T^{(i)} \dot{\mathbf{r}}_i' \right] \times \dot{\mathbf{R}} &= \sum_i \mathbf{r}'_i \times (\mathbf{f}_T^{(i)} + \mathbf{f}_B^{(i)}) \\ \sum_i \eta_T^{(i)} (\dot{\mathbf{r}}_i - \dot{\mathbf{R}}) + \kappa \chi \mathbf{e}_x &= \sum_i \mathbf{f}_T^{(i)} + f_N \mathbf{e}_z + \kappa \mathcal{V} t \mathbf{e}_x.\end{aligned}\tag{24a,b,c}$$

These Eqs. (24) are a system of vector equations of motion that can be solved numerically. At any moment of time, they are a linear algebraic system for  $\dot{\mathbf{r}}$ ,  $\boldsymbol{\omega}$  and  $\dot{\mathbf{R}}$  given a nanoparticle's position  $\mathbf{r}$ , rotation  $q$  and top plane's position  $\mathbf{R}$ .

The system of equations of motion for a nanoparticle on a bottom plane and manipulated by a point force:

$$\begin{aligned}\sum_i \eta_B^{(i)} \dot{\mathbf{r}} + \sum_i \eta_B^{(i)} \boldsymbol{\omega} \times \mathbf{r}'_i &= \sum_i \mathbf{f}_B^{(i)} + \mathbf{f}_P \\ \left[ \sum_i \eta_B^{(i)} \dot{\mathbf{r}}_i' \right] \times \dot{\mathbf{r}} + \left[ \sum_i \eta_B^{(i)} \dot{\mathbf{r}}_i' \right] \times (\boldsymbol{\omega} \times \mathbf{r}'_i) &= \sum_i \mathbf{r}'_i \times \mathbf{f}_B^{(i)} + \boldsymbol{\tau}_P.\end{aligned}\tag{25a,b}$$

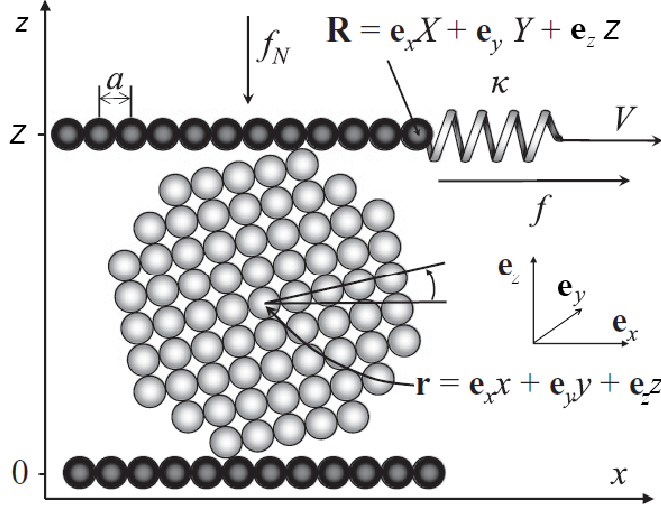


**Figure 7.** Schematics of the physical system: a nanorod is clutched between the fixed lower plan and the upper plane pressed down by the normal load force  $f_N$  and attached to a spring of stiffness  $\kappa$ , the other end of that is pulled with the velocity  $V$ . The friction force  $f$  corresponds to the force of elastic deformation in the spring  $\kappa$ .

## 1.6. Elastic beam theory for modeling of nanowires

Crystalline NWs possess elastic properties and may exhibit flexure. The elasticity of NWs can be considered in the framework of the continuum theory of elasticity. However the exact analytic solution of the elasticity problem in most practical cases is hardly achievable due to complicated boundary conditions. The necessity to account for elastic effects in prolonged objects has also arisen in engineering problems such as building construction. That gave a strong incentive to development of a theory for approximate solutions of elasticity problems, i.e. the elastic beam theory (EBT) [43, 44]. The recall of certain models from the EBT helps to model the elastic behavior of NWs. In the present paragraph we will go through the basic statements of the EBT that will be used further in the study.

Let us consider a prismatic-shaped NW of length  $L$  and diameter  $D$ , bent under external lateral forces (see Fig. 8). The external forces may include distributed (such as friction) forces as well as concentrated forces (such as driving force from the tip). The state of NW is sustained in equilibrium due to interplay of intrinsic elastic force in the NW and the external forces of various origins.

We will designate the force and momentum of elastic stresses in a cross section of the NW as  $\mathbf{F}$  and  $\mathbf{M}$ , respectively. Their components can be written as an integral by the cross section area  $S$  at any given point  $l$  of NW axis [43, 44]:

$$F_i = \int_S \sigma_{i\gamma} n_\gamma dS \quad (26a, b)$$

$$M_i = \int_S e_{i\alpha\beta} r_\alpha \sigma_{\beta\gamma} n_\gamma dS,$$

where  $\sigma_{\alpha\beta}$  are the components of stress tensor,  $n_\gamma$  are the components of the normal vector to the element of cross section area  $dS$ ,  $r_\alpha$  are the components of the radius vector from the axial point  $l$  and  $e_{\alpha\beta\gamma}$  represents the unit anti-symmetric tensor. Both the elastic force  $\mathbf{F}$  and the momentum  $\mathbf{M}$  are considered as functions of the coordinate  $l$  along the NW's axis (Fig. 8).

The full system of equilibrium equations for the NW consists of the equations for elastic force  $\mathbf{F}$  and momentum  $\mathbf{M}$  [44]:

$$\begin{aligned} \frac{d\mathbf{F}}{dl} &= -\mathbf{f} \\ \frac{d\mathbf{M}}{dl} &= \mathbf{F} \times \mathbf{t}, \end{aligned} \quad (27a,b)$$

where  $\mathbf{f}$  is the distributed external force acting on the NW per unit length and  $\mathbf{t}$  is the tangent vector of the NW axis.

Here and below we limit the consideration to a particular assumption that the NW is undergoing a pure bending deformation. This can be a good approximation for the given problem as long as one assumes that the external forces act to the direction normal of the NW. The case of pure bending of prismatic shaped NW yields the following equation for momentum in the framework of linear isotropic elasticity [44]:

$$\mathbf{M} = EI\mathbf{t} \times \frac{d\mathbf{t}}{dl}, \quad (28)$$

where  $E$  is the Young modulus of the NW and  $I$  is the area moment of inertia of the NW. Eq. (10) describes the momentum of elastic forces inside a NW bent purely with the given curvature. It can be projected to the  $Oz$  axis and rewritten as

$$M = EI \frac{d\varphi}{dl} = EI\kappa, \quad (29)$$

where  $\varphi(l)$  is the tangent angle function over the length of the NW and  $\kappa(l) = 1/R(l) = d\varphi/dl$  is the curvature function related to the local radius of curvature  $R(l)$ .

The equations of equilibrium Eqs. (27) and “pure bending” Eq. (28) comprise the full system of equations that determine the state of the NW. Boundary conditions on  $\mathbf{F}$  and/or  $\mathbf{M}$  have to be defined in order to solve this system. The choice of boundary conditions is dictated by the problem statement and may include, e.g. the condition of free end or “walled” end (see the examples in [44]).

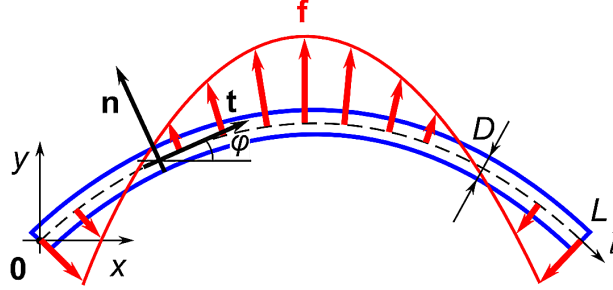


**Figure 8.** Schematics of a nanowire of length  $L$  and diameter  $D$  held in bent state by in-plane distributed lateral force  $\mathbf{f}$ . Fixed coordinates system  $Oxyz$  and local coordinate basis  $(\mathbf{t}, \mathbf{n})$  along the nanowire axis  $l$  are used. Angle between the tangent vector  $\mathbf{t}$  and axis  $Ox$  is denoted as  $\varphi$ .

## I.7. Coupling of elastic and tribological properties of nanowires on flat substrate

Elastically deformed NWs are appealing objects for investigation due to possibility of measurements of NW’s elastic properties and coupling with other phenomena such as piezoresistivity [38, 49], piezoelectricity [50] and friction. For the latter case NW is maintained in deformed state by external force of friction between the NW, substrate and optionally external concentrated force originating from AFM tip.

A simple approach, which utilizes the bent shape of a nanowire on a substrate to estimate the nanowire-substrate friction, was proposed by Bordag *et al.* [45]. The profile of bent NW comes as a result of the interplay between elastic and friction forces. The modeled NW was assumed to form a circle with uniform distribution of elastic and friction forces along the NW. This method was applied for the study of static and kinetic friction, and for determination of local strain in individual semiconductor NWs [39, 51, 52]. However, the model neglected the role of free NW ends and did not take into account the fact that the actual friction force vector may vary significantly along the NW’s length.

Strus *et al.* introduced a more sophisticated method, which also utilizes the shape of a carbon nanotube (CNT) bent by AFM on substrate to compute static friction and flexural strain energy [40]. Unfortunately, this method is highly sensitive to any inaccuracy in determination of the bent CNT or NW profile due to use of high order derivatives. Furthermore, unconsidered boundary condi-

tions of zero force and momentum at the ends of the CNT may contribute significant error to the results.

Therefore an alternative model of elastically bent NW lying on a flat substrate has to be proposed, which enables determination of friction forces between NW and substrate. Appropriate skeletonization and fitting algorithm must be elaborated that conforms to the boundary conditions.

Let us consider some of important peculiarities related to flexure-friction coupling. As it was described in the previous paragraph, elastic properties of purely bent NW are determined by its Young modulus  $E$  and area moment of inertia  $I$  which is directly related to geometry of the NW (cross section), particularly the diameter  $D$ . In one's turn cross section of NW defines the NW-substrate contact area and the area in the vicinity of the contact that essentially influence the NW-substrate friction.

Several geometries of cross section characteristic for NWs are presented in Fig. 9. Contact regions for first two – hexagonal and rectangular (belt) shapes are easily defined. Determination of contact region for circular cross section is a non-trivial problem that requires employment of contact mechanics models such as Johnson-Kendall-Roberts (JKR) or Derjaguin-Muller-Toporov (DMT) [53, 54]. The hexagonal cross section is intermediate between the rectangular, where contact line is equal to the whole diameter and the circular case, where the contact line is a small fraction of the diameter. In the present work the hexagonal cross section was chosen for the calculations in the experimental part for ZnO NWs.

The maximal tensile stress  $\sigma_{\max}$  that apparently occurs on the outermost side of NW, can be expressed as a function of local NW curvature  $\kappa$ :

$$\sigma_{\max} = ED\kappa/2. \quad (30)$$

Equation (30) can be used furthermore in order to estimate the tensile strength of the NW when the manipulation ended up with a fracture.

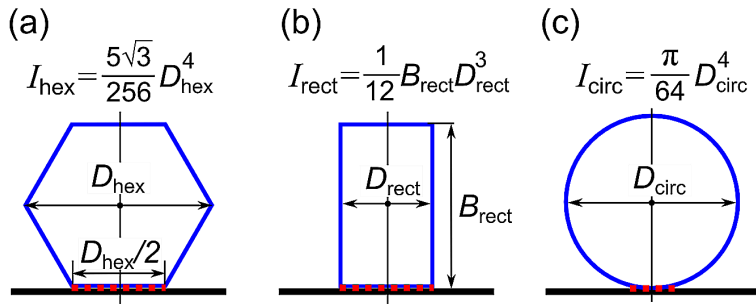


**Figure 9.** Schematics of cross sections of NWs, corresponding contact region with substrate and area moment of inertia. Hexagonal cross section of diameter  $D_{\text{hex}}$  (a). Rectangular cross section of width  $D_{\text{rect}}$  and height  $B_{\text{rect}}$  (b). Circular cross section of diameter  $D_{\text{circ}}$  (c).

## 2. AIM OF THE STUDY

The main goal of the study is contribution to understanding of the properties and phenomena specific for nanoscale objects such as nanoparticles and nanowires. A number of objectives were identified in order to achieve this goal. Both theoretical and experimental methods were utilized to realize the objectives.

The primary list of the objectives included:

- Elaboration of a theoretical model of stress relaxation in pentagonal multiply-twinned nanoparticles and nanorods related to formation of shell layer with crystal lattice mismatch in the framework of the disclination approach;
- Development of a theoretical model for explanation of formation of micro- and nano- whiskers in presence of mechanical stresses that can be originated from specific structure of pentagonal nanocrystals;
- Proposing a theoretical model and conducting numerical experiments on simulation of manipulation of pentagonal (icosahedral) nanoparticles by means of specific driving forces;
- Implementation of an experimental setup for real-time *in situ* manipulation of nanoparticles and nanowires inside a scanning electron microscope (SEM);
- Analysis of tribological properties of nanoparticles via conducting of nanomanipulation experiments of gold nanoparticles on flat substrates such as oxidized Si wafer;
- Analysis of tribological and elastic properties of nanowires via conducting of nanomanipulation experiments of zinc oxide nanowires on a flat substrate like in the former case of nanoparticles;

### 3. STRUCTURAL PROPERTIES OF PENTAGONAL 0D AND 1D NANOCRYSTALS

#### 3.1. Pentagonal nanorods with crystal lattice mismatch layer

As we have already revealed in paragraphs 1.2 and 1.3, PNCs possess internal mechanical stresses in them. Those stresses have to be released via relaxation mechanisms. By taking a closer look at the Fig. 3, one may notice that the PNCs share a common properties of having tensile stresses in the outer region and compressing stress in the inner region. Now let us propose a new mechanism of stress relaxation: the tensile stress in the surface region of PNR and INP can be diminished by increasing the crystal lattice constant in this region. This means the formation of so-called mismatched (misfit) layer. One can expect that stresses and elastic energy of PNR and PNP can be diminished during formation of mismatched shell layer.

Let us consider a model for non-uniform PNR consisting of two phases, i.e. core and shell, with different crystal lattice parameters and elastic modules as it shown in the Fig. 10. In this figure shear modules and Poisson's ratios are designed as  $G_1, \nu_1$  for core and  $G_2, \nu_2$  for shell respectively. The lattice misfit parameter  $\varepsilon^*$  is defined as

$$\varepsilon^* = \frac{a_{\text{core}} - a_{\text{shell}}}{a_{\text{core}}}, \quad (31)$$

where  $a_{\text{core}}$  and  $a_{\text{shell}}$  are the lattice parameters of the core and shell.

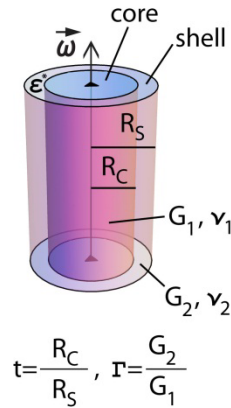


**Figure 10.** Formation of mismatched shell layer in PNRs.

As a result a shelled PNR is described as a two-phase infinite cylinder, including co-axial positive wedge disclination of strength  $\omega$  and co-axial cylindrical inclusion with eigenstrain  $\varepsilon^*$ . In this way the elastic field in shelled PNR, for example stresses  $\sigma_{ij}$ , can be calculated as a superposition of the disclination field  $\sigma_{ij}(\omega)$  and the field  $\sigma_{ij}(\varepsilon^*)$  due to inclusion. On the other hand stresses  $\sigma_{ij}(\varepsilon^*)$  can be considered as caused by mismatched layer. Note that shelled PNR is a typical core/shell cylindrical structure complicated by disclination. For these reasons we use terms “inclusion”, “core”, “layer”, and “shell” in the following.

Elasticity boundary-value problem for non-uniform PNR assumes standard Hook’s law relations for both phases, equations of equilibrium for the bulk of the core and the shell, and following boundary conditions:

$$\begin{aligned} \sigma_{rj}^{(2)} \Big|_{r=R_s} &= 0 \\ \sigma_{rj}^{(1)} \Big|_{r=R_c} &= \sigma_{rj}^{(2)} \Big|_{r=R_c} \\ u_j^{(1)} \Big|_{r=R_c} &= u_j^{(2)} \Big|_{r=R_c}, \quad j = r, \varphi, z, \end{aligned} \quad (32a,b,c)$$

where  $u_i$  are displacements in cylindrical coordinate system  $(r, \varphi, z)$  associated with axis of PNR, upper indexes (1) and (2) mean core and shell correspondingly,  $R_c$  is a core radius of PNR and  $R_s$  is shell radius of PNR. In the cross-section of PNR the condition of zero axial load must be fulfilled:

$$\iint_S \sigma_{zj} ds = 0. \quad (33)$$

The Eq. (33) reflects that no external stress is applied to the butt-ends of the PNR when modeling it as an infinite cylinder. Here  $S$  is the area of cylinder cross-section.

The solutions of boundary-value problem for  $\sigma_{ij}(\omega)$  and  $\sigma_{ij}(\varepsilon^*)$  are given separately in the paragraphs 3.1.1 and 3.1.2. In the framework of the linear theory of elasticity it is possible to find the total elastic energy of PNR with mismatched layer  $E_{CP(\omega)}$  as the sum of three terms:

$$E_{CP(\omega)} = E_\omega + E_{\varepsilon^*} + E_{\omega-\varepsilon^*}, \quad (34)$$

where  $E_\omega$  is the energy of disclination in two-phase cylinder,  $E_{\varepsilon^*}$  is the energy of two-phase cylinder with mismatched layer, or cylindrical inclusion in cylinder, and  $E_{\omega-\varepsilon^*}$  is the energy of interaction between the disclination and cylindrical inclusion.

### 3.1.1. Solution for disclination in two-phase cylinder. Stresses and energy

Let us take the displacement field for a wedge disclination  $\omega$  in a two-phase cylinder in the both regions in the following form:

$$u_{r(\omega)}^{(1)} = \frac{r\omega(1-\nu_1 + (2\nu_1 - 1)\ln(r/R_S))}{4\pi(\nu_1 - 1)} + B_1 r$$

$$u_{r(\omega)}^{(2)} = \frac{r\omega(1-\nu_2 + (2\nu_2 - 1)\ln(r/R_S))}{4\pi(\nu_2 - 1)} + B_2 r + C_2 / r \quad (35a,b,c,d)$$

$$u_{\varphi(\omega)}^{(1)} = u_{\varphi(\omega)}^{(2)} = r\varphi \frac{\omega}{2\pi}$$

$$u_{z(\omega)}^{(1)} = u_{z(\omega)}^{(2)} = Dz$$

for the total displacement in the core and the shell, respectively.  $B_1$ ,  $B_2$ ,  $C_2$  and  $D$  are unknown constants determined by boundary conditions for the displacements and stresses:

$$u_{r(\omega)}^{(1)} \Big|_{r=R_C} = u_{r(\omega)}^{(2)} \Big|_{r=R_C}$$

$$\sigma_{rr(\omega)}^{(1)} \Big|_{r=R_C} = \sigma_{rr(\omega)}^{(2)} \Big|_{r=R_C}$$

$$\sigma_{rr(\omega)}^{(2)} \Big|_{r=R_S} = 0 \quad (36a,b,c,d)$$

$$\iint_S \sigma_{zz(\omega)} dS = 2\pi \left( \int_0^{R_C} \sigma_{zz(\omega)}^{(1)} r dr + \int_{R_C}^{R_S} \sigma_{zz(\omega)}^{(2)} r dr \right) = 0.$$

The system of Eqs. (36) solved for  $B_1$ ,  $B_2$ ,  $C_2$  and  $D$  is described in Appendix A3. Finally, the mechanical stresses of the positive wedge disclination  $\sigma_{ij(\omega)}$  in the two-phase cylinder in a closed analytical form:

$$\begin{aligned}
\sigma_{rr(\omega)}^{(1)} &= -\frac{\omega G_1}{2\pi(1-\nu_1)A} \cdot \\
&\left\{ G_1^2(1+\nu_1)t^2 \left[ (\ln(t) - \ln(R_s^{-1}r))(2\nu_2 t^2 - t^2 - 1) \right] + \right. \\
&+ G_1 G_2 \left[ -2\nu_1^2 t^2 \ln(t) + t^2 \ln(t) + t^2 \ln(R_s^{-1}r) - \right. \\
&- \nu_1(1+4\nu_2)t^2(t^2-1)(\ln(t) - \ln(R_s^{-1}r)) + (2t^4-1)(\ln(t) - \ln(R_s^{-1}r)) - \\
&- \left. \left. \nu_2(t^2-1)^2(\ln(t) - \ln(R_s^{-1}r)) \right] + \right. \\
&+ G_2^2(1+\nu_2)(t^2-1) \left[ -t^2 \ln(t) + t^2 \ln(R_s^{-1}r) - \ln(t) - \ln(R_s^{-1}r) + \right. \\
&+ \left. \left. 2\nu_1(t^2 \ln(t) - (t^2-1)\ln(R_s^{-1}r)) \right] \right\}, \tag{37a}
\end{aligned}$$

$$\begin{aligned}
\sigma_{rr(\omega)}^{(2)} &= -\frac{\omega G_2}{2\pi(1-\nu_2)A} \cdot \\
&\left\{ G_1^2(1+\nu_1)t^2 \left[ -t^2 \ln(t) + 2\nu_2 t^2 (\ln(t) - \ln(R_s^{-1}r)) + \right. \right. \\
&+ \left. \left. (t^2+1)\ln(R_s^{-1}r) + (1-2\nu_2)t^2 \ln(t) R_s^2 r^{-2} \right] + \right. \\
&+ G_1 G_2 \left[ t^2(2t^2-1)\ln(t) - \nu_1(1+4\nu_2)t^2(t^2 \ln(t) - (t^2-1)\ln(R_s^{-1}r)) + \right. \\
&+ \left. \left. (-2t^4+t^2+1)(\ln(R_s^{-1}r)+1) + \right. \right. \\
&+ \left. \left. 2\nu_2^2 t^2 \ln(t) + \nu_2 t^2(t^2-1)\ln(t) + \nu_2(t^2-1)^2 \ln(R_s^{-1}r) + \right. \right. \\
&+ \left. \left. t^2 \ln(t) (\nu_1 t^2(4\nu_2+1) - 2t^2 + \nu_2(t^2-2\nu_2-1)+1) R_s^2 r^{-2} \right] + \right. \\
&+ \left. \left. G_2^2(1+\nu_2)(2\nu_1-1)(t^2-1) \left[ t^2 \ln(t) - (t^2-1)\ln(R_s^{-1}r) - t^2 \ln(t) R_s^2 r^{-2} \right] \right\}, \tag{37b}
\end{aligned}$$

$$\begin{aligned}
\sigma_{\varphi\varphi(\omega)}^{(1)} &= -\frac{\omega G_1}{2\pi(1-\nu_1)A} \cdot \\
&\left\{ G_1^2(1+\nu_1)t^2 \left[ (\ln(t) - \ln(R_s^{-1}r) - 1)(2\nu_2 t^2 - t^2 - 1) \right] + \right. \\
&+ G_1 G_2 \left[ -2t^4 - 2\nu_1^2 t^2 \ln(t) + t^2 \left( (2t^2+1)\ln(t) + (1-2t^2)\ln(R_s^{-1}r) \right) - \right. \\
&- \nu_1(1+4\nu_2)(t^2-1)(\ln(t) - \ln(R_s^{-1}r) - 1) + t^2 - \ln(t) + \ln(R_s^{-1}r) + 1 - \\
&- \left. \left. \nu_2(t^2-1)^2(\ln(t) - \ln(R_s^{-1}r) - 1) \right] + \right. \\
&+ G_2^2(1+\nu_2)(t^2-1) \left[ -t^2 \ln(t) + t^2 \ln(R_s^{-1}r) + t^2 - \ln(t) - \ln(R_s^{-1}r) + \right. \\
&+ \left. \left. 2\nu_1(t^2 \ln(t) - (t^2-1)(\ln(R_s^{-1}r)+1)) - 1 \right] \right\}, \tag{37c}
\end{aligned}$$

$$\sigma_{\varphi\varphi(\omega)}^{(2)} = -\frac{\omega G_2}{2\pi(1-\nu_2)A} \cdot$$

$$\left\{ G_1^2(1+\nu_1)t^2 \left[ -t^2 \ln(t) + 2\nu_2 t^2 (\ln(t) - \ln(R_s^{-1}r) - 1) + \right. \right.$$

$$\left. + (t^2 + 1)(\ln(R_s^{-1}r) + 1) + (2\nu_2 - 1)t^2 \ln(t) R_s^2 r^{-2} \right] +$$

$$+ G_1 G_2 \left[ t^2 (2t^2 - 1) \ln(t) - \nu_1 (1 + 4\nu_2) t^2 (t^2 \ln(t) - (t^2 - 1)(\ln(R_s^{-1}r) + 1)) - \right.$$

$$\left. - (t^2 - 1)(2t^2 + 1)(\ln(R_s^{-1}r) + 1) + \right.$$

$$+ 2\nu_2^2 t^2 \ln(t) + (t^2 - 1)((t^2 - 1)(\ln(R_s^{-1}r) + 1) - t^2 \ln(t)) -$$

$$\left. - t^2 \ln(t) (\nu_1 t^2 (4\nu_2 + 1) - 2t^2 + \nu_2 (t^2 - 2\nu_2 - 1) + 1) R_s^2 r^{-2} \right] +$$

$$+ G_2^2 (1 + \nu_2) (2\nu_1 - 1) (t^2 - 1) \left[ t^2 \ln(t) - (t^2 - 1)(\ln(R_s^{-1}r) + 1) + t^2 \ln(t) R_s^2 r^{-2} \right] \},$$

$$\sigma_{zz(\omega)}^{(1)} = -\frac{\omega G_1}{2\pi(1-\nu_1)A} \cdot$$

$$\left\{ G_1^2(1+\nu_1)\nu_1 t^2 \left[ (2\ln(t) - 2\ln(R_s^{-1}r) - 1)(2\nu_2 t^2 - t^2 - 1) \right] + \right.$$

$$+ G_1 G_2 \left[ 4\nu_2 t^2 \ln(t) + \nu_1^2 t^2 (4\nu_2 (-2t^2 \ln(t) + t^2 + \ln(t) + 2(t^2 - 1)\ln(R_s^{-1}r) - 1) - \right.$$

$$\left. - (t^2 - 1)(2\ln(t) - 2\ln(R_s^{-1}r) - 1) \right] +$$

$$+ \nu_1 (2\ln(t) - 2\ln(R_s^{-1}r) - 1) (2t^4 - t^2 - \nu_2 (t^2 - 1)^2 - 1) \left. \right] +$$

$$+ G_2^2 (1 + \nu_2) \nu_2 (2\nu_1 - 1) (t^2 - 1) \left[ 2t^2 \ln(t) - (t^2 - 1)(2\ln(R_s^{-1}r) + 1) \right] \},$$

$$\sigma_{zz(\omega)}^{(2)} = -\frac{\omega G_2}{2\pi(1-\nu_2)A} \cdot$$

$$\left\{ G_1^2(1+\nu_1)\nu_2 t^2 \left[ -2t^2 \ln(t) + 2\nu_2 t^2 (2\ln(t) - 2\ln(R_s^{-1}r) - 1) + (t^2 + 1)(2\ln(R_s^{-1}r) + 1) \right] + \right.$$

$$+ G_1 G_2 \left[ \nu_1 t^2 (-2\nu_2 t^2 \ln(t) + \nu_2 (t^2 - 1)(2\ln(R_s^{-1}r) + 1) + \right.$$

$$+ 4\nu_2^2 ((1 - 2t^2) \ln(t) + \ln(t)(t^2 - 1)(2\ln(R_s^{-1}r) + 1)) - 4\ln(t) \left. \right]$$

$$+ \nu_2 (2t^2 - \nu_2 (t^2 - 1) + 1) (2t^2 \ln(t) - (t^2 - 1)(2\ln(R_s^{-1}r) + 1)) \left. \right] +$$

$$+ G_2^2 (1 + \nu_2) \nu_2 (2\nu_1 - 1) (t^2 - 1) \left[ 2t^2 \ln(t) - (t^2 - 1)(2\ln(R_s^{-1}r) + 1) \right] \},$$

$$A = G_1^2(1+\nu_1)t^2(2\nu_2 t^2 - t^2 - 1) + G_1 G_2 (t^2 - 1) ((2 - \nu_2)t^2 + \nu_2 + 1 - \nu_1 t^2 (1 + 4\nu_2)) +$$

$$+ G_2^2 (1 + \nu_2) (2\nu_1 - 1) (t^2 - 1)^2. \quad (37g)$$

Here upper indexes (1) and (2) designate core and shell correspondingly;  
 $t=R_C/R_S$ .

The elastic energy of disclination in two-phase cylinder per unit length is:

$$\begin{aligned}
E_\omega &= \frac{\omega^2 R_s^2}{16\pi(1-\nu_1)(1-\nu_2)A} \cdot \\
&\left\{ G_1^3(1+\nu_1)(1-\nu_2)t^4(2\nu_2t^2-t^2-1) - \right. \\
&- G_2^2 G_2 t^2 \left[ -3t^4 + 4t^2 \ln^2(t) - (1+\nu_1)\nu_2 t^2 (-5t^2 + 8\ln^2(t) + 2\nu_1(t^2 - 4\ln^2(t) - 1) + 5) + \right. \\
&+ t^2 - \nu_2^2(t^2 - 1)(4\nu_1 t^2 + t^2 - 1) + \nu_1(t^4 - t^2 + \nu_1(t^4 - 4t^2 \ln^2(t) - 1)) + 2 \left. \right] + \\
&+ G_2^3(1-\nu_1)(1+\nu_2)(1-2\nu_1)(t^2 - 1)((t^2 - 1)^2 - 4t^2 \ln^2(t)) - \\
&- G_2^2 G_1 \left[ 3t^6 - 5t^4 + 4t^2(1-2t^2)\ln^2(t) - \nu_1^2(1+4\nu_2)t^2((t^2 - 1)^2 - 4t^2 \ln^2(t)) + \right. \\
&+ t^2 + \nu_1(1+\nu_2)(4t^2(3t^2 - 1)\ln^2(t) + 2\nu_2 t^2((t^2 - 1)^2 + 4\ln^2(t)) - (t^2 - 1)^2(5t^2 + 1)) + \\
&\left. + \nu_2(-(t^2 - 1)^3 + 4t^2(t^2 - 1)\ln^2(t) - \nu_2 t^2((t^2 - 1)^2 + 8\ln^2(t))) + 1 \right] \left. \right\} \quad (38)
\end{aligned}$$

### 3.1.2. Solution for cylinder with mismatched phases. Stresses and energy

Formation of mismatched shell layer in PNR leads to eigenstrain in the shell region  $\varepsilon^*$ . Thus, plastic displacements in the cylinder representing the PNR can be written as:

$$\begin{aligned}
\hat{u}_r^{(1)} &= \hat{u}_\phi^{(1)} = \hat{u}_z^{(1)} = 0 \\
\hat{u}_r^{(2)} &= -\varepsilon^* r, \quad \hat{u}_\phi^{(2)} = 0, \quad \hat{u}_z^{(2)} = -\varepsilon^* z.
\end{aligned} \quad (39a,b)$$

Elastic displacements are:

$$\begin{aligned}
u_r^{(1)} &= B_1 r, \quad u_\phi^{(1)} = 0, \quad u_z^{(1)} = D_1 z \\
u_r^{(2)} &= B_2 r + C_2 / r, \quad u_\phi^{(2)} = 0, \quad u_z^{(2)} = D_2 z.
\end{aligned} \quad (40a,b)$$

Here  $B_1$ ,  $D_1$ ,  $B_2$ ,  $C_2$  and  $D_2$  are unknown constants. Boundary conditions for the total displacements will be same as in Eqs. (36). The solution for them and strain tensor components are described in Appendix A4. The stresses of two-phase cylinder with mismatched shell layer have been found as following:

$$\sigma_{rr(\varepsilon^*)}^{(1)} = -\frac{2\varepsilon^* G_1 G_2 (1+\nu_1)(1+\nu_2) \left( (G_1 - G_2)t^2 + G_2 \right) (t^2 - 1)}{A}, \quad (41a)$$

$$\sigma_{rr(\varepsilon^*)}^{(2)} = -\frac{2\varepsilon^* G_1 G_2 (1+\nu_1)(1+\nu_2) \left( (G_1 - G_2)t^2 + G_2 \right) t^2 (1 - R_s^2 r^{-2})}{A}, \quad (41b)$$

$$\sigma_{\phi\phi(\varepsilon^*)}^{(1)} = -\frac{2\varepsilon^* G_1 G_2 (1+\nu_1)(1+\nu_2) \left( (G_1 - G_2)t^2 + G_2 \right) (t^2 - 1)}{A}, \quad (41c)$$

$$\sigma_{\phi\phi(\varepsilon^*)}^{(2)} = -\frac{2\varepsilon^* G_1 G_2 (1+\nu_1)(1+\nu_2) \left( (G_1 - G_2)t^2 + G_2 \right) t^2 (1+R_s^2 r^{-2})}{A}, \quad (41d)$$

$$\sigma_{zz(\varepsilon^*)}^{(1)} = -\frac{2\varepsilon^* G_1 G_2 (1+\nu_1)(1+\nu_2) \left( (t^2 + 1)G_1 - (t^2 - 1)G_2 \right) (t^2 - 1)}{A}, \quad (41e)$$

$$\sigma_{zz(\varepsilon^*)}^{(2)} = -\frac{2\varepsilon^* G_1 G_2 (1+\nu_1)(1+\nu_2) \left( (t^2 + 1)G_1 - (t^2 - 1)G_2 \right) t^2}{A}. \quad (41f)$$

Here all designations are as those used in Eqs. (37).

The elastic energy  $E_{\varepsilon^*}$  of a two-phase cylinder with mismatched layer per unit length is:

$$E_{\varepsilon^*} = \frac{\pi\varepsilon^{*2} G_1 G_2 (1+\nu_1)(1+\nu_2) \left( (3t^2 + 1)G_1 - 3(t^2 - 1)G_2 \right) t^2 (t^2 - 1) R_s^2}{A}. \quad (42)$$

On the base of elastic fields Eqs. (37) or Eqs. (41) one can calculate the energy of interaction between the disclination and cylindrical inclusion:

$$E_{\omega-\varepsilon^*} = \frac{2\omega\varepsilon^* G_1 G_2 (1+\nu_1)(1+\nu_2) \left( (G_1 - G_2)t^2 + G_2 \right) t^2 \ln(t) R_s^2}{A}. \quad (43)$$

### 3.1.3. Conditions for mismatched crystal lattice layer formation in PNR

Energy release in the result of formation of the mismatched layer in PNR is defined as:

$$\Delta E_{CP(\omega)} = (E_{\omega} + E_{\varepsilon^*} + E_{\omega-\varepsilon^*}) - E_{\omega}^0, \quad (44)$$

where  $E_{\omega}^0$  is the energy of unshelled PNR with radius  $R_s$ .

Diagrams for energy release per unit length for PNR are shown in Fig. 11. One can see areas where  $\Delta E_{CP(\omega)} < 0$ . It means that formation of such layer is energetically favorable. Fig. 11a and 11b demonstrates the energy release  $\Delta E_{CP(\omega)}$  as a function of the core/shell radii ratio  $t$  at different misfit parameters  $\varepsilon^*$  and ratio of shear moduli  $\Gamma$ . The contours of the energy release  $\Delta E_{CP(\omega)}$  as a function of  $t$  and mismatch parameter  $\varepsilon^*$  are shown in Fig. 11c.

Optimal misfit parameter  $\varepsilon_{opt}^*$  and radii ratio  $t_{opt}$  are defined as the parameters which give the global maximum of elastic energy release. For shelled PNR at equal elastic modules of core and shell the optimal parameters are obtained numerically:  $\varepsilon_{opt}^* \approx -0.01$ ;  $t_{opt} \approx 0.45$ .

The case of elastically softer shell, i.e. for elastic modulus ratio  $\Gamma=G_2/G_1<1$  (see the top of Fig. 11b), is of special interest. Under such conditions the gain in energy exists for  $\varepsilon^* >0$ , i.e. for the lattice parameter of the shell being smaller than that of the core. On the contrary, for  $\Gamma>1$  (see the bottom of Fig. 11b) even for optimal misfit parameter  $\varepsilon^*_{opt}$  there is the region for the parameter  $t$  with no energy release. It is useful to note that optimal misfit parameter  $\varepsilon^*_{opt}$  does not vary much with the change of  $\Gamma$ . In the same time the radii ratio  $t$  giving the maximum energy release at optimal  $\varepsilon^*_{opt}$  varies substantially with  $\Gamma$ .

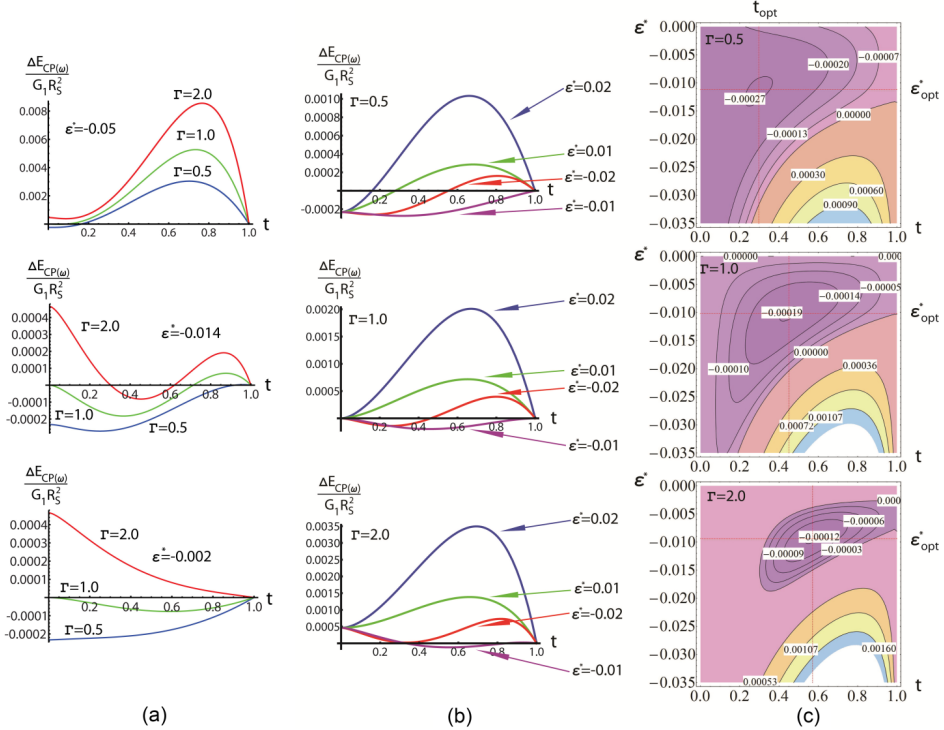


**Figure 11.** Formation of mismatched shell layer in pentagonal nanorods (PNRs): (a) energy release per unit length  $\Delta E_{CP(\omega)}$  as a function of the core/shell radii ratio  $t$  with different misfit parameters  $\varepsilon^*$  and ratios of shear modules  $\Gamma$ . Here  $\nu_1=\nu_2=0.3$ . Energy release per unit length  $\Delta E_{CP(\omega)}$  for shelled PNR with different  $\Gamma=G_2/G_1$ : (b) energy release  $\Delta E_{CP(\omega)}$  as a function of the core/shell radii ratio  $t$  with different misfit parameters  $\varepsilon^*$ ; (c) contours of equal energy release  $\Delta E_{CP(\omega)}$  as a function of  $t$  and  $\varepsilon^*$ .  $G_1$ ,  $\nu_1$ ,  $G_2$ ,  $\nu_2$  are the shear modules and Poisson's ratios of the core and shell correspondingly,  $\Gamma$  varies from 0.5 to 2 and  $\nu_1=\nu_2=0.3$ .

### 3.1.4. The role of core/shell interface energy

Let us introduce now the energies of free surface and interface in core/shell PNR (or INP):

$$E_\gamma = \gamma S, \quad (45)$$

where  $\gamma$  is a free surface energy per unit area or an interface energy per unit area and  $S$  is an area of the free surface or interface. It will be demonstrated that the introduction of surface energy terms enables to define the threshold radius of PNR(or INP), at which the formation of lattice mismatched shell becomes energetically favorable.

### 3.1.5. Threshold radius for mismatched crystal lattice layer formation in PNR

Assuming the energies of free surface for shelled PNR and unshelled PNR being equal there will be only one additional term in the energy balance caused by the interface energy:

$$E_{\gamma(\omega)} = 2\pi\gamma R_C. \quad (46)$$

As a result, the energy release  $\Delta E_{CP(\omega)}$  from Eq. (44) transforms to  $\Delta E_{CP(\omega)}^\gamma$ :

$$\Delta E_{CP(\omega)}^\gamma = (E_\omega + E_{\varepsilon^*} + E_{\omega-\varepsilon^*} + E_{\gamma(\omega)}) - E_\omega^0, \quad (47)$$

where all energies are per unit length of PNR.

The criteria for determining the threshold radius  $\check{R}_S$  can be written as following:

$$\left\{ \begin{array}{l} \Delta E_{CP(\omega)}^\gamma(R_S) = 0 \\ \frac{\partial \Delta E_{CP(\omega)}^\gamma(R_S)}{\partial t} = 0 \\ \frac{\partial \Delta E_{CP(\omega)}^\gamma(R_S)}{\partial \varepsilon^*} = 0 \\ 0 < t < 1. \end{array} \right. \quad (48)$$

The value of threshold radius depends on the elastic modules of the core and shell (Fig. 12). For the system with  $\Gamma=0.5$  the threshold radius defined by Eqs. (48) does not appear at all. For  $\Gamma > 1$  it increases with  $\Gamma$ . The reason of that can be understood as ‘‘predefined’’ energetically favorability of a PNR to transform into a PNR with lower shear modulus. From Eq. (48), for example, for Cu PNR

( $\gamma=0.625 \text{ Jm}^{-2}$ ,  $G=5.46 \times 10^{10} \text{ Pa}$ , [55]) the threshold radii are  $\check{R}_S \approx 108 \text{ nm}$  (Fig. 12b) and  $\check{R}_S \approx 320 \text{ nm}$  (Fig. 12c), respectively. The formation of shell layer with the mismatch parameter  $\varepsilon^*$  close to the optimal value is energetically favorable for PNRs with  $R_p > \check{R}_S$ .

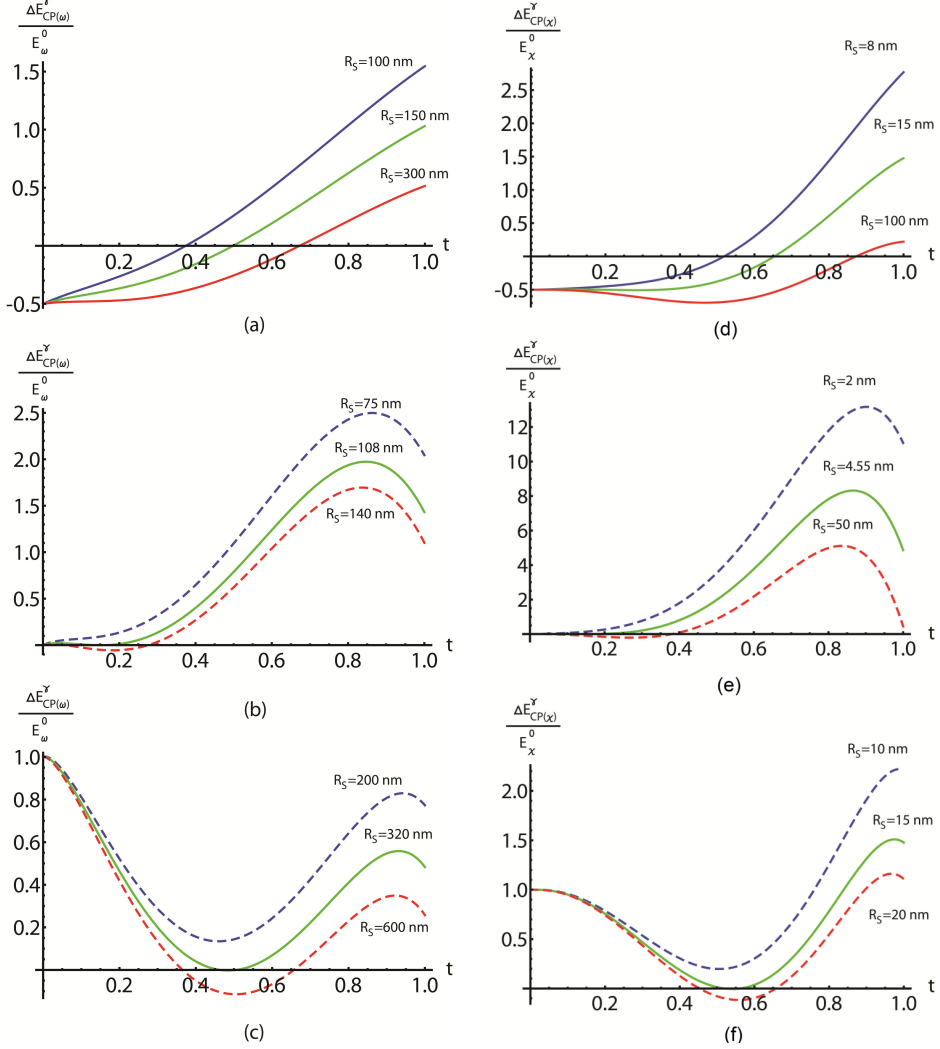


**Figure 12.** Typical diagram of the energy release in PNR (a,b,c) per unit length  $\Delta E_{CP(\omega)}^\gamma$  and INP (d,e,f)  $\Delta E_{CP(\chi)}^\gamma$  in the units of the initial energy of PNR  $E_\omega^0$  and INP  $E_\chi^0$  for shelled pentagonal nanocrystals with the interface energy  $\gamma$  taken into account with different  $\Gamma=G_2/G_1$ : (a) misfit parameter  $\varepsilon^*=-0.019$ ,  $\Gamma=1$ ; (b)  $\varepsilon^*=-0.0112$ ,  $\Gamma=0.5$ ; (c)  $\varepsilon^*=-0.011$ ,  $\Gamma=2$ , (d)  $\varepsilon^*=-0.121$ ,  $\Gamma=1$ ; (e)  $\varepsilon^*=-0.049$ ,  $\Gamma=0.5$ ; (f)  $\varepsilon^*=-0.045$ ,  $\Gamma=2$ . For these plots  $\gamma=0.625 \text{ J}\times\text{m}^{-2}$ , shear module of core  $G_1=5.46 \times 10^{10} \text{ Pa}$ , Poisson's ratio of core and shell  $\nu_1=\nu_2=0.3$ .

### 3.2. Pentagonal nanoparticles with crystal lattice mismatch layer

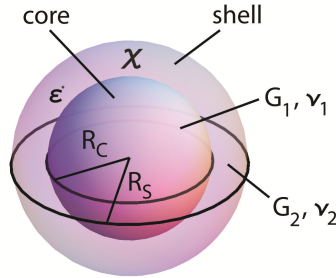
Fig. 13 represents mechanical model of shelled INP as a two-phase spheroid, including the distributed Marks-Yoffe disclination with strength  $\chi$  and dilatational spherical inclusion with eigenstrain  $\varepsilon^*$  that corresponds to the crystal lattice mismatch layer. The elastic field generated in shelled INP, for example stresses  $\sigma_{ij}$ , can be considered as a superposition of the disclination field  $\sigma_{ij}(\chi)$  and the field  $\sigma_{ij}(\varepsilon^*)$  due to the mismatched layer.

In order to find the elastic fields and energy of the INP with lattice mismatched layer, the boundary value problem similar to the problem for PNR must be solved.

The total elastic energy of the shelled INP consists of the following terms:

$$E_{CP(\chi)} = E_{\chi} + E_{\varepsilon^*} + E_{\chi-\varepsilon^*}, \quad (49)$$

where  $E_{\chi}$  is the energy of the distributed disclination in two-phase spheroid,  $E_{\varepsilon^*}$  is the energy of two-phase spheroid with mismatched layer (spherical inclusion with eigenstrain  $\varepsilon^*$ ) in a free spheroid, and  $E_{\chi-\varepsilon^*}$  is an interaction energy between the distributed disclination and the mismatched layer.



$$t = \frac{R_C}{R_S}, \quad \Gamma = \frac{G_2}{G_1}$$

**Figure 13.** Formation of the shell layer with crystal lattice mismatch in INPs. INP with mismatched shell layer.  $G_1, \nu_1, G_2, \nu_2$  are the shear modules and Poisson's ratios of the core and shell correspondingly;  $R_C$  is a core radius;  $R_S$  is a shell radius and  $\varepsilon^*$  is a lattice misfit parameter.

### 3.2.1. Solution for distributed disclination in two-phase spheroid. Stresses and energy

The overall idea for the calculation is similar to described in the paragraph 1.2.2. But in this case we give the displacement field in the both regions as following:

$$u_{r(\chi)}^{(1)} = \frac{2\chi}{3} \left( \frac{1-2\nu_1}{1-\nu_1} \right) r \ln r + B_1 r + C_1 / r^2 \quad (50a,b)$$

$$u_{r(\chi)}^{(2)} = \frac{2\chi}{3} \left( \frac{1-2\nu_2}{1-\nu_2} \right) r \ln r + B_2 r + C_2 / r^2$$

for the total displacement in the core and the shell, respectively.

Boundary conditions for the displacements and stresses are written as:

$$u_{r(\chi)}^{(1)} \Big|_{r=0} = 0 \quad (51a)$$

$$u_{r(\chi)}^{(1)} \Big|_{r=R_C} = u_{r(\chi)}^{(2)} \Big|_{r=R_C} \quad (51b)$$

$$\sigma_{rr(\chi)}^{(1)} \Big|_{r=R_C} = \sigma_{rr(\chi)}^{(2)} \Big|_{r=R_C} \quad (51c)$$

$$\sigma_{rr(\chi)}^{(2)} \Big|_{r=R_S} = 0. \quad (51d)$$

Now the system of Eqs. (51) can be solved for coefficients  $B_1, C_1, B_2$  and  $C_2$  (see the Appendix A5 for details). The expressions found for mechanical stresses  $\sigma_{ij(\chi)}$  due to the distributed disclination in the two-phase spheroid are:

$$\sigma_{rr(\chi)}^{(1)} = \frac{4\chi G_1 (2\nu_1^2 + \nu_1 - 1)}{3(1-\nu_1)(1-2\nu_1)(G_1(1+\nu_1)(-2t^3 + \nu_2(4t^3 - 1) - 1) + 2G_2(1+\nu_2)(1-2\nu_1)(t^3 - 1))} \cdot \left\{ G_1(1+\nu_1)(-\ln(t) - \ln(R_s r^{-1}) + 1)(-2t^3 + \nu_2(4t^3 - 1) - 1) - G_2(1+\nu_2) \left[ (2t^3 + 1) \ln(t) + 2t^3 \ln(R_s r^{-1}) - 2 \ln(R_s r^{-1}) \right] + \nu_1 \left[ (1 - 4t^3) \ln(t) - 4t^3 \ln(R_s r^{-1}) + 4 \ln(R_s r^{-1}) \right] \right\} \quad (52a)$$

$$\sigma_{rr(\chi)}^{(2)} = \frac{4\chi G_2(2\nu_2^2 + \nu_2 - 1)}{3(1-\nu_2)(1-2\nu_2)(G_1(1+\nu_1)(-2t^3 + \nu_2(4t^3 - 1) - 1) + 2G_2(1+\nu_2)(1-2\nu_1)(t^3 - 1))} \cdot \left\{ G_1(1+\nu_1) \left[ 2t^3 \ln(t) + 2t^3 \ln(R_s r^{-1}) + \ln(R_s r^{-1}) \right] + \nu_2(-4t^3 \ln(t) - 4t^3 \ln(R_s r^{-1}) + \ln(R_s r^{-1})) - 2(1-2\nu_2)t^3 \ln(t)R_s^3 r^{-3} \right\} + 2G_2(1+\nu_2)(1-2\nu_1) \left\{ [-t^3 \ln(t) - t^3 \ln(R_s r^{-1}) + \ln(R_s r^{-1}) - 1] + t^3 \ln(t)R_s^3 r^{-3} \right\} \quad (52b)$$

$$\sigma_{\theta\theta(\chi)}^{(1)} = \sigma_{\varphi\varphi(\chi)}^{(1)} =$$

$$\frac{2\chi G_1(2\nu_1^2 + \nu_1 - 1)}{3(1-\nu_1)(1-2\nu_1)(G_1(1+\nu_1)(-2t^3 + \nu_2(4t^3 - 1) - 1) + 2G_2(1+\nu_2)(1-2\nu_1)(t^3 - 1))} \cdot \left\{ G_1(1+\nu_1)(-2 \ln(t) - 2 \ln(R_s r^{-1}) + 1)(-2t^3 + \nu_2(4t^3 - 1) - 1) - 2G_2(1+\nu_2) \left[ (-t^3 + 2t^3 \ln(t) + 2t^3 \ln(R_s r^{-1}) - 2 \ln(R_s r^{-1})) + \nu_1((1-4t^3) \ln(t) - 4t^3 \ln(R_s r^{-1}) + 4 \ln(R_s r^{-1}) + 2(t^3 - 1)) + 1 \right] \right\} \quad (52c)$$

$$\sigma_{\theta\theta(\chi)}^{(2)} = \sigma_{\varphi\varphi(\chi)}^{(2)} =$$

$$\frac{2\chi G_2(2\nu_2^2 + \nu_2 - 1)}{3(1-\nu_2)(1-2\nu_2)(G_1(1+\nu_1)(-2t^3 + \nu_2(4t^3 - 1) - 1) + 2G_2(1+\nu_2)(1-2\nu_1)(t^3 - 1))} \cdot \left\{ G_1(1+\nu_1) \left[ 4t^3 \ln(t) + 4t^3 \ln(R_s r^{-1}) - 2t^3 + 2 \ln(R_s r^{-1}) \right] - \nu_2(8t^3 \ln t - 8t^3 \ln(R_s r^{-1}) + 4t^3 + 2 \ln(R_s r^{-1}) - 1) + 2(1-2\nu_2)t^3 \ln(t)R_s^3 r^{-3} \right\} - 2G_2(1+\nu_2)(1-2\nu_1) \left\{ [-2t^3 \ln(t) - 2t^3 \ln(R_s r^{-1}) + t^3 + 2 \ln(R_s r^{-1}) - 1] + t^3 \ln(t)R_s^3 r^{-3} \right\} \quad (52d)$$

Here upper indexes (1) and (2) mean core and shell correspondingly;  $t=R_C/R_S$ ,  $R_C$  is a core radius of spheroid and  $R_S$  is shell radius of spheroid;  $r$  is a radial coordinate of spheroid.

Elastic energy  $E_\chi$  of the distributed disclination of two-phase spheroid can be written in following form:

$$E_\chi = \frac{8\pi\chi^2 R_s^3}{27(1-\nu_1)(1-\nu_2)(G_1(1+\nu_1)(-2t^3 + \nu_2(4t^3 - 1) - 1) + 2G_2(1+\nu_2)(1-2\nu_1)(t^3 - 1))} \cdot \left\{ -G_1^2(1+\nu_1)^2 t^3 [-6\nu_2 t^3 + 2t^3 + \nu_2^2(4t^3 - 1) + 1] - 2G_2^2(1+\nu_2)^2(1+\nu_1)(2\nu_1 - 3) \left[ (t^3 - 1)^2 - 9t^3 \ln^2(t) \right] + G_1 G_2(1+\nu_1)(1+\nu_2) \cdot \left[ \nu_1(-6t^6 + 18t^3 \ln^2(t) + 5t^3 + \nu_2(8t^6 - 36t^3 \ln^2(t) - 9t^3 + 1) + 1) + \nu_2(-6t^6 + 36t^3 \ln^2(t) + 7t^3 - 1) + 4t^6 - 18t^3 \ln^2(t) - 3t^3 - 1 \right] \right\} \quad (53)$$

Let us consider a practically important case  $\nu_1 = \nu_2 = \nu$ . Then the energy of Marks-Yoffe disclination yields:

$$E_\chi = \frac{8\pi G_1^3 R_s^3 (1+\nu)\chi^2 (2 + \Gamma(1+\nu) - 4\nu - 18(\Gamma-1)(2\nu-1)t^3(\ln t)^2 - ((\Gamma-1)t^3 + 1)(2(\Gamma-1)(2\nu-1)t^3))}{27\Gamma t^3(1-\nu)(2-4\nu + \Gamma(1+\nu) + 2(\Gamma-1)(1-2\nu)t^3)} \quad (54)$$

### 3.2.2. Solution for spheroid with crystal lattice mismatched layer. Stresses and energy

Formation of mismatched shell layer in INP leads to eigenstrain in the shell region  $\varepsilon^*$ . Consequently, plastic displacements in the spheroid representing the INP are written as:

$$\hat{u}_r^{(1)} = 0, \quad \hat{u}_\theta^{(1)} = \hat{u}_\phi^{(1)} = 0. \quad (55a)$$

$$\hat{u}_r^{(2)} = -\varepsilon^* r, \quad \hat{u}_\theta^{(2)} = \hat{u}_\phi^{(2)} = 0. \quad (55b)$$

Elastic displacements are:

$$u_r^{(1)} = Ar, \quad u_\theta^{(1)} = u_\phi^{(1)} = 0. \quad (56a)$$

$$u_r^{(2)} = \frac{B}{r^2} + Cr, \quad u_\theta^{(2)} = u_\phi^{(2)} = 0, \quad (56b)$$

where

$$A = \frac{2\varepsilon^*(1-t^3)(1-2\nu_1)(1+\nu_2)}{\Gamma(1+\nu_1)((4\nu_2-2)t^3 - \nu_2 - 1) - 2(1-t^3)(1-2\nu_1)(1+\nu_2)} \quad (57a)$$

$$B = \frac{\varepsilon^* t^3 R_s^3 (1+\nu_1)(1+\nu_2)}{2(1-t^3)(1-2\nu_1)(1+\nu_2)/\Gamma + (1+\nu_1)(1+\nu_2 - (4\nu_2-2)t^3)} \quad (57b)$$

$$C = \frac{2\varepsilon^* t^3 (1+\nu_1)(1-2\nu_2)}{2(1-t^3)(1-2\nu_1)(1+\nu_2)/\Gamma + (1+\nu_1)(1+\nu_2 - (4\nu_2-2)t^3)}. \quad (57c)$$

The corresponding strain tensor components have the form:

$$\varepsilon_{rr}^{(1)} = -\frac{2\varepsilon^*(1-t^3)(1-2\nu_1)(1+\nu_2)}{(2-4\nu_1 + \Gamma(1+\nu_1))(1+\nu_2) - 2t^3((1-2\nu_1)(1+\nu_2) - \Gamma(1+\nu_1)(1-2\nu_2))} \quad (58a)$$

$$\varepsilon_{rr}^{(2)} = -\frac{2\varepsilon^* t^3 \Gamma(1+\nu_1)((1+\nu_2)R_s^3/r^3 - (1-2\nu_2))}{(2-4\nu_1 + \Gamma(1+\nu_1))(1+\nu_2) - 2t^3((1-2\nu_1)(1+\nu_2) - \Gamma(1+\nu_1)(1-2\nu_2))} \quad (58b)$$

$$\varepsilon_{\theta\theta}^{(1)} = \varepsilon_{\phi\phi}^{(1)} = -\frac{2\varepsilon^*(1-t^3)(1-2\nu_1)(1+\nu_2)}{(2-4\nu_1 + \Gamma(1+\nu_1))(1+\nu_2) - 2t^3((1-2\nu_1)(1+\nu_2) - \Gamma(1+\nu_1)(1-2\nu_2))} \quad (58c)$$

$$\varepsilon_{\theta\theta}^{(2)} = \varepsilon_{\phi\phi}^{(2)} = \frac{\varepsilon^* t^3 \Gamma(1+\nu_1)((1+\nu_2)R_s^3/r^3 + 2(1-2\nu_2))}{(2-4\nu_1 + \Gamma(1+\nu_1))(1+\nu_2) - 2t^3((1-2\nu_1)(1+\nu_2) - \Gamma(1+\nu_1)(1-2\nu_2))}. \quad (58d)$$

The stresses of spheroid with mismatched layer or, as we noted above, spherical inclusion with eigenstrain  $\varepsilon^*$  in free spheroid, are:

$$\sigma_{rr}^{(1)}(\varepsilon^*) = \sigma_{\theta\theta}^{(1)}(\varepsilon^*) = \sigma_{\phi\phi}^{(1)}(\varepsilon^*) = -\frac{4\varepsilon^* G_1 G_2 (1+\nu_1)(1+\nu_2)(t^3-1)}{G_1(1+\nu_1)(-2t^3+\nu_2(4t^3-1)-1)+2G_2(1+\nu_2)(1-2\nu_1)(t^3-1)} \quad (59a)$$

$$\sigma_{rr}^{(2)}(\varepsilon^*) = -\frac{4\varepsilon^* G_1 G_2 (1+\nu_1)(1+\nu_2)t^3(1-R_s^3 r^{-3})}{G_1(1+\nu_1)(-2t^3+\nu_2(4t^3-1)-1)+2G_2(1+\nu_2)(1-2\nu_1)(t^3-1)} \quad (59b)$$

$$\begin{aligned} \sigma_{\theta\theta}^{(2)}(\varepsilon^*) &= \sigma_{\phi\phi}^{(2)}(\varepsilon^*) = \\ &= -\frac{2\varepsilon^* G_1 G_2 (1+\nu_1)(1+\nu_2)t^3(2+R_s^3 r^{-3})}{G_1(1+\nu_1)(-2t^3+\nu_2(4t^3-1)-1)+2G_2(1+\nu_2)(1-2\nu_1)(t^3-1)}. \end{aligned} \quad (59c)$$

The elastic energy of two-phase spheroid with mismatched layer  $E_{\varepsilon^*}$  is:

$$E_{\varepsilon^*} = \frac{8\pi\varepsilon^{*2} G_1 G_2 (1+\nu_1)(1+\nu_2)t^3(t^3-1)R_s^3}{G_1(1+\nu_1)(-2t^3+\nu_2(4t^3-1)-1)+2G_2(1+\nu_2)(1-2\nu_1)(t^3-1)}. \quad (60)$$

Thus, the energy of interaction between the distributed disclination and mismatched layer in INP has a following simple expression:

$$E_{\chi}^{\text{int}} = \frac{16\pi^3 \varepsilon^* \chi \ln(t) G_1 G_2 R_s^3 (\nu_1+1)(\nu_2+1)}{G_1(\nu_1+1)(-2t^3+(4t^3-1)\nu_2-1)-2(t^3-1)G_2(2\nu_1-1)(\nu_2+1)}. \quad (61)$$

### 3.2.3. Conditions for mismatched layer formation in INP

Energy release  $\Delta E_{CP(\chi)}$  after formation of the mismatching layer in INP is defined as:

$$\Delta E_{CP(\chi)} = (E_{\chi} + E_{\varepsilon^*} + E_{\chi-\varepsilon^*}) - E_{\chi}^0, \quad (62)$$

where  $E_{\chi}^0$  is the energy of the unshelled INP with radius  $R_s$ . Fig. 14 gives the energy release for INPs calculated in accordance with Eq. (62). The optimal parameters  $\varepsilon_{opt}^*$  and  $t_{opt}$  at which the energy release is maximal have been found numerically and, for example, for equal elastic modules of core and shell are  $\varepsilon_{opt}^* \approx -0.04$  and  $t_{opt} \approx 0.59$ . All observations we made about the role of parameter  $\Gamma$  for PNRs (see section 3.1) remain true for INPs.

It should be noted that the core-shell model justifies the hollow-core model of relaxation in pentagonal crystals suggested by Romanov *et al.* in [14]. Hollow-core can be treated as a material with shear model  $G_1$  equal to 0. In the terms of our model the definition of initial state PNR or INP would need to be changed correspondingly to have elastic modules  $G_2$  and  $\nu_2$ . The resulted expression for energy release for both PNR and INP shows energetic favorability of formation of hollow-core in all the range of core radius parameter.

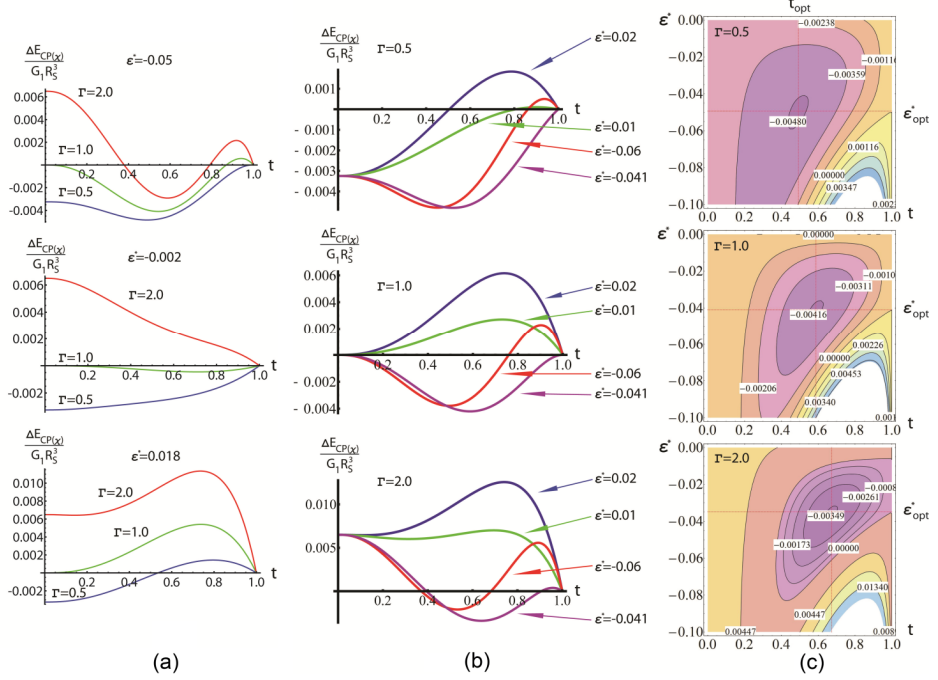


**Figure 14.** Energy release  $\Delta E_{CP(\lambda)}$  in a INP as a function of the core/shell radii ratio  $t$  with different misfit parameters  $\varepsilon^*$  and ratios of shear modules  $\Gamma$ , where  $\nu_1=\nu_2=0.3$  (a). Energy release per unit length  $\Delta E_{CP(\lambda)}$  for shelled INP with different  $\Gamma=G_2/G_1$ : (b) energy release  $\Delta E_{CP(\lambda)}$  as a function of the core/shell radii ratio  $t$  with different misfit parameters  $\varepsilon^*$ ; (c) contours of equal energy release  $\Delta E_{CP(\lambda)}$  as function of  $t$  and  $\varepsilon^*$ .  $G_1$ ,  $\nu_1$ ,  $G_2$ ,  $\nu_2$  are the shear modules and Poisson's ratios of the core and shell correspondingly,  $\Gamma$  varies from 0.5 to 2 and  $\nu_1=\nu_2=0.3$ .

### 3.2.4. Threshold radius for mismatched crystal lattice layer formation in INP

The interface energy term for INPs can be introduced in the same manner as it was done in the paragraph 3.1.5:

$$E_{\gamma(\lambda)} = 4\pi R_c^2. \quad (63)$$

Hence, the energy release  $\Delta E_{CP(\lambda)}$  for INP with the additional interface energy from Eq. (63) yields:

$$\Delta E_{CP(\lambda)}^\gamma = (E_\lambda + E_{\varepsilon^*} + E_{\lambda-\varepsilon^*} + E_{\gamma(\lambda)}) - E_\lambda^0. \quad (64)$$

For Cu INP ( $\gamma=0.625 \text{ J}\cdot\text{m}^{-2}$ ,  $G=5.46\cdot 10^{10} \text{ Pa}$ , [55]) the threshold radii obtained from Eqs. (48) and (64) are  $\check{R}_S\approx 4.6 \text{ nm}$  (see Fig. 12e) and  $\check{R}_S\approx 15 \text{ nm}$ , for Ag INP ( $\gamma=0.780 \text{ J}\cdot\text{m}^{-2}$ ,  $G=3.38\cdot 10^{10} \text{ Pa}$ , [55])  $\check{R}_S\approx 14 \text{ nm}$ . The formation of shell layer with the mismatch parameter  $\varepsilon^*$  close to the optimal value is energetically favorable for INPs with  $R_P > \check{R}_S$ .

In order to estimate the threshold radii of PNR and INP we took into account the interface energies only. In general case the difference in surface energies of unshelled and shelled PNR or INP should be considered.

It is worth noting that the core/shell pentagonal nanoparticles had been investigated by molecular dynamics simulation method [56, 57]. It was shown that for Cu-Ni and Cu-Pd systems [56] the location of “smaller” atoms of Cu in the core of icosahedral nanoclusters reduces the energy of the system. The Ag-Pd and Ag-Cu systems considered in [57] also confirmed that formation of shell with larger lattice parameter is energetically favorable.

### 3.3. Nanowhisker growth triggered by disclination

Grain boundary junctions in polycrystals possess elastic fields characteristic of disclinations [10, 58]. These fields become a source for such structural transformations associated with defect formation and defect motion. Formation of metallic nanowhiskers on the surface of polycrystals is often referred to as a relaxation of mechanical stresses stored in the material. On the other hand, as was described in the paragraph 1.3 PNCs are subject to relaxation processes due to mechanical stress in them as well. I would like to propose a new model that combines this idea with the advantages of the disclination approach. The model of nanowhisker growth proposed below is suitable for pentagonal crystals and bulk polycrystalline materials with micrograins and nanograins, junctions of which are known to form disclination-type structures [17].

This model of nanowhisker formation operates with prismatic dislocation loops that condensate on the disclination in the TB junction or in the grain boundaries of a polycrystal. Due to the formation of vacancy-type dislocation loops or pores in the bulk the excess material is then extruded at the surface in the form of nanowhiskers (Fig. 15). The model will be described in 2 steps. For the first of all, a system with single prismatic dislocation loop in the field of disclination is considered. Then one more prismatic dislocation loop of opposite sign is introduced. Calculation of elastic fields and energies is demonstrated for the both cases.

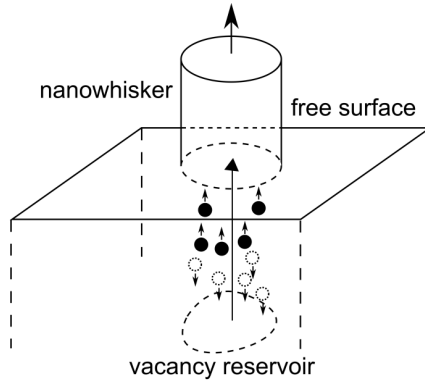


**Figure 15.** Schematics of the nanowhisker growth model. Sketch of the atom's flow motion to nanowhisker formation in the grain boundary junction.

### 3.3.1 Single dislocation loop in presence of a disclination source

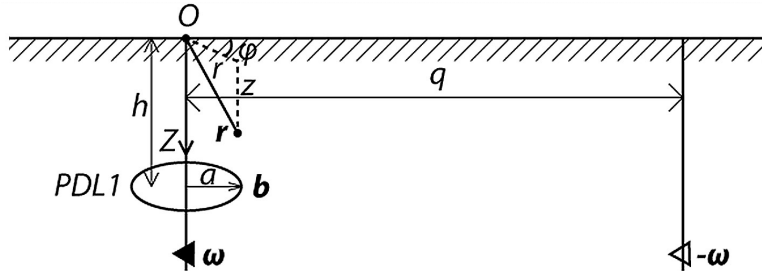


**Figure 16.** Half-space body with disclination dipole and prismatic dislocation loop *PDL1* coaxial with one of the disclinations.

Let us consider a half-space body with 2 wedge disclinations of powers  $\omega$  and  $-\omega$  (i.e. disclination dipole) perpendicular to the surface. The distance between the disclinations is  $q$ . The first disclination  $\omega$  (shown in Fig. 16) serves as a source of compressive stresses and is located coaxial to the growing nanowhisker, while the other is placed enough far, i.e. at a distance much greater than any size parameters used in the problem and used for “screening”. The elastic fields of a disclination dipole are well-known from [59]. The vertical component of the stress  $\sigma_{zz}$  field near the disclination line  $OZ$  ( $r \ll q$ ) can be written as (see Fig. 16):

$$\sigma_{zz} = -\frac{Gv\omega}{\pi(1-\nu)} \left( z \left( \frac{1}{\sqrt{r^2+z^2}} - \frac{1}{\sqrt{q^2+z^2}} \right) + \ln \left( \frac{\sqrt{q^2+z^2}+z}{\sqrt{r^2+z^2}+z} \right) + \ln \left( \frac{r}{q} \right) \right), \quad (65)$$

where  $G$  is the shear modulus and  $\nu$  is the Poisson's ratio of the body.

A prismatic dislocation loop *PDLI* with Burger's vector  $\mathbf{b}$  and radius  $a$  coaxial with the disclination line *OZ* is now introduced. Total elastic energy  $E_{\text{total}}$  of the system can be then expressed:

$$E_{\text{total}} = E_{\text{dcl}} + E_{\text{d-L1}} + E_{\text{L1}}, \quad (66)$$

where  $E_{\text{dcl}}$  is the elastic energy of the disclination dipole,  $E_{\text{L1}}$  is the elastic energy of the prismatic dislocation loop and  $E_{\text{d-L1}}$  is the interaction energy between them.

Therefore, the energy release  $E_{\text{rel}}$  after formation of the dislocation loop is:

$$E_{\text{rel}} = E_{\text{total}} - E_{\text{dcl}} = E_{\text{d-L1}} + E_{\text{L1}}. \quad (67)$$

The interaction energy  $E_{\text{int}}$  can be calculated as a work done by the elastic forces of the disclination dipole for inserting (removing) a disk of radius  $a$  and of thickness  $b$ :

$$E_{\text{d-L1}} = \int_0^a b \sigma_{zz} \cdot 2\pi r \, dr = \frac{Gb\nu\omega}{\nu-1} \left( h \left( \frac{a^2}{\sqrt{h^2+q^2}} - \sqrt{a^2+h^2} + h \right) - a^2 \ln \left( \frac{a \sqrt{h^2+q^2} + h}{q \sqrt{a^2+h^2} + h} \right) \right). \quad (68)$$

The elastic energy  $E_{\text{L1}}$  has the following form [60]:

$$E_{\text{L1}} = \frac{Gb^2a}{2(1-\nu)} \left[ \left( \ln \frac{8a}{r_{\text{core}}} - 2 \right) - \pi \left( J^{**}(1,1;0) \Big|_{r=a}^{z=h} + \frac{2h}{a} J^{**}(1,1;1) \Big|_{r=a}^{z=h} + \frac{2h^2}{a^2} J^{**}(1,1;2) \Big|_{r=a}^{z=h} \right) \right]. \quad (69)$$

Here  $r_{\text{core}}$  is the core cutoff radius of the loop and Lipshitz-Hankel integrals  $J^{**}(m,n;p)$  are defined as:

$$J^{**}(m,n;p) = \int_0^\infty J_m(\kappa) J_n \left( \kappa \frac{r}{a} \right) \exp \left( -\kappa \frac{|z+h|}{a} \right) \kappa^p d\kappa, \quad (70)$$

where  $J_m(\kappa)$  is the Bessel function.

The Lipshitz-Hankel integrals  $J^{**}(m,n;p)$  used in the Eq. (69) can be rewritten in terms of complete elliptic integrals according to [61]:

$$E_{\text{L1}} = \frac{Gb^2a}{2(1-\nu)} \left[ \left( \ln \frac{8a}{r_{\text{core}}} - 2 \right) - \frac{1}{2k^{1/2}} \left( K(k) \left( 4 - 2k + \frac{h^2k(k-4)}{a^2} \right) + E(k) \left( \frac{h^2k \left( 1 - 2k - \frac{3}{k-1} \right)}{a^2} - 4 \right) \right) \right], \quad (71)$$

where  $k=1/(h^2/a^2+1)$ ,  $K(k)$  and  $E(k)$  are complete elliptic integrals defined as:

$$K(k) = \int_0^{\pi/2} (1 - k^2 \sin^2 \phi)^{-1/2} d\phi \quad (72a)$$

$$E(k) = \int_0^{\pi/2} (1 - k^2 \sin^2 \phi)^{1/2} d\phi. \quad (72b)$$

The energy release  $E_{\text{rel}}$  after formation of the dislocation loop has been calculated numerically for a sample set of parameters (see Fig. 17). There is an area where  $E_{\text{rel}} < 0$  meaning that the formation of such dislocation loop is energetically favorable. One can notice that the radius of the loop  $a$  at the local negative minimum of  $E_{\text{rel}} < 0$  is of the same order as  $h$ .

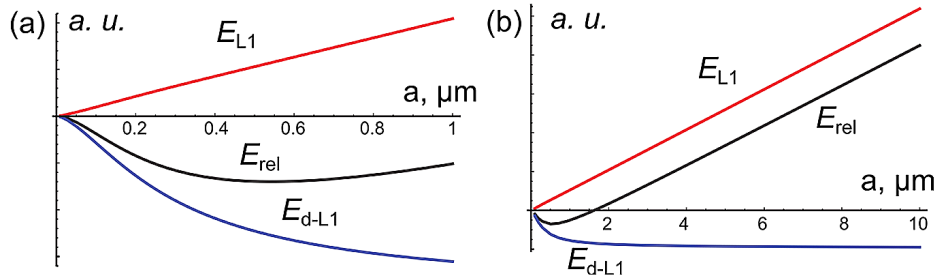


**Figure 17.** Diagrams of the energy of the dislocation loop  $E_{L1}$ , interaction energy  $E_{\text{d-L1}}$  and energy release  $E_{\text{rel}}$  as a function of radius of the dislocation loop  $a$  given in arbitrary units in different scales of  $a$ . Calculated for the case  $b=0.5$  nm,  $\omega=0.1$ ,  $\nu=0.3$ ,  $h=300$  nm,  $q=1$  m,  $r_{\text{core}}=0.4$  nm.

On the other hand, from the Fig. 18 one can see that formation of a dislocation loop of a given radius  $a$  becomes energetically favorable in distance of  $h > h^*$  where  $E_{\text{rel}}(h^*)=0$ .

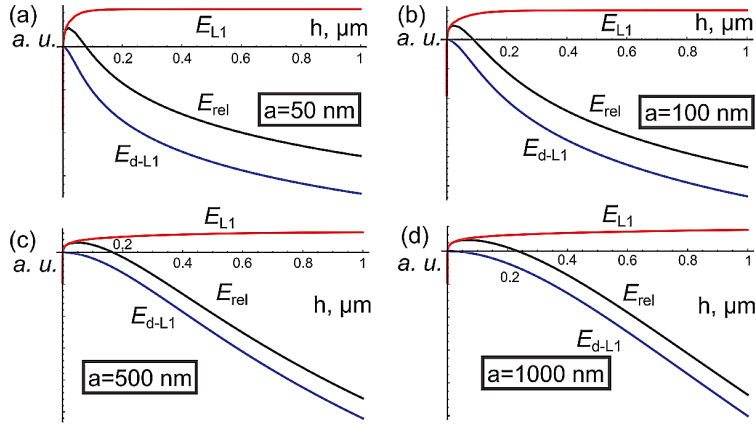


**Figure 18.** Diagrams of the energy of the dislocation loop  $E_{L1}$ , interaction energy  $E_{d-L1}$  and energy release  $E_{rel}$  as a function of the distance of the dislocation loop from the surface  $h$  given in arbitrary units with different radii of the dislocation loop  $a$ . Calculated for the case  $b=0.5$  nm,  $\omega=0.1$ ,  $\nu=0.3$ ,  $q=1$  m,  $r_{core}=0.4$  nm.

One should note that dependence of the energy release  $E_{rel}$  and its components from the distance  $q$  is negligible keeping the conditions  $a \ll q$  and  $h \ll q$ , i.e. dislocation loop is formed in a field of a “screened” disclination.

### 3.3.2. A pair of dislocation loops in presence of a disclination source

Let us now in addition to the system considered in the previous paragraph introduce another prismatic dislocation loop  $PDL2$  of radius  $a$  with Burgers vector  $-b$  is coaxial with the former dislocation loop and situated at the distance  $j$  from the surface (Fig. 19). The loop  $PDL2$  is of interstitial type and represents the collective flow of excess atoms towards the surface (Fig. 19).

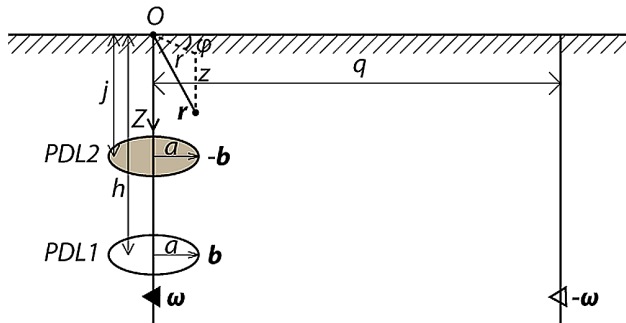


**Figure 19.** Half-space body with disclination dipole and two prismatic dislocation loops  $PDL1$  and  $PDL2$  coaxial with one of the disclinations.

Total elastic energy  $E_{\text{total}}$  of the body containing a disclination dipole and dislocation loops,  $PDL1$  and  $PDL2$ , can be expressed as the sum:

$$E_{\text{total}} = E_{\text{dcl}} + E_{L1} + E_{L2} + E_{\text{d-L1}} + E_{\text{d-L2}} + E_{L1-L2} \quad (73)$$

where  $E_{\text{dcl}}$  is the elastic energy of disclination dipole,  $E_{L1}$  and  $E_{L2}$  are the elastic energy of  $PDL1$  and  $PDL2$  correspondingly, interaction energy between the disclination dipole and  $PDL1$  ( $PDL2$ ) is denoted as  $E_{\text{d-L1}}$  ( $E_{\text{d-L2}}$ ), and  $E_{L1-L2}$  is interaction energy between  $PDL1$  and  $PDL2$ .

The energy release,  $E_{\text{rel}}$ , is defined as a difference between the initial elastic energy of a bare disclination dipole and the total elastic energy of the system after the formation of the dislocation loops  $PDL1$  and  $PDL2$ :

$$E_{\text{rel}} = E_{\text{total}} - E_{\text{dcl}} = E_{L1} + E_{L2} + E_{\text{d-L1}} + E_{\text{d-L2}} + E_{L1-L2} \quad (74)$$

$E_{L1}$  and  $E_{L2}$  can be found in analytical form in [59]. The interaction energies  $E_{\text{d-L1}}$  and  $E_{\text{d-L2}}$  are calculated as a work done by the elastic forces of the disclination dipole for removing or inserting a disk of radius  $a$  and thickness  $b$  at the position of  $PDL1$  or  $PDL2$ . The term  $E_{L1-L2}$  is determined as a work done by elastic forces of  $PDL1$  for inserting the same disk (or vice versa) at the position of  $PDL2$ . The expressions for the stress field of  $PDL1$  ( $PDL2$ ) are given, for example, in [60].

Calculation of  $E_{\text{d-L2}}$  and  $E_{L2}$  follows directly from Eqs. (68) and (69) by substitution of  $h$  with  $j$  and  $b$  with  $-b$ .

The term  $E_{L1-L2}$  involving elastic stress fields of  $PDL1$   $\sigma_{zz}^{L1}$  is expressed by:

$$E_{L1-L2} = \int_0^a b \sigma_{zz}^{L1} \cdot 2\pi r \, dr \quad (75)$$

The very expression for the stress component  $\sigma_{zz}^{L1}$  can be found in [60]:

$$\sigma_{zz}^{L1} = \frac{Gb}{2(1-\nu)} \left[ -\frac{1}{a} J^*(1,0;1) - \frac{|z-h|}{a^2} J^*(1,0;2) + \frac{1}{a} J^{**}(1,0;1) + \frac{z+h}{a^2} J^{**}(1,0;2) + \frac{2zh}{a^3} J^{**}(1,0;3) \right], \quad (76)$$

where Lipshitz-Hankel integrals  $J^*(m,n;p)$ .

We use [62] to rewrite the Lipshitz-Hankel integrals in terms of complete elliptic integrals that are more suitable for numeric computations.

In the Fig. 20a,b the diagrams demonstrate general behavior of the system with certain sample set of parameters. Both  $PDL1$  and  $PDL2$  are attracted to the free surface (see  $E_{L1}$  and  $E_{L2}$ ), although  $PDL1$  is also attracted deep into the body by the compressive stresses of the disclination and  $PDL2$  is extruded by them. Attraction between  $PDL1$  and  $PDL2$  follows from their opposite Burger's vectors. Interplay of these forces is described by the energy release  $E_{\text{rel}}$  as functions of  $j$  and  $h$  (Fig. 20). The diagrams clearly show a range of parameters

where  $E_{rel} < 0$ , which means that formation of *PDL1* and *PDL2* is energetically favorable versus the initial state of the body without them.

However in other cases, their formation requires overcoming of an energy barrier. Rearrangement of the separated dislocation loops is followed by gliding of *PDL1* downward to a vacancy reservoir (e.g. pore), and *PDL2* towards the surface contributing to the growth of the nanowhisker.

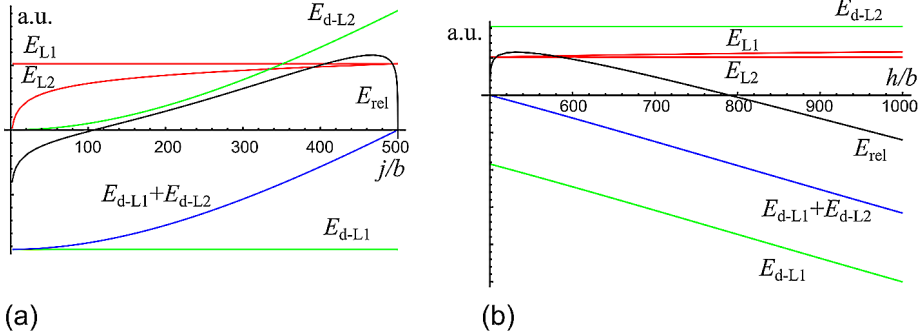


**Figure 20.** Diagrams of the energy of the dislocation loops  $E_{L1}$  and  $E_{L2}$ , the interaction energies  $E_{d-L1}$ , and  $E_{d-L2}$  and their sum, and the energy release  $E_{rel}$  as a functions of distance  $j$  in units of  $b$  with fixed  $h=500 \cdot b$  (a), as function of distance  $h$  in units of  $b$  with fixed  $j=500 \cdot b$  (b). The energy is given in arbitrary units, calculated for the case  $b=0.5$  nm,  $\omega=0.1$ ,  $a=500$  nm,  $r_{core}=0.4$  nm and typical values of the materials elastic properties.

### 3.4. Summary

In the chapter 3 a new mechanism of stress relaxation in PNRs (section 3.1) and INPs (section 3.2) was proposed in the framework of the disclination approach. On the base of our modeling and calculations it has been proved that formation of a shell layer with crystal lattice mismatch can diminish the internal energy of PNRs or INPs. Solution for the boundary value problem of elasticity was obtained for a wedge disclination (Marks-Yoffe disclination) in a core-shell cylinder and spheroid with different elastic moduli of core and shell. The elastic fields and energy of core-shell mismatch were solved for undisclinated cylinder and spheroid. Then the conditions of mismatch layer formation were proposed on the base of the two elastic fields and corresponding diagrams were demonstrated. Then the core/shell interface energy was introduced into consideration and the threshold radius for PNRs and INPs. The optimal mismatch parameter  $\varepsilon_{opt}^*$  giving the maximal energy release was determined as  $\varepsilon_{opt}^* \approx -0.01$  for PNR and  $\varepsilon_{opt}^* \approx -0.04$  for INP. The threshold radius as the minimal radius of nanorods or nanoparticles, for which the formation of the layer is energetically favorable was found to be approximately 10 nm for nanoparticles and 100 nm for nanorods of typical FCC metals.

In the section 3.3 a new model for nanowhisker growth was proposed. In this model the nanowhisker extruded from the material having compressing stresses originated from a disclination that might reside in a PNCs or grain boundary junction. For simplicity half-space with a wedge disclination dipole perpendicular to the surface was considered. The elastic fields and energy of a half-space with the disclination dipole is described. Then a single dislocation loop is introduced coaxial to the disclination line, elastic fields and energy are revealed. And finally, a second dislocation loop is invoked that is responsible for the extruding of the material in a form of nanowhisker. The elastic energy of the system with a pair of dislocation loops as a function of location and size of the loops.

## 4. TRIBOLOGICAL PROPERTIES OF 0D AND 1D NANOCRYSTALS

### 4.1. Simulation of icosahedral nanoparticles manipulation

#### 4.1.1. Computer program for numerical simulation

In the present paragraph a model of simulation of INP manipulation is demonstrated. The necessary theoretical background is described in the paragraph 1.5. The simulation comprises numerical solution of the equations of motion in the overdamped zero-temperature case. Two cases are considered: (a) nanoparticle on a plane is being manipulated by a concentrated force  $\mathbf{f}_p$  at the point  $\mathbf{r}_p$ ; (b) nanoparticle clutched between two planes, while the top plane is pressed by normal load  $\mathbf{f}_N$  and pulled by a spring  $\kappa$  with a constant velocity  $V$ .

In order to perform the calculations and present the results a computer program was developed. The main components of that program must be as following:

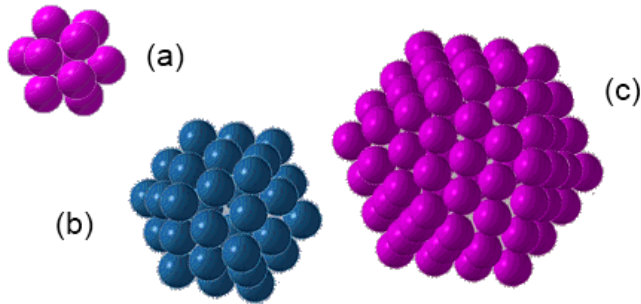
1. Integration algorithm for numerical solving of the equations of motion, therefore generating the state of the system at each moment  $t$  with time interval  $\Delta t$ . The state of the system includes the position of nanoparticle's center of mass  $\mathbf{r}$ , its rotation  $q$  for the both cases (a) and (b), and position of the top plane  $\mathbf{R}$  for the case (b).
2. Physical system's subroutines for calculation of the dissipation coefficients  $\eta_{B,T}$ , forces  $\mathbf{f}_{B,T}^{(i)}$  atom's positions  $\mathbf{r}_i'$ . The latter will account for the nanoparticle shape. In our case, only INPs are considered. However the size of the nanoparticle, i.e. number of icosahedral "layers" can be different.
3. Control panel for setting the physical parameters of the system: lattice constant for nanoparticle  $a_p$  and planes  $a$ , adhesion energy  $\epsilon$ , equilibrium separation from the surface  $\sigma$ , characteristic decay length  $\lambda$ , damping coefficient  $\eta_0$  and decay length  $\zeta$ . It also includes vector of point force  $\mathbf{f}_p$  and its application point  $\mathbf{r}_p$  for the case (a), and normal load  $f_N$ , velocity of the spring  $V$ , and spring constant  $\kappa$  for the case (b). Initial configuration of the system, i.e. position of the nanoparticle and top-plane can be also set. The mode of calculation – classical equations of motion or overdamped case can be chosen.
4. Visualization and analysis system for visual representation of the system evolution in time, and tools for analysis of the various system variables, such as friction force  $f$ .

The components stated above were realized in the frame of a single executable file. Let us consider some of the peculiarities in the implementation of each of the components.

Among all the available numerical algorithms of solving ordinary differential equations, one of the most widely used is so-called Runge-Kutta. In particular, classical Runge-Kutta (RK4) has an error on each step of order  $h^5$

and accumulated error of order  $h^4$ , where  $h$  is the integration step [63]. This RK4 method was chosen for the implementation of the simulation program.

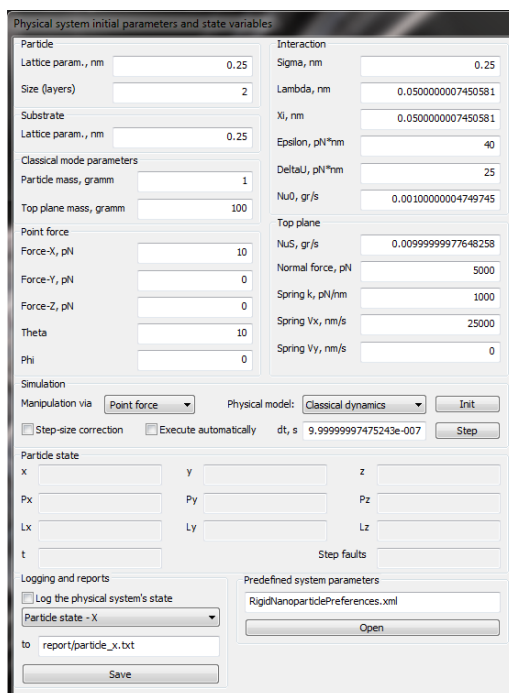
The subroutine for calculations of atom's positions is an important part of the 2<sup>nd</sup> component. In the current implementation, where only INPs are considered, this subroutine must give the atom's positions  $\mathbf{r}'_i$  of all the atoms for a nanoparticle of a given size. The size can be described as a number of icosahedral layers  $L$ . When  $L=0$ , the nanoparticle consists of a single atom (layer 0). When  $L=1$ , in addition to the central atom of the layer 0 a number of atoms arranged the way depicted in the Fig. 21a (layer 1). The length of the edge of the icosahedron is described by the nanoparticle lattice constant  $a_p$  and nanoparticle  $L=1$  consists of  $1+12=13$  atoms. In the case of  $L=2$ , the layer 2 is added up to the basis described by layers 0 and 1 with the same orientation of the icosahedron. The length of the edge in layer 2 is now  $2a_p$  and the nanoparticle consists of  $1+12+42=55$  atoms. This can be continued for larger  $L$  in analogous way as seen from the Fig. 21.



**Figure 21.** Schematics of atoms in an icosahedral nanoparticle: with 1 layers, 13 atoms (a), with 2 layers, 55 atoms (b), with 3 layers, 147 atoms (c).

Control panel has been implemented to set up physical parameters in a graphical user interface before the simulation start (Fig. 22). It also allows monitoring current state of the physical system during the simulations and seeing such variables like nanoparticle position, momentum and angular momentum. It should be noted, that the choice of the initial rotation of the nanoparticle does not really influence the long-term motion of the system, because in relatively short time the nanoparticle rolls and occupies an energetically favorable position. In the current implementation in the initial state the icosahedron is “standing” upon one of the vertexes.

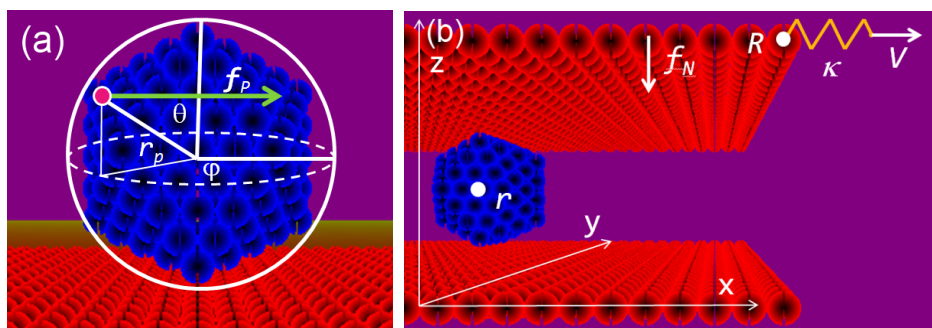
Visualization of the simulations has been realized in a form of 3D picture of the system with atomic spheres rendered to a graphical window and updating in real-time along the simulations. In the current version of the program, the simulation timeline is written in a corner.



**Figure 22.** Control panel for setting physical parameters of the simulation and monitoring the system state.

#### 4.1.2. Results of the simulations

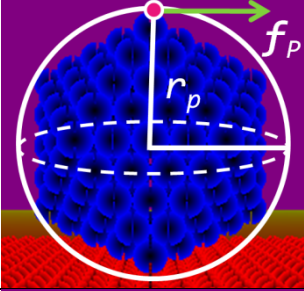
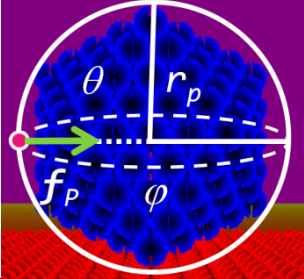
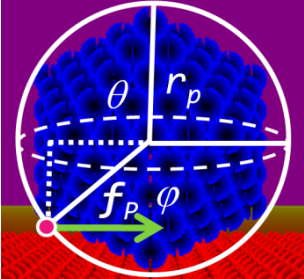
Let us now consider some of the results obtained with use of the numerical simulations described in the previous paragraph. The simulations were performed in the two manipulation regimes: point force and top plane (see Figure 23). The overdamped zero-temperature approximation was used all the time.



**Figure 23.** Schematics of the simulation regimes. The point force manipulation regime (a). The top plane manipulation regime (b).

In the point force regime, it makes sense to consider 3 main cases. In all these cases the point force is directed along  $X$  axis, however it is applied at different positions on the nanoparticle, therefore producing different torques (see Table 1 for details). The types of observed motion are also listed in the Table 1, where it can be clearly seen that the nanoparticle follows intuitively expectable directions of motion. In the case 2 the nanoparticle slides on a facet attracted by the surface.

**Table 1.** Schematics and results of the numerical simulation of manipulations of a nanoparticle with a point force applied at different locations of the nanoparticle. In all cases  $L=4$ ,  $\eta_0=10^{-6}$  kg/s,  $a=a_s=0.25$  nm and  $\zeta=\lambda=0.05$  nm were used.

No.	System parameters	Schematics	Types of nanoparticle's motion
1	$\mathbf{f}_p=(10, 0, 0)$ nN, $\theta=\varphi=0$ .		Rolling motion in the clock-wise direction.
2	$\mathbf{f}_p=(10, 0, 0)$ nN, $\theta=\pi/2$ , $\varphi=0$ .		After rolling to a facet, stable translational motion.
3	$\mathbf{f}_p=(20, 0, 0)$ nN, $\theta=3\pi/4$ , $\varphi=0$ .		Rolling motion in the counter-clockwise direction.

In the regime with the top plane the dependence of the nanoparticle's motion on the normal load is interesting to consider. According to the results listed in

Table 2, under higher normal load the nanoparticle slides without rolling (case 1), and with lower load the nanoparticle may roll (case 2).

It should be noted that the goal of this paragraph is to present the model for numerical simulations. The physical parameters used for the calculations listed in Tables 1 and 2, were not chosen to suit any particular real materials. Therefore, performing “realistic” simulations for different materials could be aims of new investigations. It could be also interesting to simulate nanoparticles of other shapes and compare the results.

**Table 2.** Results of the numerical simulation of manipulations of a nanoparticle clutched between two planes with the top plane dragged by a spring  $\kappa$  with constant velocity  $V$ . In all cases  $L=4$ ,  $\eta_0=10^{-5}$  kg/s,  $a=a_S=0.25$  nm and  $\zeta=\lambda=0.05$  nm were used.

No.	System parameters	Types of nanoparticle's motion
1	$f_N=300$ nN, $V=4 \cdot 10^5$ nm/s $\kappa=10$ N/m.	Sliding without rolling.
2	$f_N=10$ nN, $V=8 \cdot 10^5$ nm/s $\kappa=10$ N/m.	Rolling slowly.

## 4.2. Nanomanipulation experimental setup and force sensor

Experimental measurements considered in the present paper involve visually controllable manipulations (positioning and bending) of NPs and NWs inside SEM (Vega-II SBU, *TESCAN*; typical chamber vacuum  $3 \times 10^{-4}$  mbar). The manipulation tool comprised an AFM cantilever with a silicon tip (*NT-MDT*), etched 0.1 mm W wire [64] or chip with contact cantilever (Nanosensor ATEC-CONT cantilevers  $C=0.2$  N/m) connected to a 3D nanomanipulator (SLC-1720-S, *SmarAct*). The tip of the AdvancedTEC AFM probes is tilted about 15 degrees relative to the cantilever, providing tip visibility from the top.

For the nanomanipulation experiments described in paragraphs 4.3 and 4.4.2, a home-made force sensor was installed to measure the applied force. Force sensors were constructed in a manner similar to Rozhok *et al.* [65]. Force measurements were based on the fact that the oscillation amplitude of the sensor oscillating on its resonant frequency depends on the forces acting on the tip, i.e. so-called amplitude modulation. Sensor oscillations were excited by applying alternating voltage to its electrodes using a lock-in amplifier (SR830; *Stanford Research Systems*). The amplitude of free oscillations at the tip apex was on the order of 100 nm. The sensor also provided feedback to control the distance between the tip and the surface.

Depending on the side to which the tip was glued, the sensor operated in normal or shear modes. In normal mode, the QTF oscillated perpendicularly to the surface in a manner similar to a conventional AFM (Fig. 24a). In shear mode, the sensor oscillated parallel to the surface (Fig. 24b).

Such a sensor enables to measure the force applied by AFM tip to the NP or NW. The tip was electrically connected to the QTF electrode to exclude charging effects. To make the QTF response faster, the Q-factor was reasonably decreased by putting a small drop of epoxy resin (Ecobond 286, *Emerson & Cuming*) onto the opposite prong of the QTF. Thermal drift for given experimental set-up was on the order of 0.1 nm/sec and could thus be neglected within one manipulation event.

The signal from the QTF was amplified by the lock-in and recorded through the ADC-DAC card (NI PCI-6036E, *National Instruments*). The typical values of the driving voltage were 10–30 mV. The force sensitivity of the QTF was calibrated in both the *Y* and *Z* directions on reference contact AFM cantilevers (FCL, *AppNano* and CSG11  $C=0.03\text{--}0.1$  N/m, *NT-MDT*) inside the SEM similar to the procedures described in [66, 67]. The reference cantilevers were precalibrated by the thermal noise method [68].

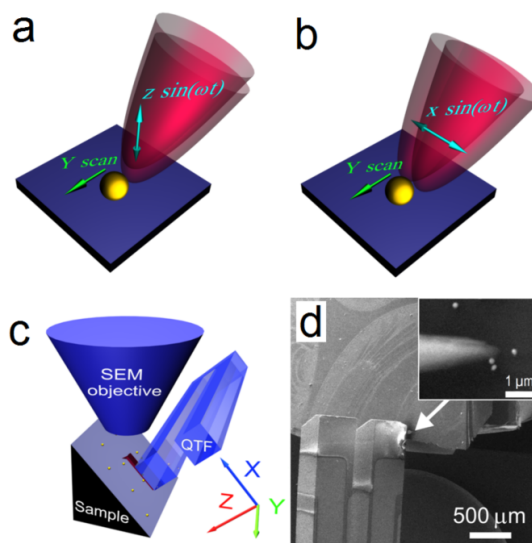


**Figure 24.** Tip oscillating in (a) Normal and (b) Shear modes. (c) QTF and sample tilted at 45 degrees to the SEM objective. (d) SEM image of the sample and QTF with AFM tip.

Special software was developed to control the nanomanipulator and record simultaneous signals from the nanomanipulator’s position sensors and signals from the force sensor (see the Fig. 25). More details on the force sensor, data acquisition and manipulator control used can be found in [69].

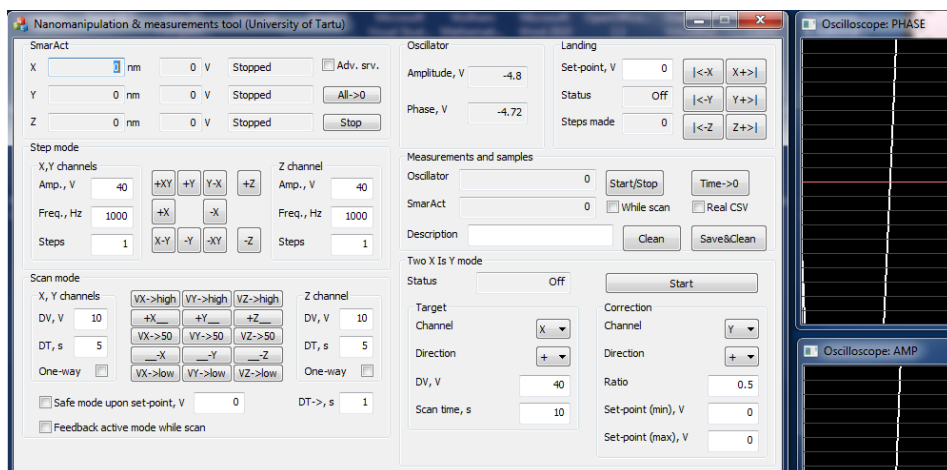


**Figure 25.** A screenshot of the control and measurement system panel for the nanomanipulation setup.

### 4.3. Manipulation of nanoparticles employed for tribological measurements

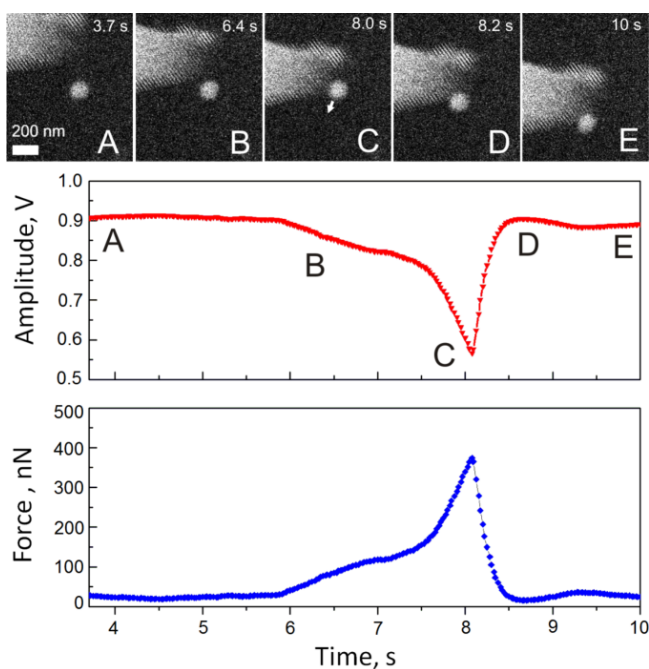
#### 4.3.1. Manipulation of gold nanoparticles in SEM

For manipulation experiment, the tip was brought into the close proximity to the chosen particle. The particle was then displaced (“kicked”) from its initial position by an abrupt tip motion in the step regime to reduce the initial adhesion [32], which is known to be time-dependent [70], to its minimal value. Initial displacement was followed by controlled manipulation of the particle by pushing it with the tip in scan regime with simultaneous force recording. During manipulation, the tip moved parallel to the surface along a straight line without feedback.

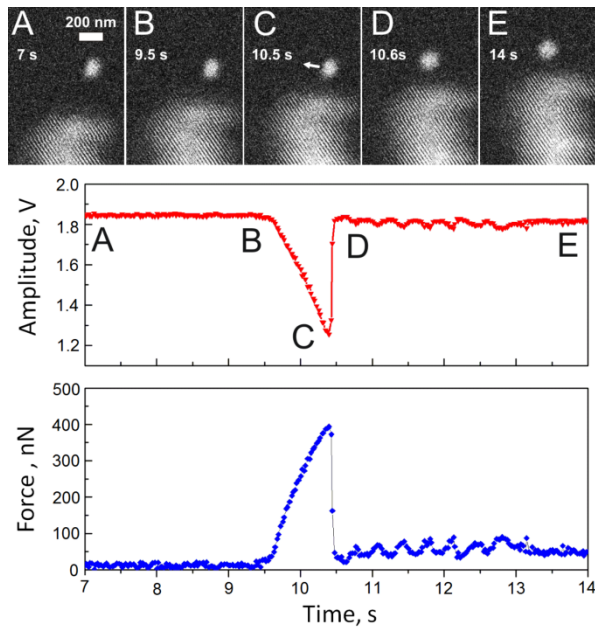
Figure 26 presents a typical manipulation curve for the QTF oscillating in the normal mode. The initial flat region **A-B** of the curves corresponds to the movement of the tip above the surface. Decline of the curve at region **B-C** was caused by a long-range interaction between the tip and the particle. The abrupt drop of the amplitude at **C** corresponds to the force needed to overcome the static friction and displace the Au particle from its initial location. When static friction was overcome, the particle jumped in the direction indicated by the arrow. From **D** to **E**, the particle moved smoothly with the tip. For the moving particle, the amplitude drop was only few percent lower than it was before the contact.

Figure 27 shows a manipulation curve for the QTF oscillating in the shear mode. The initial flat region from **A** to **B** of the curve corresponds to the movement of the tip at a constant set point above the surface. The abrupt drop in amplitude from **B** to **C** corresponds to the force needed to overcome static friction and displace the Au particle. The particle made a small jump in the direction indicated by the arrow. From **D** to **E**, the particle moved smoothly with the tip, and minor oscillations related to tip-particle interaction were noticeable.

In all manipulation experiments, the tip moved in the *Y* direction. We used the *Y*-direction force-calibration data to convert the amplitude to force (further details are given below). The static friction was found in the range from 40 to 450 nN for normal mode and from 50 to 750 nN for the shear mode. It should be noted that the oscillation amplitude often dropped to zero. This drop corresponds to the force higher than 1500–2500 nN (the upper limit depending on the particular sensor). Forces higher than these limits could not be measured due to the limited range of QTF sensitivity at a given driving voltage.



**Figure 26.** Snapshots of the manipulation process and corresponding amplitude and force curves, Normal mode (sample tilt corrected).



**Figure 27.** Snapshots of the manipulation process and corresponding amplitude and force curves, Shear mode.

Figure 28 displays a distribution histogram of the static friction forces for the manipulation experiments in the normal and shear modes. The static friction values for the cases when the amplitude dropped to zero remain unknown and thus could not be included in the histogram.

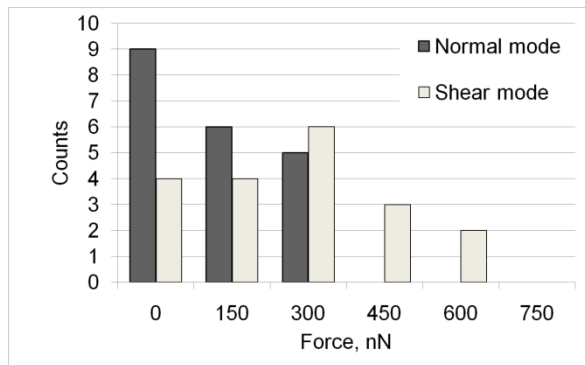


**Figure 28.** Distribution of static friction forces based on 20 manipulation events in Normal mode and 17 manipulation events in Shear mode.

### 4.3.2. Structure and tribology of gold nanoparticles

From the experimental results, it is evident that considerable force is needed to overcome static friction in this system. However, once the threshold for static friction was exceeded and the particle moved smoothly with the tip, then only minor changes in oscillation amplitude were observed in a few cases. Most of kinetic friction values were below the detection limits of our setup. This finding is in agreement with other researches, who have demonstrated that the kinetic friction is very small for clean surfaces in vacuum [71].

Variations in the experimental values of static friction may be due to the fact that the contact area between a particle and a substrate can vary due to deviations from a spherical shape. From Fig. 29a it is clearly seen, that Au particles used in the experiments were, in general, not spherical and had facets of different sizes.

Geometrical factors may also play a crucial role in the reduction of static friction after a thermal treatment. In our experiments, the main reason for heating the samples was to burn out the surfactant remaining after the deposition of the particles onto the substrate. However, it was found that the annealing at 773 K also led to a rounding of the particles (see Fig. 29b), which, in turn, should result in reduction of contact area and the static friction.

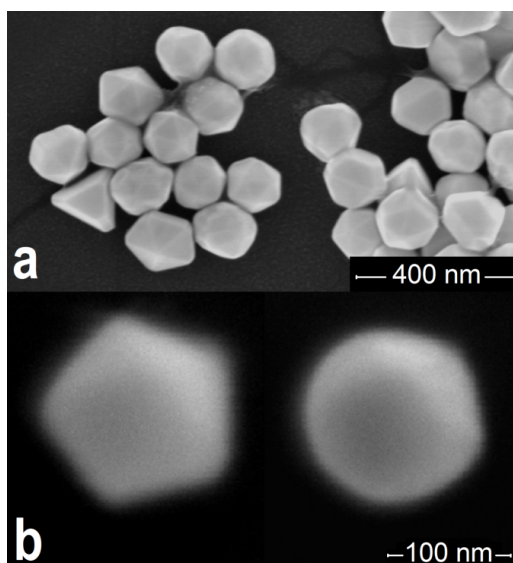


**Figure 29.** (a) Au particles of different shape as deposited from solution. (b) SEM micrograph of the same Au particle before and after annealing for 1 h at 773 K.

Here, we provide an analytical estimate of the static friction considering the geometric parameters [5] of the particles used in our manipulation experiments. It has theoretically proposed and experimentally proven that friction at the

nanoscale is proportional to the contact area:  $F_{frict} = \tau A$ , where  $A$  is the contact area and  $\tau$  is the shear strength [72].

For spherical particles, the contact area can be calculated on the basis of continuum elasticity models for deformable spheres [32] such as the JKR model [53] or the DMT model [54]. According to Tabor [73], the choice of the most suitable model is determined by the parameter:

$$\eta = \left( \frac{16R\gamma^2}{9K^2 z_0^3} \right)^{1/3}, \quad (77)$$

where  $R$  is the radius of the sphere,  $\gamma$  is the work of adhesion, and  $z_0$  is the equilibrium spacing for the Lennard-Jones potential of the surfaces.  $K$  is the reduced elastic modulus of the sphere and the substrate defined as  $K = \frac{4}{3}[(1-\nu_1^2)/E_1 + (1-\nu_2^2)/E_2]^{-1}$  in which  $\nu_{1,2}$  and  $E_{1,2}$  are the Poisson ratios and Young moduli of the substrate and sphere, respectively.

Assuming the following parameters for silicon and gold:  $E_1 = 71.7$  GPa,  $\nu_1 = 0.17$ ,  $E_2 = 78$  GPa,  $\nu_2 = 0.44$ ,  $\gamma = 50$  mJ/m<sup>2</sup> [32],  $R = 75$  nm and  $z_0 = 0.3$  nm, we obtained  $\eta = 0.158$ . For small  $\eta$ , the DMT-M theory is more appropriate [73]. According to the DMT-M model, the contact area

$$A_{DMT-M} = \pi \left( \frac{2\pi\gamma}{K} \right)^{2/3} R^{4/3} \quad (78)$$

for spherical Au NPs with  $R = 75$  nm is  $A_{DMT-M} \approx 31.43$  nm<sup>2</sup>.

The contact areas of the faceted NPs can be easily calculated using geometrical considerations. The results of the calculations for tetrahedral, decahedral and icosahedral NPs are presented in Table 3.

The shear strength  $\tau$  can be estimated using the relation  $\tau_{theo} = G^* / 30$  between the theoretical shear strength and the reduced shear modulus,  $G^* = [(2-\nu_1)/G_1 + (2-\nu_2)/G_2]^{-1}$ , where  $G_{1,2} = E_{1,2} / 2(1+\nu_{1,2})$  [43, 74]. The ultimate static friction can then be calculated as  $F_{frict} = \tau_{theo} A_{DMT-M}$ .

**Table 3.** Estimated static friction forces for 150 nm Au particles of different geometries.

Shape	Contact area, nm <sup>2</sup>	Static friction, nN
Spherical	31	9
Tetrahedral	9743	2768
Decahedral	3652	1038
Icosahedral	2693	765

It should be noted here that the geometry of real particles is more complex due to the presence of arbitrarily truncated edges and apexes (Fig. 29a). Thus, the contact areas and static frictions should generally be lower than the maximal values listed in Table 3.

According to the histograms (Fig. 28), low static friction force values prevail in the obtained data set. This finding can be interpreted as a reduction of contact area due to shape evolution towards the spherical after thermal treatment. For values beyond the upper detection limit (where the amplitude dropped to zero), the geometry was assumed to be highly faceted.

The displacement of strongly adhered particles entails the risk of their plastic deformation. As one of the main objectives of our study was to compare the normal and shear modes, we narrowed our measurements to the low-friction region.

Normal oscillation mode is commonly used for the AFM manipulation of nanoparticles. Considering that the friction is significantly higher at ambient conditions than in vacuum, our results correlate well with the previously reported static friction values of 130 nN for 15 nm Au nanoparticles on poly-L-lysine coated mica in air [75]. In many studies, the friction was estimated from the dissipated power [30, 31]; however, the data obtained using such approach cannot be compared with direct frictional force measurements.

In the normal mode, the sensor oscillated perpendicularly to the sample plane, producing a horizontal force component determined by the contact angle. The use of a nonzero contact angle requires sensor calibration in both the horizontal and vertical directions. However, according to our calibration data, the sensor was about ten times less sensitive in the  $Z$  (vertical) direction than in the  $Y$  (horizontal) direction. The ratio between the vertical and horizontal components of the applied force remains unknown, as it is determined by the contact angle, making interpretation of recorded signal in the normal mode complicated.

In the shear mode, the tip oscillated parallel to the sample plane, and the alternating vertical component was almost absent (the small value may be due to imperfect alignment of the sensor relative to the sample). The force calibrations in both  $Y$  and  $Z$  directions showed the same sensitivity within the accuracy of our measurements.

The manipulation curves for both normal and shear oscillation modes were rather similar. However, the values of static friction measured in the normal mode were a few hundred nN lower than those measured in the shear mode. This difference may be due to the contribution of the unaccounted vertical component in the normal mode.

It is worth noting that the normal mode is closely related to AFM tapping mode and hence provides a stable set point. In the shear mode, the tip oscillates above a certain area and it is more difficult to maintain a stable set point.

The influence of the impact velocity on the initial displacement of the particles is another challenging issue. We found that the step regime was more effective for the initial displacement of the particles than the scan regime. This might be related to the abruptness of motion in this regime; the tip strikes the particle with a much higher velocity than in the scan regime. Visual information

concerning the real motion of the tip and the particle is restricted by the scanning speed of the SEM. Manipulation events in the step regime are so fast that we could see only the initial and final positions of the tip and the particle and have no data on the motion in between these points.

#### 4.4. Manipulation of nanowires employed for tribological measurements

For the experiments and tribological measurements zinc oxide NWs were used. ZnO NWs were grown using Au nanoparticles as a catalyst for the vapor transport method [76]. Droplets of water suspension of 60 nm Au nanoparticles (*BBI International*) were deposited on a silicon substrate. Then 1:4 mixture of ZnO and graphite powder was heated to 800–900°C in an open-ended quartz tube over a period of 30 minutes. Synthesized NWs were 10–20  $\mu\text{m}$  long and had diameters in the range of 60 to 200 nm (Fig. 30a).

Morphology of the synthesized NWs is of highly importance within the scope of the present investigation. Size and geometry of the NW strongly influence the interfacial forces as well as elastic properties of the NW and therefore qualitatively determine behavior of NW. Resolution of SEM used in present study was not sufficient to distinguish single facets on the NW surface. Therefore based on the literature data for ZnO NWs the cross-section of NWs used in experiments assumed to be hexagonal [76].

For the measurements of tribological properties of ZnO NWs the substrates were prepared by mechanically transferring the grown NWs from the original wafer to freshly oxidized (50 nm of  $\text{SiO}_2$  layer) silicon wafer (*Semiconductor Wafer, Inc.*) using a piece of clean-room paper (Fig. 30b). Some of the NWs had been broken up during the transferring and the NWs had wide distribution of lengths from few hundred nm to several  $\mu\text{m}$  afterwards.

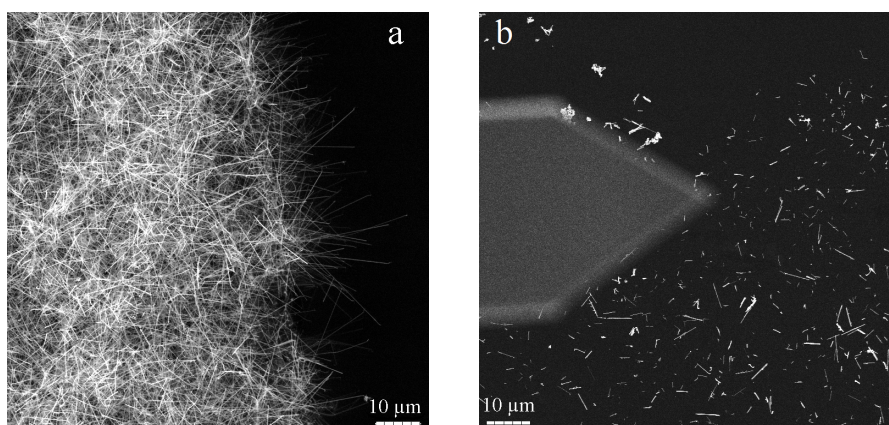


**Figure 30.** Scanning electron microscope images of ZnO nanowires a) grown on silicon substrate and b) mechanically transferred to freshly oxidized silicon wafer.

Experimental measurements included measurements of Young modulus (paragraph 4.4.2), kinetic friction (paragraph 4.4.4), static friction (paragraphs 4.4.6 and 4.4.8), as well as mechanical strength of NWs (paragraph 4.4.6).

#### 4.4.1. Half-suspended nanowire loaded at the end

Let us consider a NW of length  $L$  fixed at one end (“walled”) and loaded by a concentrated force  $F_{\text{load}}$  perpendicular to the initial straight NW line (Fig. 31). This problem is classical and described in textbooks (e.g. [44]) through the following equilibrium equation along the NW axis:

$$EI \frac{d^2 \varphi}{dl^2} + F_{\text{load}} \cos \varphi = 0. \quad (79)$$

Boundary conditions for the walled end and for the zero momentum  $\mathbf{M}$  at the other end dictate:

$$\begin{aligned} \varphi|_{l=0} &= 0 \\ \frac{d\varphi}{dl}|_{l=L} &= 0. \end{aligned} \quad (80a,b)$$

Equation for the NW profile can be then expressed via elliptic integrals or calculated numerically from the tangent angle  $\varphi(l)$ . For the reference, the length of the NW from 0 to the current point as a function of the current tangent angle is:

$$l = \sqrt{\frac{IE}{2F_{\text{load}}}} \int_0^{\varphi} \frac{d\varphi}{\sqrt{\sin \varphi_0 - \sin \varphi}}, \quad (81)$$

where  $\varphi_0 = \varphi|_{l=L}$  is the tangent angle at the free end, which correspondingly can be found from Eq. (81) knowing the overall length  $L$  through the following equation:

$$L = \sqrt{\frac{IE}{2F_{\text{load}}}} \int_0^{\varphi_0} \frac{d\varphi}{\sqrt{\sin \varphi_0 - \sin \varphi}}. \quad (82)$$

The profile of the NW in Cartesian coordinates can be expressed therefore as:

$$x = \sqrt{\frac{2IE}{F_{\text{load}}}} \left( \sqrt{\sin \varphi_0} - \sqrt{\sin \varphi_0 - \sin \varphi} \right), \quad (83a,b)$$

$$y = \sqrt{\frac{IE}{2F_{\text{load}}}} \int_0^\varphi \frac{\sin \varphi d\varphi}{\sqrt{\sin \varphi_0 - \sin \varphi}}.$$

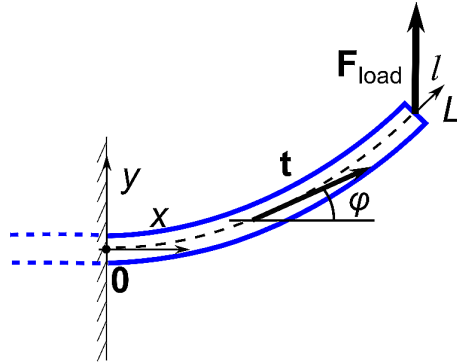


**Figure 31.** Schematics of NW walled at one end and loaded at the other end by concentrated force  $F_{\text{load}}$ .

#### 4.4.2. Young modulus measurements for ZnO nanowires

For measurements of Young modulus  $1 \mu\text{m}$  deep and  $2 \times 2$  or  $1 \times 3 \mu\text{m}$  trenches were cut in Si wafer (Fig. 32b) by focused ion beam (Helios NanoLab, FEI). The measurement algorithm started in translation of the NW over the wafer and positioning it half-suspended on the edge of the trench. In order to measure the Young's modulus, the half-suspended NW was bent by pushing it at the free end with the tip, and the interaction force corresponding to the visually observed bending angle was measured with a QTF force sensor.

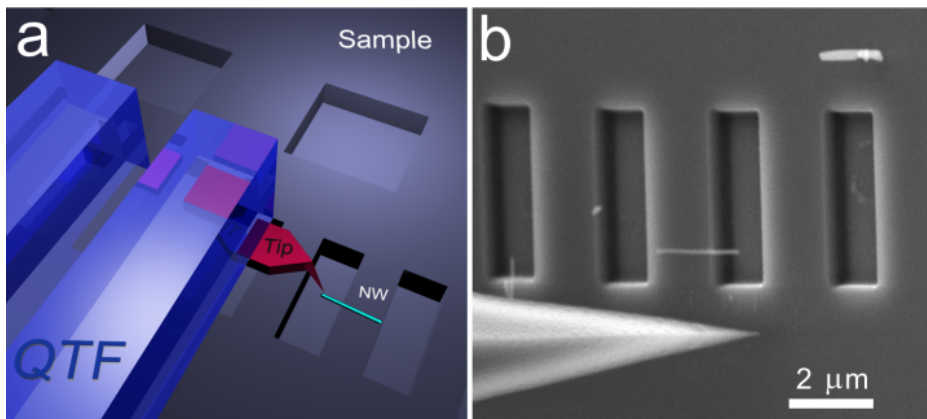


**Figure 32.** Schematics of experiment. (a) QTF with the glued AFM tip contacts a NW suspended over a trench on the silicon sample; Corresponding SEM image of the AFM tip, NW and trenches (b).

NW having appropriate parameters (uniform thickness, sufficient length) and situated in the proximity of the patterned area was chosen and moved by the AFM tip toward nearest trench and positioned over its edge so that one end of the NW was suspended over the trench while another end was fixed to the substrate surface by the adhesion force. The suspended part of the NW was pushed by the AFM tip in direction parallel to the trench wall (Fig. 32). The QTF oscillation amplitude signal (which directly correlates with the applied force) and the grabbed SEM images were recorded simultaneously during the experiment. For the calculation of Young modulus the NW profile from the SEM image was numerically fitted to the curve given by the equation of equilibrium for a bent elastic beam Eq. (79) and the value of Young modulus was extracted.

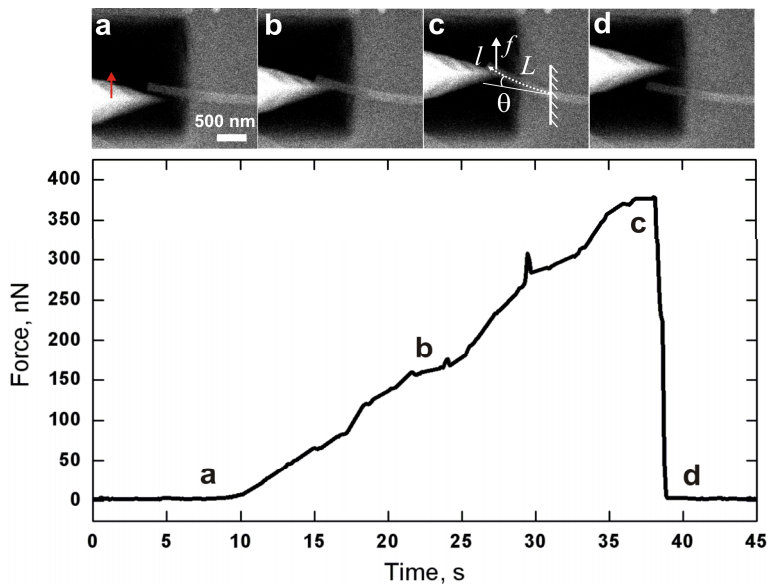


**Figure 33.** SEM images of the suspended NW being pushed by the tip and the corresponding force-time curve. The tip approaches the NW, the arrow indicates the direction of tip movement (a); The NW is slightly bent (b); Maximal bending of NW and the corresponding schematics of the NW loading laid over the SEM image; the natural axis  $l$ , the angle  $\theta$  between the tangent of the bent NW profile projected on an initial NW profile, the length  $L$  of the suspended part of the NW and the applied force  $f$  are shown (c); The NW has come off the tip and the force has dropped to zero (d). The calculated Young's modulus is  $E=58$  GPa.

It should be noted that the region close to the trench (approximately 250–500 nm) is slightly concave due to an imperfect focusing of the ion beam. This should be taken into account when estimating length  $L$  of suspended part of the

NW. Suspended part looks more transparent on SEM image in comparison to the adhered part (Fig. 33a-d).

The typical force curve and the corresponding SEM images are presented in Fig. 33. The averaged value of Young's modulus for five different NWs was found to be  $40.4 \pm 11$  GPa (Table 4). The mean value is in good agreement with other works performed on ZnO NWs. Manoharan *et al.* found 40 GPa for a NW with the diameter of 200–750 nm [77] and Song *et al.* found 29 GPa for a NW with the diameter of 45 nm [78]. Significant variation in magnitudes of Young's modulus from 27 to 58 GPa in the measured set of NWs clearly evidences the importance of gathering the Young's modulus for each NW individually in order to perform calculations of friction based on the balance of elastic and friction forces as described in sections 4.4.4, 4.4.6 and 4.4.8.

In most bending experiments, the adhered part of the NW remained motionless. It means that the applied force was lower than the static friction force between the NW and the substrate. NWs were never broken during the bending experiment, even at large bending angles ( $\theta \approx 60^\circ$ ).

The proposed method opens a route to measure Young's modulus of rather short NWs with lengths of a few microns. In our experiments, the length of the suspended part of NW was about 1  $\mu\text{m}$  in contrast to at least a few tens of  $\mu\text{m}$  in other works dealing with NW bending [77, 79].

**Table 4.** Results of measurements of kinetic friction  $q_{\text{kin}}$  and Young modulus  $E$  of individual ZnO NWs. Interfacial shear stress  $\sigma_{\text{kin}}$  is given assuming the contact on one hexagonal side of the NW.

Nr.	Diameter, nm	Length, nm	$q_{\text{kin}}$ , nN/nm	$\sigma_{\text{kin}}$ , MPa	Young's modulus $E$ , GPa
1	112	3850	0.115	1.8	38
2	125	3280	0.135	1.9	58
3	160	3140	0.2	2.2	27
4	180	4640	0.25	2.4	41
5	230	4615	0.3	2.3	38

#### 4.4.3. Nanowire loaded at the midpoint and balanced by uniformly distributed kinetic friction forces

When a NW is being uniformly dragged at its midpoint and all parts of the NW have the same constant velocity, the equilibrium equations Eq. (27a,b) are still applicable due to Galileo's principle of relativity. In this case, the profile of the deformed NW is determined by the balance of the external driving force, the kinetic friction between the NW and the substrate and the intrinsic elastic forces of the NW. The distributed driving force  $\mathbf{F}_{\text{apl-lat}}$  can be modeled via the delta

function, and the kinetic friction  $\mathbf{q}^{\text{kin}}$  maintains a constant vector opposite to the direction of motion and  $\mathbf{F}_{\text{apl-lat}}$  (see Fig. 34):

$$\mathbf{f} = \mathbf{q}^{\text{kin}} + \mathbf{F}_{\text{apl-lat}} \cdot \delta\left(l - \frac{L}{2}\right). \quad (84)$$

The condition of zero total force yields  $\mathbf{F}_{\text{apl-lat}} = -\mathbf{q}^{\text{kin}}L$ . The differential equation of “kinetic” equilibrium of the NW on the interval  $(0, L)$  directly follows from Eqs. (27,29):

$$IE \frac{d^2\varphi}{dl^2} = -q^{\text{kin}} \left[ l - LH\left(l - \frac{L}{2}\right) \right] \cos\varphi, \quad (85)$$

where  $H(x)$  is the Heaviside step function. The Eq. (85) can be solved numerically in order to obtain the NW profile. It is easy to see that the solution of Eq. (85) together with the initial condition  $\varphi'(0) = 0$  fully complies with the free boundary conditions  $\mathbf{F}|_{l=0} = \mathbf{F}|_{l=L} = 0$  and  $\mathbf{M}|_{l=0} = \mathbf{M}|_{l=L} = 0$ .

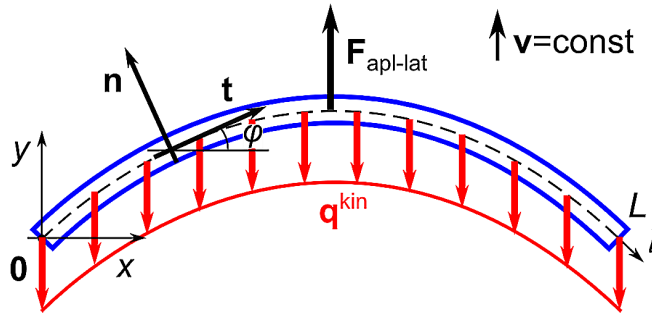


**Figure 34.** Schematics of a nanowire of length  $L$  being pushed at the midpoint by concentrated force  $\mathbf{F}_{\text{apl-lat}}$  and affected by distributed kinetic friction force  $\mathbf{q}^{\text{kin}}$ . Fixed coordinates system  $Oxyz$  and local coordinate basis  $(\mathbf{t}, \mathbf{n})$  along the nanowire axis  $l$ . Angle between the tangent vector  $\mathbf{t}$  and axis  $Ox$  is denoted as  $\varphi$ .

#### 4.4.4. Measurement of kinetic friction of ZnO nanowires on a flat surface

For the kinetic friction measurements NW was translated by pushing it at its midpoint with AFM tip. The shape of the NW elastically deformed during the translation was used to determine the distributed kinetic friction force. To increase the loading during the NW translation and to ensure that the tip would

not slide over the NW, the force sensor was lowered another 1–2  $\mu\text{m}$  after the tip came into contact with the substrate surface. The oscillation amplitude dropped to zero due to the high repulsive force, and no force measurement was performed during the NW translation.

After being pushed a few microns the NW bends into an arc due to the distributed kinetic friction force acting along the NW's length (Fig. 35). The characteristic profile of the bent NW remains constant during the translation due to the fact that the total kinetic friction force acting on the NW is balanced with the external force applied by the tip. The determination of the distributed kinetic friction for shorter NWs was problematic due to the large radius of the curvature during the translation. The minimal length suitable for the determination of kinetic friction depends on the NW's diameter. For NWs used in our experiments minimal length was found to be about 3  $\mu\text{m}$ .

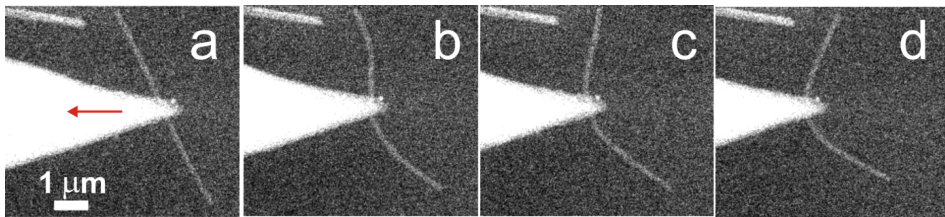


**Figure 35.** Scanning electron microscope images of the NW shape profile during the NW dragging. The AFM tip contacts the intact NW, the arrow indicates the direction of tip movement (a); Partially displaced NW (b); Completely displaced NW (c); Final characteristic shape (d).

For estimation of the distributed kinetic friction force the Timoshenko beam theory was applied as described in the paragraph 1.6. NW length  $L$ , diameter  $D$  and profile during manipulation were obtained from the SEM image. Actual values of Young moduli measured individually for each NW as described in the paragraph 4.4.2 were used for the calculation.

Measurements were performed on five NWs with different diameters. Results of the calculations are presented in Table 4. The average value of the interfacial shear stress is  $\sigma_{\text{kin}}=2.1\pm 0.26$  MPa. These results are in a good agreement with Manoharan *et al.* who obtained 1 MPa for the interfacial shear stress for ZnO 30–40  $\mu\text{m}$  long NWs with 200 nm diameters parallel to the NW axis dragging [80].

Large variation in sliding friction and shear stress values are common for nanotribological experiments, e.g. of an order of magnitude for InAs NWs [51]. That is probably also due to the usage of the bulk Young's modulus of InAs in the friction calculations. Thus, the use of individual values of Young's modulus for each NW is important to make friction force and shear stress determination more reliable.

#### 4.4.5. Nanowire loaded at the end and balanced by combined distributed kinetic and static friction forces

Let us consider a specific situation, when initially straight NW has been loaded at some point and a part of the NW was fixed to the substrate by static friction (see Fig. 36). The mobile part of the NW undergoes kinetic friction and the concentrated load force. The distributed force  $\mathbf{f}$  consists of the external tip force  $\mathbf{F}_{\text{apl-lat}}$  applied at the point  $L_{\text{tip}}$ , and the kinetic friction force  $\mathbf{q}^{\text{kin}}$  per unit length distributed uniformly along the moving part of the NW:

$$\mathbf{f} = \mathbf{q}^{\text{kin}} + \mathbf{F}_{\text{apl-lat}} \cdot \delta(l - L_{\text{tip}}), \quad (86)$$

where  $\delta(x)$  is Dirac's delta-function.

Zero elastic force and momentum at the NW's free end dictate the boundary conditions [44]:

$$\begin{aligned} \mathbf{F} \Big|_{l=L_{\text{kin}}} &= 0 \\ \mathbf{M} \Big|_{l=L_{\text{kin}}} &= 0. \end{aligned} \quad (87\text{a,b})$$

Elastic force  $\mathbf{F}$  according to Eq. (27a) yields together with Eq. (86):

$$\mathbf{F} = -\mathbf{q}^{\text{kin}} \cdot (l - L_{\text{kin}}) - \mathbf{F}_{\text{apl-lat}} \cdot (H(l - L_{\text{tip}}) - 1), \quad (88)$$

where  $H(x)$  is Heaviside step function.

Finally the equation for  $\varphi(l)$  describing the profile of NW with boundary conditions:

$$\begin{aligned} EI \frac{d^2 \varphi}{dl^2} &= [q^{\text{kin}}(l - L_{\text{kin}}) - F_{\text{apl-lat}} \cdot (H(l - L_{\text{tip}}) - 1)] \cdot \cos(\varphi + \theta) \\ \varphi \Big|_{l=0} &= 0 \\ \frac{d\varphi}{dl} \Big|_{l=L_{\text{kin}}} &= 0, \end{aligned} \quad (89\text{a,b,c})$$

where Eq. (89b) defines orientation of the NW with respect to the coordinate system, Eq. (89c) follows directly from Eq. (87b) and Eq. (87a) is automatically satisfied. Eq. (89) can be simplified in particular case  $L_{\text{tip}}=L_{\text{kin}}$  and yields:

$$EI \frac{d^2 \varphi}{dl^2} = [q^{\text{kin}}(l - L_{\text{kin}}) - F_{\text{apl-lat}}] \cdot \cos(\varphi + \theta). \quad (90)$$

Motionless (“static”) part of the NW is assumed to be a rigid rod of length  $L_{st}$  with 2 degrees of freedom: axis  $Oy$  and rotation angle in the plane  $Oxy$ . Values of elastic force  $F_y|_{l=0}$  and momentum  $M|_{l=0}$  at the start point of the motionless region follow from the solution of Eqs. (89a,b,c) for continuity reasons. We assume that the interfacial stress between the NW and substrate and consequently the static friction force is distributed linearly along the rotated static part of the NW:  $q_y^{st}(l') = a \cdot l' + b$ , where  $a$  and  $b$  are unknown constants. For the equilibrium of the NW, conditions for total force and momentum yield system of two equations:

$$F_y|_{l=0} = \int_0^{L_{st}} q_y^{st}(l') dl' \quad (91a,b)$$

$$M|_{l=0} = \int_0^{L_{st}} q_y^{st}(l') l' dl' ,$$

which easily determine  $a$  and  $b$ . This allows to find such parameters as maximal static friction  $q_{max}^{st} = |b|$  and averaged static friction  $q_{avg}^{st} = \frac{1}{L_{st}} \int_0^{L_{st}} |q_y^{st}(l')| dl' .$

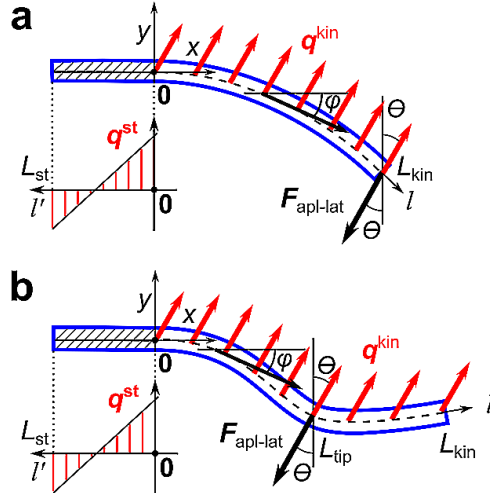


**Figure 36.** Schematics of a nanowire loaded by concentrated force  $F_{apl-lat}$  and affected by distributed kinetic friction force  $q^{kin}$  of the interval  $(0, L_{kin})$  along  $l$  axis. Left end is fixed by strong static friction force  $q^{st}$  on the interval  $(0, L_{st})$  along  $l'$  axis. Angle between the tangent vector and axis  $Ox$  is denoted as  $\varphi$  and  $F_{apl-lat}$  is directed by angle  $\theta$  to  $Oy$  axis. The external force  $F_{apl-lat}$  is applied at the very end of the NW (a), the external force  $F_{apl-lat}$  is applied at a distance from the end of the NW (b).

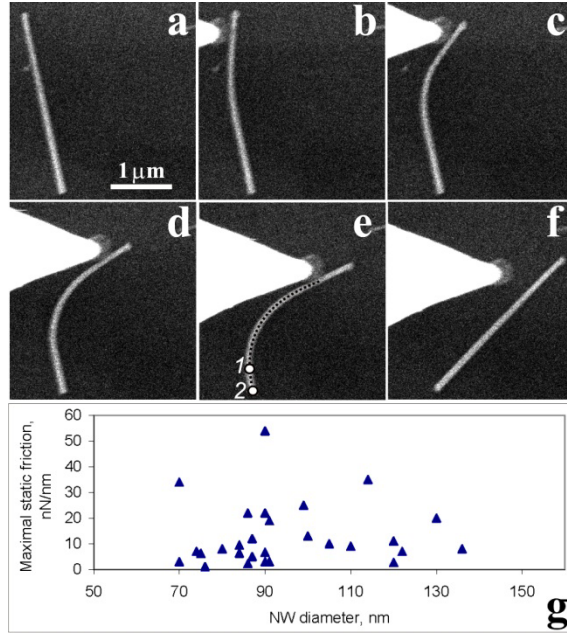
#### 4.4.6. Combined measurements of the kinetic and static friction forces of a ZnO nanowire on a flat surface

Another approach in measurements of the NW static friction consists in bending of the NW lying on flat substrate by pushing it at one end with an AFM tip while some part of the NW at opposite end is adhered to the substrate and stays motionless as long as the applied external force does not exceed the total static friction force between adhered part and substrate. When the elastic stress generated inside the bent NW overcomes the total static friction force, the whole NW is displaced. The NW bending profile just before the complete displacement (“most bent state”) of the NW may be used then to find the static friction force. It is done by fitting the experimentally found NW bending profile in “most bent state” to the theoretical profile of an elastic beam lying on a flat substrate and pushed from one end by a point force in the substrate plane, while the second end is fixed by static friction as described in the paragraph 4.4.5. From the elastic deformation of the NW the generated elastic force and momentum are calculated. It enables to find counteracting friction forces in the adhered part.

Depending on the point of the force application on the NW two loading schemes are possible. The first loading scheme is when an external force is applied at the very end of the NW. In this case the bending profile of the NW is rather simply determined and described (Fig. 36a). If an external force is applied at longer distance from the end of the NW, the profile may be more complicated and the second loading scheme is realized (Fig. 36b).

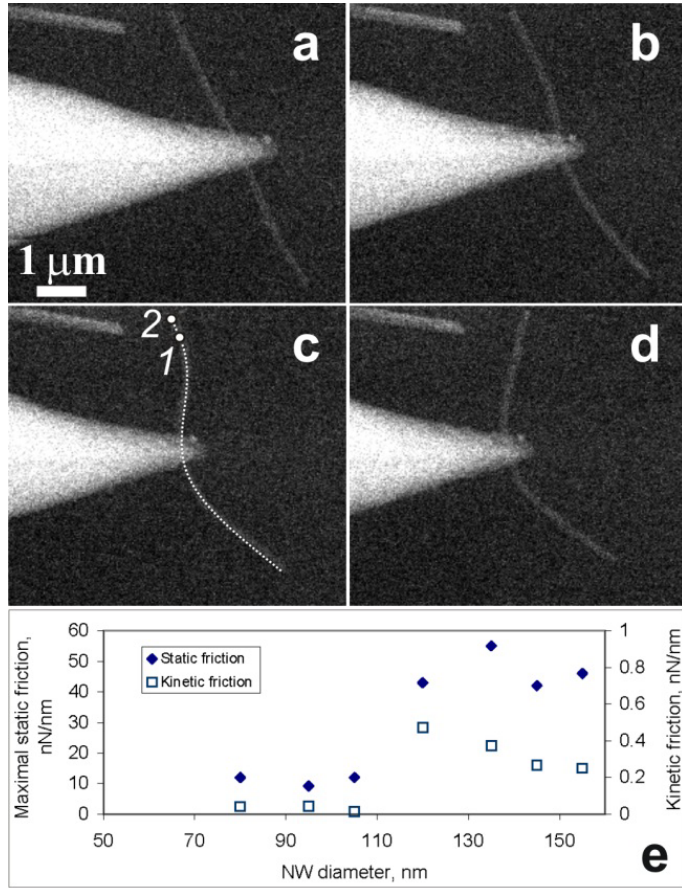
It should be noted that the method is applicable only for NWs having aspect ratio in the appropriate range (usually between 10 and 100). If NW is sufficiently short (one micron or less for 100 nm cross-section), it slides or rotates as a whole object; if NW is long enough, the internal elastic force produced during NW bending is not strong enough to overcome the static friction force, and the NW cannot be displaced even after significant bending. To produce a loading force high enough to initiate the displacement of NWs, the AFM chip with a cantilever was lowered 5–20  $\mu\text{m}$  after the tip came into contact with the substrate surface.

**First loading scheme.** Fig. 37 represents a typical manipulation experiment according to the first loading scheme. The NW was bent by pushing it from one end by an AFM tip until the internal elastic stress generated due to deformation led to release of adhered part of NW and straightening of the whole NW (Fig. 37a-f). Considering the length, the cross section of the NW, and the applied force  $F_{\text{apl-lat}}$  as fitting parameters, the NW “most bent state” profile was calculated according to Eq. (90) and laid over the SEM image (Fig. 37e). The values of Young’s modulus  $E=57$  GPa and the interfacial shear stress associated with the kinetic friction force  $\sigma^{\text{kin}}=2.1$  MPa were taken from our previous works described in section 4.4. The statistics of the maximal static friction measurements for a set of 32 NWs is presented in Fig. 37g.



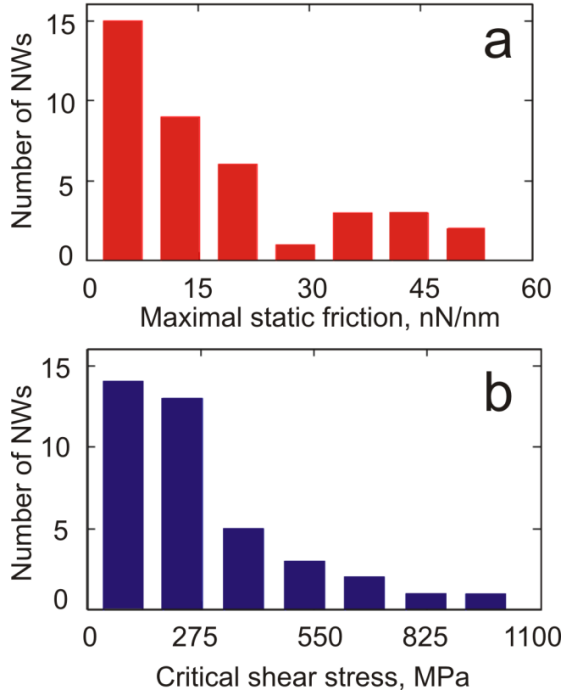
**Figure 37.** Manipulation experiment of ZnO nanowires according to the first loading scheme (see text). Series of SEM images of the nanowire bent by AFM tip from one end while other end is adhered to the substrate by static force (a-f). Skeletonized profile lying over the real nanowire image (e). Completely displaced nanowire (f). Distribution of the maximal static friction force versus NW diameter (g).

**Second loading scheme.** When an external force is applied at a longer distance from the end of the NW, the free end of the moving part is bent in opposite direction (Fig. 38). The degree of bending of the moving part is determined by the magnitude of the kinetic friction force. The “most bent” profile of NW in this case contains information about both the static and the kinetic friction. It enables to introduce the kinetic friction  $q^{\text{kin}}$  as an independent fitting parameter in addition to the applied force  $F_{\text{apl-lat}}$ , in contrast to the first scheme where we used the average value of  $q^{\text{kin}}$  taken from previous experiments. The fit for the NW bending profile was calculated according to Eq. (89) and compared to the experimental profile of the NW (Fig. 38c). The second loading scheme was applied to 7 NWs (Fig. 38e). The median value of kinetic friction was  $q^{\text{kin}} = 0.25$  nN/nm ( $\sigma^{\text{kin}} = 2.8$  MPa), which is close to our previously obtained results in the paragraph 4.4.4 [81]. These measurements confirm that for NWs, the static friction can be significantly higher than the kinetic friction.



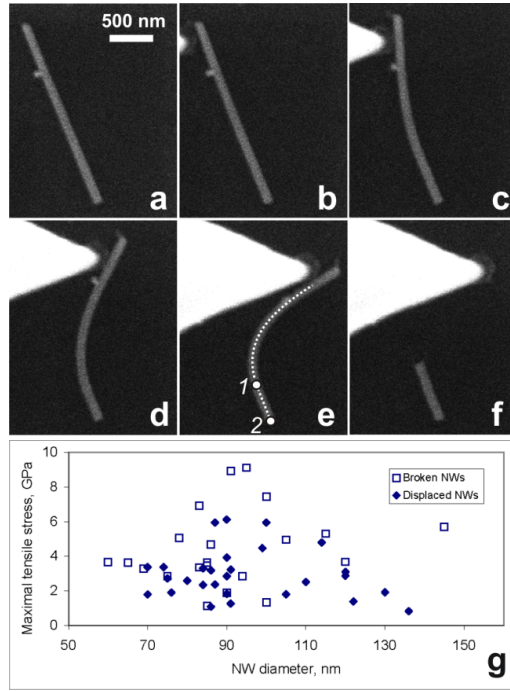
**Figure 38.** Manipulation experiment of ZnO nanowires according to the second loading scheme (see text). Intact NW (a). Part of the NW is displaced (b). “Most bent” profile of the NW before the complete displacement; the calculated profile (dashed white line) that is laid over the SEM image; white points (1, 2) indicate the static portion of the NW (c). The whole NW is displaced (d). The NW diameter is  $D=155$  nm, the calculated maximal static friction is  $q_{\max}^{\text{st}} = 46$  nN/nm ( $\sigma_{\max}^{\text{st}} = 514$  MPa), and the kinetic friction is  $q^{\text{kin}} = 0.25$  nN/nm ( $\sigma^{\text{kin}} = 2.8$  MPa). Measurement statistics of the static and kinetic friction for a set of 7 NWs (e).

Figure 38 presents the statistics of maximal static friction and critical interfacial shear stress for all 39 measured NWs. The median values of the maximum static friction and average static friction were found to be  $q_{\max}^{\text{st}} = 11$  nN/nm and  $q_{\text{avg}}^{\text{st}} = 5$  nN/nm, respectively. The corresponding values of critical interfacial static shear stress and average static shear stress were  $\sigma_{\max}^{\text{st}} = 195$  MPa and  $\sigma_{\text{avg}}^{\text{st}} = 67$  MPa.



**Figure 39.** Histograms of maximum static friction  $q_{\max}^{\text{st}}$  (a) and corresponding critical interfacial shear stress  $\sigma_{\max}^{\text{st}}$  (b) summary of the measurements according to both loading schemes. The median value of static friction is  $q_{\max}^{\text{st}} \sim 11$  nN/nm, and the critical interfacial shear stress is  $\sigma_{\max}^{\text{st}} \sim 195$  MPa.

**NW strength measurement.** Loading scheme described in section 4.4.5 can be used for calculation of NW fractural strength when the static friction in adhered part is higher than the force needed to break the NW by bending (Fig. 40). In general, the NWs that broke experienced smaller interfacial shear stress (a longer motionless region  $L_{\text{st}}$ ) but higher tensile stress compared to the displaced the NWs. The tensile stress is maximal at the boundary dividing the motionless and displaced regions of the NW (Fig. 40e). However, the NWs did not necessarily break in the maximal tensile strain region but in any region probably with a structural defect. The statistics of maximal tensile stress values for both broken and displaced NWs are presented in Fig. 40g. The median value of tensile stress in successfully displaced NWs was  $\sigma_{\text{displ}}^{\text{tens}} = 2.6$  GPa (for a set of 32 NWs), while in broken NWs,  $\sigma_{\text{fract}}^{\text{tens}} = 3.3$  GPa (for a set of 21 NWs). These values are in good agreement with failure tests performed by Hoffmann *et al.* on ZnO nanowires, where failure occurred with stress in the range from 2–9 GPa [82].



**Figure 40.** Fracture of a NW during manipulation. Intact NW (a). Gradual bending of NW (b-d). The “most bent state” profile before the fracture of the NW and the calculated bending profile (dashed white line) laid over the SEM image; white points (1, 2) indicate the static part of the NW (e). The NW is broken (f). The NW diameter is  $D = 115$  nm; its fracture tensile stress is  $\sigma_{\text{frac}}^{\text{tens}} = 5.1$  GPa. The statistics of the maximum tensile stress for both broken NWs (21 NWs) and displaced NWs (32 NWs) (g).

#### 4.4.7. Nanowire self-balanced by distributed static friction forces on a flat surface

In the case when the NW had been preliminarily bent by an actuator, it can be sustained in bent state by static friction forces from the substrate after the removal of the external load. The equations of equilibrium for a purely bent NW affected by distributed static friction force  $\mathbf{f}(l) = \mathbf{q}^{\text{st}}(l)$  give (see Fig. 8 and, e.g., [44]):

$$\begin{aligned} \frac{dF_t}{dl} - \kappa F_n &= -q_t^{\text{st}} \\ \frac{dF_n}{dl} + \kappa F_t &= -q_n^{\text{st}} \end{aligned} \quad (92a,b,c)$$

$$EI \frac{d\kappa}{dl} = -F_n,$$

where  $F_t$  and  $F_n$  are the projections of elastic force  $\mathbf{F}$ ,  $q_t^{\text{st}}$  and  $q_n^{\text{st}}$  are the projections of  $\mathbf{q}^{\text{st}}$  to the local coordinates  $(\mathbf{t}, \mathbf{n})$ .

Zero elastic force and momentum at the free ends of the NW dictate the boundary conditions [44]:

$$\begin{aligned} \mathbf{F}|_{l=0} &= \mathbf{F}|_{l=L} = 0 \\ \mathbf{M}|_{l=0} &= \mathbf{M}|_{l=L} = 0. \end{aligned} \tag{93a,b}$$

The complete set of boundary conditions Eq. (93a,b) applied to the system Eq. (92a,b,c) yields:

$$\begin{aligned} \kappa|_{l=0} &= \kappa|_{l=L} = 0 \\ \frac{d\kappa}{dl}\bigg|_{l=0} &= \frac{d\kappa}{dl}\bigg|_{l=L} = 0. \end{aligned} \tag{94a,b}$$

We will neglect the tangential component of the friction  $q_t^{\text{st}} = 0$ , thus making the system of Eq. (92a,b,c) complete and yielding:

$$\begin{aligned} F_t &= -EI \int_0^l \kappa \frac{d\kappa}{dl} dl = -EI \frac{\kappa^2}{2} \\ q_n^{\text{st}} &= EI \left( \frac{d^2\kappa}{dl^2} + \frac{\kappa^3}{2} \right), \end{aligned} \tag{95a,b}$$

which solves the system together with the initial condition  $F_t|_{l=0} = 0$ . The absence of a tangential friction component does not lead to the vanishing of  $F_t$  which is then fully “driven” by the normal component  $F_n$  and necessary for exact NW equilibrium.

It is important to note that the assumption  $q_t^{\text{st}} = 0$  was dictated by an intuitive consideration that the direction of  $\mathbf{q}^{\text{st}}$  should be close to the direction at which the NW tends to unbend. This “unbending” direction correspondingly is close to normal to the NW’s line. Formally it means that the integral contribution of  $q_t^{\text{st}}$  along the length of the NW is much smaller than that of  $q_n^{\text{st}}$ .

#### 4.4.8. Measurements of a self-balanced ZnO nanowire static friction on a flat surface

Once a NW is deposited on a substrate and elastically deformed in plane, the NW may preserve its bending profile or relax to form another non-straight profile. This requires the NW to be flexible enough (high aspect ratio) and static friction to be sufficiently high. In this case the role of “external force” is employed by the elastic force in each point along the NW which in turn controlled by static friction force in other points of the NWs. This kind of self-balanced system, theoretically described in the paragraph 4.4.7, can be used for estimation of static friction for experimentally observed bent NWs self-balanced by distributed static friction forces on a flat surface.

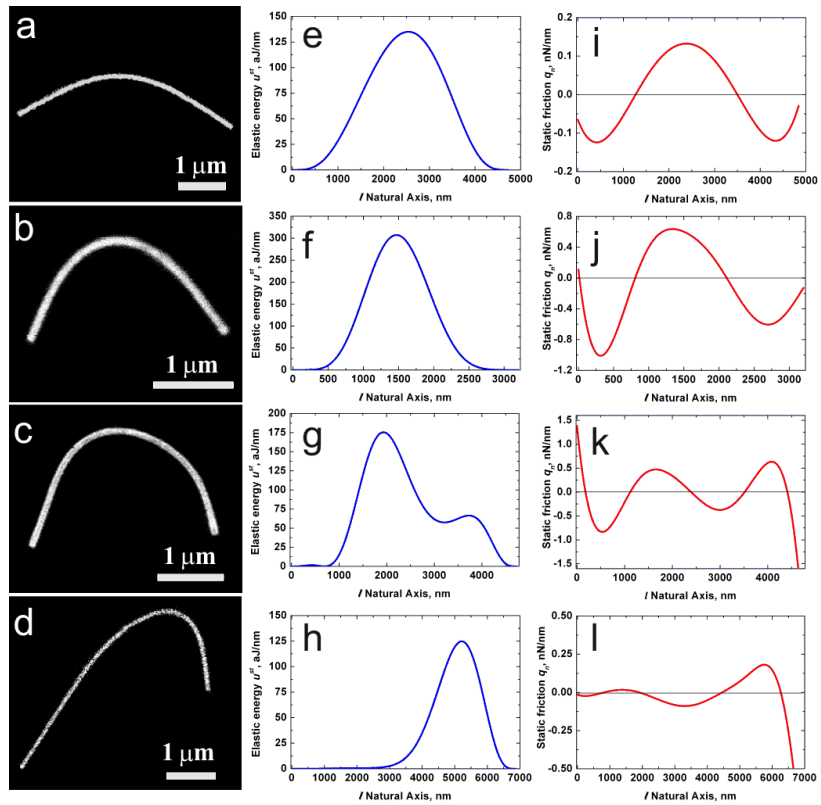


**Figure 41.** Measurements of elastic energy density and static friction distribution as functions along the NW for differently shaped nanowires (in rows). Parameters used: Young modulus  $E=57$  GPa; diameter  $D=115$  nm (a,e,i);  $D=111$  nm (b,f,j);  $D=112$  nm (c,g,k);  $D=103$  nm (d,h,l).

Consider a SEM or AFM image of a ZnO NW bent upon a substrate as a data source for static friction force analysis. We have developed an original method of skeletonization suitable for finding elastic and friction forces with use of Eq. (95). The method consist of several steps: 1) Filtration of the source image and identification the backbone of the nanowire in Cartesian coordinates in the form of separate points; 2) differential analysis of the backbone points to find the tangential angle curve; and 3) interpolation of the tangential angle curve with polynomial function confined by the boundary conditions Eq. (94). As a result we obtain a smooth polynomial function  $\varphi(l)$ , which can be then utilized for the further  $q_n^{\text{st}}(l)$  calculations according to Eq. (95b). A special polynomial function was chosen as a possible analytic form for Eq. (95). Let us now examine an application of this method in detail.

The source image snapshotted from a microscope usually contains some foreign objects (other nanowires, nanoparticles, etc.). Everything except the NWs under investigation should be filtered out to avoid artifacts during the skeletonization. After filtration, the image is ready for the extraction of the backbone.

For locating the backbone we used a polar-scanning method. We chose an origin point and observed the intersection of the polar beam with the NW. The intersection histogram commonly has an obvious peak which we assume to belong to the backbone curve. This method is best suited for curves bent in a circular manner, so that we can choose an origin point close to the circle's center. However, any other method of backbone extraction can be used.

After the microscope image of the NW is skeletonized, a set of  $n$  discrete points  $(x_i, y_i)$  is obtained, representing the backbone. Differential analysis of the backbone is then needed to convert the Cartesian coordinates  $(x_i, y_i)$  to natural coordinates  $(l_i, \varphi_i)$ , which are more suitable for the subsequent calculations. The discrete mesh for future  $\varphi(l)$  interpolation is produced with the following expressions:

$$\varphi_i = \tan^{-1} \left( \frac{y_{i+1} - y_i}{x_{i+1} - x_i} \right), \quad 1 \leq i < n - 1 \quad (96a,b)$$

$$l_i = l_{i-1} + \sqrt{(x_i - x_{i-1})^2 + (y_i - y_{i-1})^2}, \quad 2 \leq i < n,$$

where  $l_1 = 0$ .

Correct choice of the interpolation function is important, due to errors, which may arise during the identification and differentiation of the backbone curve. Regular polynomial interpolation would likely break the boundary conditions Eq. (94). The interpolation of  $\varphi(l)$  can be performed through the curvature  $\kappa(l)$  with the linear combination of the selected polynomial functions as follows:

$$\frac{d\varphi}{dl} = \kappa(l) = \sum_{i=0}^N A_i l^{i+2} (L-l)^2, \quad (97)$$

where  $A_i$  are coefficients to be determined by the numerical interpolation. It is apparent that  $\varphi(l)$ , defined according to Eq. (97), complies with the boundary conditions Eq. (94).

It should be noted that, the more asymmetric or wavy the nanowire curve looks, the higher the degree  $N$  that must be used. Higher  $N$  leads to increased precision in fitting the curves, but it also may introduce artifacts generated from the scatter of experimental points. Therefore, as low  $N$  as possible should be used, on condition of sufficient correspondence between the fitted and the original curves.

The friction profile can be now calculated with the Eq. (95b), using the constrains for  $\kappa(l)$  from Eq. (94). The expression for  $q_n^{\text{st}}(l)$  contains the 2nd derivative of the approximated  $\kappa(l)$  and therefore might contain significant error. As a consequence, the friction profile  $q_n^{\text{st}}(l)$  can vary significantly with  $N$ . As stated above, the usage of high  $N$  may introduce unnecessary features into the curve and therefore should be avoided.

Let us now take, for instance, an experimental nanowire of ZnO resting on a silicon wafer substrate. In the Fig. 41, an SEM images of bent ZnO nanowires are presented. To prepare the NW in this bent state, it was pushed near its center perpendicular to the NW axis by an AFM tip inside the SEM [81]. Over several microns of travel, the initially straight profile of the NW transformed into the characteristic arc shape. The static friction force model can be applied after the removal of the force applied by the AFM tip.

Prior to the calculation of  $q_n^{\text{st}}(l)$  a number of steps were performed as follows. The image was filtered manually. The backbone was extracted in the form of an array of Cartesian coordinates, and Eq. (96) was used to obtain the mesh of  $(l_i, \varphi_i)$  for further interpolation according to Eq. (97). Then the distributed friction force  $q_n^{\text{st}}(l)$  was calculated using Eq. (95b) taking into account  $I = 5\sqrt{3}D^4/256$  for the hexagonal cross section of the NW [76], where  $D$  is the diameter of the NW's. Polynomial functions of a degree of up to 7 were used, which corresponds to  $N = 3$ .

As was mentioned above, the shape and extreme values of  $q_n^{\text{st}}$  are sensitive to any errors in the interpolated NW profile and to the polynomial degree. Therefore, we must find reliable quantities able to characterize the NW-substrate system.

The friction profile  $q_n^{\text{st}}(l)$  contains several ranges of length with different signs. We suggest using the following procedure to estimate the average friction forces acting on the different parts of the NW. When we integrate

$Q_i^{\text{st}} = \left| \int_{l_i}^{l_{i+1}} q_n^{\text{st}}(l) dl \right|$ , the obtained quantity has the meaning of an effective force

acting on the corresponding range. At least three regions,  $Q_1$ ,  $Q_2$  and  $Q_3$ , are necessary to stabilize the NW profile in its bent state. Our calculations have shown that the  $Q_1$  calculated using different  $N$  do not significantly change, however a positive correlation of  $Q_i$  with  $N$  is noticeable (see [83]). This behavior can be attributed to the fact that a curve of higher  $N$  is wavier and therefore implies higher elastic distortion of the NW, which leads to higher friction. For the next step, a friction force averaged along the NW length  $\bar{q}_n^{\text{st}} = \sum_i |Q_i^{\text{st}}| / L$  is introduced. This along-NW-length-averaged friction force

$\bar{q}_n^{\text{st}}$  still remains nearly the same with different  $N$ , and it may be utilized to characterize the magnitude of the NW-substrate friction interaction.

As it was stated above, the kinetic friction force is balanced with the force applied by the tip during the dragging of the NW over the substrate surface. We did not find any visual changes in the NW profile during the dragging and after the removal of the tip, hence elastic energy of deformed NW for static case should be preserved approximately the same with kinetic case. The static friction force should redistribute itself to maintain force balance with the elastic force, and value of averaged static friction should be comparable with one of kinetic friction. It should be noted here that the method for determination of the kinetic friction utilizes a more simple and faultless model than the static friction model (more details in [81]). In other words, agreement between values of kinetic and averaged static friction will verify correctness or fault of static friction calculation method. The averaged static friction force  $\bar{q}_n^{\text{st}}$  (1.7–2.34 nN/nm) has a value close to that of the kinetic friction  $q^{\text{kin}}$  (1.8 nN/nm). This confirms appropriateness of our static friction calculation method.

An additional characteristic of the NW-substrate interaction is the elastic energy stored in the bent nanowire. The stronger the NW-substrate friction interaction, the higher the strain energy can be conserved in the elastically bent NW. The elastic energy per unit length  $u^{\text{st}}$  and total elastic energy  $U^{\text{st}}$  of bent nanowire can be calculated, respectively, as [44]:

$$u^{\text{st}} = \frac{EI}{2} \kappa^2$$

$$U^{\text{st}} = \int_0^L \frac{EI}{2} \kappa^2 dl. \quad (98\text{a,b})$$

The profile of the distributed elastic energy  $u^{\text{st}}$  is shown in Fig. 42. The distributed elastic energy is proportional to the square of the NW curvature  $\kappa(l)$

and contains much smaller error compared to the friction force. Profiling of the distributed strain energy along the NW length and calculation of the total elastic energy may be important in piezotronics for engineering piezoresistive and piezoelectric nanowire-based devices [84].

It is important to note that, while  $u^{\text{st}}$  has only one extremum near the NW center, the distributed friction  $q_n^{\text{st}}$  experiences 3 extrema of different signs. This evidences a non-local character of the NW-substrate friction. Moreover, the model enables certain cases when  $|q_n^{\text{st}}|$  has absolute maxima near the NW ends, rather than in the middle where the absolute maximum strain is located. Consequently, it is impossible to judge where the maximum friction is applied without detailed analysis in the framework of the presented distributed NW friction model.

We have demonstrated that our method produces reasonable values of the averaged friction force  $\bar{q}_n^{\text{st}}$ , and gives estimations of the distributed and total elastic energies  $U^{\text{st}}$ . Thus, the method may provide important and useful information on NW-substrate force interactions.

## 4.5. Summary

In the chapter 4 several theoretical and experimental methods for investigation of tribological properties of nanoparticles and nanowires were described.

Paragraph 4.1 demonstrated the model and some results of numerical simulation of INP manipulation. A computer program was developed to implement the simulations and visually present the results. The INP is modeled as a rigid body governed by Newton's laws of motion. Two main cases were considered: (a) the INP is rested on an atomically flat substrate and affected by a point force, and (b) the INP is clutched between 2 atomically flat surface while the upper surface is laterally dragged by a spring with a constant velocity. The surface and the INP consisted of atoms in mass point model. The interaction between the surface and the INP was calculated peer-to-peer between the atoms. The interaction forces came from 2 sources: conservative potential and dumping interaction. The point force can drag the INP over the surface in different manners depending on the position and magnitude of that force. In general, the motion of the INP is a combination of translational and rotational motion. However, the direction and velocity of the rotation depends on the position of the applied force. The results for 3 special cases (the lateral force at the top, in the middle and at the bottom of the INP) were qualitatively described.

Paragraph 4.2 describes the nanomanipulation experimental setup and the QTF force sensor used for investigation of tribological properties of NPs and NWs. The setup consists of an AFM cantilever glued on a QTF mounted onto a high-precision 3D nanomanipulator. The cantilever can be glued in 2 ways,

enabling either normal or shear type of oscillations. This system is located inside a SEM and enables real-time visual guidance of the manipulation experiment. The QTF is served by a lock-in amplifier in amplitude modulation mode. A special control and measurement system is developed in order to manage the 3D manipulator and record the signal from the QTF. The calibration procedure is used to match the signal from the QTF and real force applied to the manipulated object.

In the section 4.3 the results of the tribological measurements on gold nanoparticles are presented. The nanoparticles of approximately 150 nm in diameters on an oxidized Si substrate were used. The forces needed to overcome static friction and move individual nanoparticles were measured in normal and shear oscillation modes. The static friction was found to range from 40 to 450 nN for the normal mode and from 50 to 750 nN for the shear mode. The kinetic friction tends to be close to the detection limit and in most cases does not exceed several nN. Thermal treatment of Au particles for 1 hour at 725 K resulted in a rounding of the particles and a corresponding decrease in the static friction.

Section 4.4 contains several experimental methods of measurements of NW-substrate friction and elastic properties (Young modulus) of NWs. For each of the method a detailed description of the corresponding theoretical model is given. The experiments are performed for ZnO NWs on oxidized Si wafer using the real-time nanomanipulation experimental setup with QTF force sensor for measurement of Young modulus and without the force sensor in other cases.

The measurement of Young modulus is conducted when the NW is half-suspended on a trench in the substrate and bent by the tip. The applied force by tip is registered and then used to correlate the force with visually observable deflection of the NW and to find the Young modulus. The magnitude of Young modulus ranged from 27 to 58 GPa.

In order to measure the kinetic friction of NW on a flat surface, the NW was loaded by a tip at the midpoint and dragged with a constant velocity along some direction. In this case, the NW shape is determined by the interplay of elastic forces inside the NW, the kinetic friction from the substrate and the external concentrated force from the tip. The NW profile observed in SEM is used to calculate the kinetic friction between the NW and the substrate by fitting to a theoretical model. The obtained magnitudes of the interfacial kinetic shear stress are within the range 1.8–2.3 MPa.

The combined measurements of the kinetic and static friction is used, when the NW is pushed by a tip in some point and the NW is partially moving while the rest part is still. That corresponds to the situation when the NW exerts both kinetic and static kinds of friction at the same time. The shape of the NW is then determined by the interplay of internal elastic forces, all friction forces and external forces. This experiment may end up in 2 basic scenarios upon the increase of the applied force: (a) the static friction is overcome and the whole NW is displaced, (b) the NW is broken due to high tensile stress. The first scenario enables to estimate the ultimate NW-substrate static friction. The second one allows measuring the tensile strength of the NW. Moreover, when

the tip pushes at some distance from the end of the NW, measurement of the kinetic friction is also possible. Values of the maximal interfacial static shear stress, averaged static shear stress and kinetic shear stress obtained are  $\sigma_{\max}^{\text{st}} \sim 195$  MPa,  $\sigma_{\text{avg}}^{\text{st}} \sim 65$  MPa and  $\sigma^{\text{kin}} \sim 2.8$  MPa respectively. Median value of the tensile strength for broken NWs is  $\sigma_{\text{break}}^{\text{tens}} \sim 3.3$  GPa.

The measurement of the distributed static friction force of a NW is performed also for the case when the NW is bent and self-balanced by static friction from the flat substrate. In this case the static friction significantly varies along the NW and the distribution of the static friction force can be obtained by considering the visible NW bending profile. The NW profile is determined by the friction force in each point of the NW and elastic force in the NW. It is important to note that the NW's elastic force is cumulative and therefore the bending curvature of the NW in each point is not locally determined by friction. The elaborated model includes taking this cumulative effect into account as well as the effect of free NW ends. The several visual NW profiles of ZnO NW on an oxidized Si wafer are considered and the calculation of the static friction distribution is demonstrated. In addition, the elastic strain energy density is presented as a function along the NW.

## MAIN RESULTS AND CONCLUSION

From the point of view of modern physics, size of the physical system under the investigation is crucially important and in many cases essentially determines the properties of the system. For a nanoscale material, when surface/volume ratio is much higher compared to a bulk material, structure and other intrinsic properties are strongly affected by the presence of large surface area. Tribology, i.e. frictional properties have interfacial nature and the tremendously differ at the nanoscale. The goal of this dissertation was to consider some of structural and tribological properties of nanoparticles, nanorods and nanowires, propose corresponding theoretical models and demonstrate several experimental methods based upon those. In particular, structural properties of PNCs concerned with the presence of intrinsic stresses and stress relaxation were investigated and described. Tribological properties of nanoparticles and nanowires on a flat surface were studied and described.

In the present dissertation and previously published papers [17, 85] the model of core/shell formation as a mechanism of stress relaxation in PNRs and INPs was proposed. The model dealt with the formation of a crystal lattice mismatch layer that could diminish the total elastic energy of PNRs and INPs in the framework of the disclination model. On the base of the presented modeling and calculations it was shown that formation of the shell layer with crystal lattice mismatch could diminish the internal energy of the PNRs and INPs. Nanoparticles with core/shell configuration were prepared and observed experimentally [86], where copper nanoparticles were grown with silver shells.

The optimal mismatch parameter  $\varepsilon_{opt}^*$  giving the maximal energy release was determined as  $\varepsilon_{opt}^* \approx -0.01$  for PNR and  $\varepsilon_{opt}^* \approx -0.04$  for INP. The threshold radius as the minimal radius of nanorods or nanoparticles, for which the formation of the layer is energetically favorable was found to be approximately 10 nm for nanoparticles and 100 nm for nanorods of typical FCC metals.

It should be noted that the described model justifies the hollow-core model of relaxation in pentagonal crystals suggested by Romanov *et al.* in [14]. The resulted expression for energy release for both PNR and INP showed energetic favorability of formation of hollow-core in all the range of core radius parameter.

One additional possible stress relaxation mechanism was considered in particular, namely, the appearance of the internal cavity in PRs and PPs, accompanied by the formation of nanowhiskers on the surface of the PRs and PPs.

A possible mechanism addressing the simultaneous emergence of pentagonal nanowhiskers and internal cavities in PRs and PPs based on the nucleation of two dislocation loops of opposite sign near the surface of the crystal with a disclination was described. As a result, vacancy-type dislocation loop remains in the material and acts as a nucleus for pores, while the interstitial loop comes to the free surface, contributing to nanowhisiker growth. Demonstrated calculations provided a qualitative evidence for the formation of nanowhisiker-cavity

pair in a material with disclinations, in particular in PRs and PPs. Therefore a conduction of additional experimental study to verify this hypothesis can be proposed. Moreover, in the development of the given model it would be desirable to elaborate the theoretical explanation and estimation of the critical size of PR and PP as well as the nanowhisker radius.

Numerical simulation of INP manipulation was employed to investigate tribological properties of such objects. A computer program developed for the simulations used to model the INP, which was modeled as a rigid body governed by Newton's laws of motion. In one case when the INP was rested on an atomically flat substrate and affected by a point force the simulations evidenced that the motion of the INP was a combination of translational and rotational motions. The rotation velocity depended on the position of the applied force. In the other case the INP was clutched between 2 atomically flat surfaces while the upper surface was laterally dragged by a spring with a constant velocity. The simulation demonstrated various possibilities of particle motion depending on the surface velocity and the normal load.

The nanomanipulation experimental setup and the QTF force sensor used for investigation of tribological properties of NPs and NWs were described. The setup consisted of an AFM cantilever glued on a QTF mounted onto a high-precision 3D nanomanipulator. The cantilever could be glued in 2 ways, enabling either normal or shear type of oscillations. This system was placed inside a SEM, which enabled real-time visual guidance of the manipulation experiment. A special control and measurement system was developed in order to manage the 3D manipulator and record the signal from the QTF. The calibration procedure was used to match the signal from the QTF and real force applied to the manipulated object.

The manipulations can be performed by a dynamic mode when the manipulating tip is oscillating in either normal or shear modes, or in a static mode, when the tip is not oscillating. The former way allowed measuring the applied force by the tip. However, sometimes the dynamic range of force sensor was not sufficiently wide to register large forces. Therefore both methods were used. The elaborated experimental equipment enabled to manipulate nanocrystals, register the applied force and watch the manipulation process simultaneously. This nanomanipulation setup was applied furthermore to investigate the tribological properties of gold NPs and ZnO NWs on an oxidized Si wafer.

The gold particles of approximately 150 nm in diameter were manipulated using a QTF-based sensor and particle-sample friction was measured. The large variations in the static friction values were attributed to the differences in particle-sample contact areas associated with the shapes of the particles. Thermal treatment of the particles resulted in rounding of the particles and significantly decreased the static friction. Kinetic friction in the most cases did not exceed several nN.

A novel method to determine the elastic and frictional properties of the same NW was also proposed. Distributed kinetic friction and corresponding interfacial shear stress were calculated from the characteristic shape of NW bending

during the translation on a flat substrate. Distributed kinetic friction  $q_{kin}$  and interfacial shear stress  $\sigma_{kin}$  of a ZnO NW on an oxidised Si substrate were found to be  $0.2\pm 0.8$  nN/nm and  $2.1\pm 0.26$  MPa, respectively. Young's modulus was measured for the same set of NWs by bending its half-suspended part and was found to be  $40.4\pm 11$  GPa.

Novel method of *in situ* combined measuring NW-substrate static and kinetic friction was proposed and demonstrated. The friction forces were calculated using bending profile of the NW just before its complete displacement. In some cases the NW was broken and that was used to calculate the tensile strength of the NW.

A model for calculation of distributed static friction force for a bent NW lying upon a flat surface was proposed. An appropriate nanowire backbone skeletonization algorithm was elaborated. The algorithm utilized interpolation polynomials of a special kind and enabled explicit fulfillment of mechanic equilibrium of the nanowire. In contrast to other methods [40, 45], this method enabled to take into account the free ends of the NW and comply the boundary conditions that might significantly influence the result.

As a conclusion, the following several key findings of the thesis can be extracted:

- pentagonal 0D and 1D nanocrystals possess specific structure and properties, particularly mechanical stresses due to their internal defect structure;
- formation of the core/shell structure with crystal lattice mismatch leads to diminishing the elastic energy of pentagonal nanocrystals;
- growth of a whisker is most probably to occur in the presence of mechanical stresses, e.g. in grain boundary junctions and pentagonal nanocrystals;
- tribological properties of 0D and 1D nanocrystals are different from those of macroscale objects;
- atomistic numerical simulations reveal different types of motion of icosahedral nanoparticles manipulated by concentrated or surface forces;
- real-time nanomanipulation experiments can be effectively used to investigate static and kinetic friction of nanoparticles and nanowires on flat substrates;
- nanomanipulation experiments result in the measurements of elastic moduli and bending strength of nanowires providing unique information on mechanical materials properties at the nanoscale.

**Novelty of the results:**

- A new mechanism of stress relaxation in pentagonal nanoparticles and nanorods via formation of a core/shell with crystal lattice mismatch is proposed and demonstrated in the framework of the disclination model

- An original model of nanowhisiker growth in the present of disclination source suitable for pentagonal nanocrystals and triple grain boundary junctions is elaborated
- A numerical simulation model for manipulation of icosahedral nanoparticles in 3D is demonstrated for the first time
- A new real-time nanomanipulation experimental setup with quartz tuning fork enabling either normal or shear oscillation modes and managed by a unique control and measurement system is developed
- Applicability and peculiarities of normal and shear oscillation modes in terms of manipulation of gold nanoparticles are compared and discussed for the first time.
- Novel methods of measurement elastic modulus and various tribological properties of individual nanowires are demonstrated for ZnO nanowires on oxidized Si wafer
- A new method for measurement of kinetic friction of a nanowire on a flat substrate is proposed and experimentally demonstrated
- For the first time the method of combined static and kinetic nanowire friction measurement is presented and experimentally demonstrated
- A new theoretical model and experimental method for measurement of nanowire-substrate static friction distributed along the nanowire are proposed and experimentally demonstrated

## SUMMARY IN ESTONIAN

Uurimistöö “1- ja 0-dimensiooniliste nanokristallide struktuuralsed ja triboloogilised omadused” käsitleb tänapäeva füüsika ja materjaliteaduse üht uurimisvaldkonda – süsteemi omaduste sõltuvust süsteemi suurusest, mis on eriti aktuaalne nanoskaalas süsteemide juures, kus pindala/ruumala suhe on oluliselt suurem kui makroskoopilistes süsteemides.

Töö eesmärgiks oli käsitleda teatavate nanoosakeste ja nanotraatide struktuurilisi ja triboloogilisi omadusi, luua nende kirjeldamiseks teoreetilised mudelid ning töötada välja mudelitel baseeruvad eksperimentaalsed meetodid. Eriline tähelepanu oli suunatud pentagonaalsete nanokristallide uurimisele.

### Töö peamised tulemused:

- Töötati välja uus mehaaniliste pingete relaksatsiooni mehhanism pentagonaalsetes nanoosakestes ja nanotraatides. Mudel baseerub disklinatsioonide teoorial ja seisneb mittekattuva kristallvõre struktuuriga tuuma ja kattekihi tekkimises kirjeldatavates nanostruktuurides.
- Töötati välja originaalne mudel nanonõelte (*i.k. nanowhisker*) tekkimiseks pentagonaalsetes nanokristallides kolme elementaarühiku kokkupuutepunktis.
- Esmakordselt teostati ikosaheedriliste nanoosakeste struktuuri 3D numbriline modelleerimine.
- Töötati välja uus eksperimentaalne nanomanipulatsiooni seade, mis baseerub kahemoodilisel kvartsresonaator-teravikmanipulaatoril ja reaalses elektronmikroskoopilisel visualiseerimisel. Süsteem kasutab väljatöötatud unikaalset juhtimis- ja kontrollsüsteemi.
- Nanomanipulatsiooni erinevate moodide rakendatavust uuriti kulla nanoosakeste näitel.
- Töötati välja uudne meetod nanotraatide elastsusmooduli ja triboloogiliste parameetrite määramiseks. Meetodit rakendati oksüdeeritud Si-alusel olevate ZnO nanotraatide juhul.
- Töötati välja uus meetod siledal pinnal oleva üksiku nanotraadi kineetilise hõõrde teguri määramiseks ja demonstreeriti selle rakendatavust.
- Esmakordselt demonstreeriti eksperimentaalselt nanotraatide staatilise ja kineetilise hõõrde teguri üheaegset määramist.
- Töötati välja uus teoreetiline mudel ja sellele vastav eksperimentaalne meetod jagunenud staatilise hõõrdumise määramiseks nanotraat-aluspind süsteemis.

## REFERENCES

- [1] V. Gryaznov, J. Heydenreich, A. Kaprelov, S. Nepijko, A. E. Romanov, J. Urban, Pentagonal symmetry and disclinations in small particles, *Crystal Research and Technology* **34**, 1091–1119 (1999).
- [2] H. Hofmeister, Forty years study of fivefold twinned structures in small particles and thin films, *Crystal Research and Technology* **33**, 3–25 (1998).
- [3] M. J. Yacamán, J. A. Ascencio, H. B. Liu, J. Gardea-Torresdey, Structure shape and stability of nanometric sized particles, *Journal of Vacuum Science & Technology B: Microelectronics and Nanometer Structures* **19**, 1091 (2001).
- [4] K. Koga, K. Sugawara, Population statistics of gold nanoparticle morphologies: direct determination by HREM observations, *Surface Science* **529**, 23–35 (2003).
- [5] D. Seo, C. Yoo, I. S. Chung, S. M. Park, S. Ryu, H. Song, Shape adjustment between multiply twinned and single-crystalline polyhedral gold nanocrystals: decahedra, icosahedra, and truncated tetrahedra, *The Journal of Physical Chemistry C* **112**, 2469–2475 (2008).
- [6] I. Yasnikov, Elastic stress relaxation in pentagonal fine particles and crystallites of electrolytic origin, *Technical Physics* **52**, 666–667 (2007).
- [7] R. Wit, Partial disclinations, *Journal of Physics C: Solid State Physics* **5**, 529–534 (1972).
- [8] A. Howie, L. Marks, Elastic strains and the energy balance for multiply twinned particles, *Philosophical Magazine A* **49**, 95–109 (1984).
- [9] V. G. Gryaznov, A. M. Kaprelov, A. E. Romanov, I. A. Polonskii, Channels of relaxation of elastic stresses in pentagonal nanoparticles, *Physica Status Solidi (b)* **167**, 441–450 (1991).
- [10] A. E. Romanov, V. Vladimirov, in *Dislocations in Solids, Vol. 9*, F. Nabarro, Ed. (Elsevier Science Publishers B.V., 1992), pp. 192–402.
- [11] Y. Sun, Y. Xia, Multiple-Walled Nanotubes Made of Metals, *Advanced Materials* **16**, 264–268 (2004).
- [12] A. L. Kolesnikova, A. E. Romanov, Stress relaxation in pentagonal whiskers, *Technical Physics Letters* **33**, 886–888 (2007).
- [13] L. D. Marks, Experimental studies of small particle structures, *Reports on Progress in Physics* **57**, 603–649 (1994).
- [14] A. E. Romanov, I. A. Polonsky, V. G. Gryaznov, S. A. Nepijko, T. Junghanns, N. J. Vitrykhovski, Voids and channels in pentagonal crystals, *Journal of Crystal Growth* **129**, 691–698 (1993).
- [15] A. E. Romanov, A. L. Kolesnikova, Application of disclination concept to solid structures, *Progress in Materials Science* **54**, 740–769 (2009).
- [16] A. I. Mikhailin, A. E. Romanov, Amorphization of a disclination core, *Soviet Physics, Solid State* **28**, 337–338 (1986).
- [17] L. M. Dorogin, S. Vlassov, A. L. Kolesnikova, I. Kink, R. Lohmus, A. E. Romanov, Crystal mismatched layers in pentagonal nanorods and nanoparticles, *Physica Status Solidi (b)* **247**, 288–298 (2010).
- [18] A. A. Vikarchuk, A. P. Volenko, Pentagonal Copper Crystals: Various Growth Shapes and Specific Features of Their Internal Structure, *Physics of the Solid State* **47**, 352–356 (2005).
- [19] M. O. Peach, Mechanism of growth of whiskers on cadmium, *Journal of Applied Physics* **23**, 1401–1403 (1952).

- [20] J. Eshelby, A tentative theory of metallic whisker growth, *Physical Review* **91**, 755–756 (1953).
- [21] U. Lindborg, A model for the spontaneous growth zinc, cadmium and tin whiskers, *Acta Metallurgica* **24**, 181–186 (1976).
- [22] K. Tu, J. Li, Spontaneous whisker growth on lead-free solder finishes, *Materials Science and Engineering: A* **409**, 131–139 (2005).
- [23] J. Zhao, P. Su, M. Ding, Microstructure-based stress modeling of tin whisker growth, *IEEE Transactions on Electronics Packaging Manufacturing* **29**, 265–273 (2006).
- [24] J. Smetana, Theory of Tin Whisker Growth: “The End Game,” *IEEE Transactions on Electronics Packaging Manufacturing* **30**, 11–22 (2007).
- [25] L. Prandtl, Ein Gedankenmodell zur kinetischen Theorie der festen Körper, *Journal of Applied Mathematics and Mechanics* **8**, 85–106 (1928).
- [26] G. Tomlinson, A molecular theory of friction, *Philosophical Magazine* **7**, 905–939 (1929).
- [27] H. Ahmed, Single electron electronics: Challenge for nanofabrication, *Journal of Vacuum Science & Technology B: Microelectronics and Nanometer Structures* **15**, 2101–2108 (1997).
- [28] H.-J. Butt, B. Cappella, M. Kappl, Force measurements with the atomic force microscope: Technique, interpretation and applications, *Surface Science Reports* **59**, 1–152 (2005).
- [29] F. J. Giessibl, Advances in atomic force microscopy, *Reviews of Modern Physics* **75**, 949–983 (2003).
- [30] K. Mougín, E. Gnecco, A. Rao, M. T. Cuberes, S. Jayaraman, E. W. McFarland, H. Haidara, E. Meyer, Manipulation of gold nanoparticles: influence of surface chemistry, temperature, and environment (vacuum versus ambient atmosphere), *Langmuir* **24**, 1577–81 (2008).
- [31] C. Ritter, M. Heyde, B. Stegemann, K. Rademann, U. Schwarz, Contact-area dependence of frictional forces: Moving adsorbed antimony nanoparticles, *Physical Review B* **71**, 085405 (2005).
- [32] S. Kim, D. C. Ratchford, X. Li, Atomic Force Microscope Nanomanipulation with Simultaneous Visual Guidance, *ACS Nano* **3**, 2989–2994 (2009).
- [33] C. Baur, A. Bugacov, B. E. Koel, A. Madhukar, N. Montoya, T. R. Ramachandran, A. A. G. Requicha, R. Resch, P. Will, Nanoparticle manipulation by mechanical pushing: underlying phenomena and real-time monitoring, *Nanotechnology* **9**, 360–364 (1998).
- [34] D. Dietzel, M. Feldmann, H. Fuchs, U. D. Schwarz, A. Schirmeisen, Transition from static to kinetic friction of metallic nanoparticles, *Applied Physics Letter* **95**, 053104 (2009).
- [35] M. Sitti, H. Hashimoto, Controlled Pushing of Nanoparticles: Modeling and Experiments, *IEEE/ASME Transactions on Mechatronics* **5**, 199–211 (2000).
- [36] D. Dietzel, T. Mönninghoff, L. Jansen, H. Fuchs, C. Ritter, U. D. Schwarz, A. Schirmeisen, Interfacial friction obtained by lateral manipulation of nanoparticles using atomic force microscopy techniques, *Journal of Applied Physics* **102**, 084306 (2007).
- [37] P. X. Gao, J. Song, J. Liu, Z. L. Wang, Nanowire Piezoelectric Nanogenerators on Plastic Substrates as Flexible Power Sources for Nanodevices, *Advanced Materials* **19**, 67–72 (2007).

- [38] K. H. Liu, P. Gao, Z. Xu, X. D. Bai, E. G. Wang, In situ probing electrical response on bending of ZnO nanowires inside transmission electron microscope, *Applied Physics Letters* **92**, 213105 (2008).
- [39] G. Conache, A. Ribayrol, L. Fröberg, M. Borgström, L. Samuelson, L. Montelius, H. Pettersson, S. Gray, Bias-controlled friction of InAs nanowires on a silicon nitride layer studied by atomic force microscopy, *Physical Review B* **82**, 035403 (2010).
- [40] M. C. Strus, R. R. Lahiji, P. Ares, V. Lopez, A. Raman, R. Reifengerger, Strain energy and lateral friction force distributions of carbon nanotubes manipulated into shapes by atomic force microscopy, *Nanotechnology* **20**, 385709 (2009).
- [41] D. Askari, G. Feng, Finite element analysis of nanowire indentation on a flat substrate, *Journal of Materials Research* **27**, 586–591 (2012).
- [42] A. Kulkarni, M. Zhou, F. Ke, Orientation and size dependence of the elastic properties of zinc oxide nanobelts, *Nanotechnology* **16**, 2749–2756 (2005).
- [43] S. Timoshenko, J. Goodier, *Theory of elasticity* (McGraw-Hill Book Company, 2nd ed., 1951).
- [44] L. Landau, E. Lifshitz, *Theory of Elasticity* (Butterworth-Heinemann, Oxford, 3rd ed., 1986).
- [45] M. Bordag, A. Ribayrol, G. Conache, L. E. Fröberg, S. Gray, L. Samuelson, L. Montelius, H. Pettersson, Shear Stress Measurements on InAs Nanowires by AFM Manipulation, *Small* **3**, 1398–1401 (2007).
- [46] R. Feynman, There's plenty of room at the bottom [data storage], *Journal of Microelectromechanical Systems* **1**, 60–66 (1992).
- [47] M. Evstigneev, P. Reimann, Rolling and sliding of a nanorod between two planes: Tribological regimes and control of friction, *Physical Review B* **85**, 035447 (2012).
- [48] M. Evstigneev, P. Reimann, Langevin equation for a system nonlinearly coupled to a heat bath, *Physical Review B* **82**, 224303 (2010).
- [49] R. He, P. Yang, Giant piezoresistance effect in silicon nanowires, *Nature nanotechnology* **1**, 42–46 (2006).
- [50] Z. L. Wang, J. Song, Piezoelectric Nanogenerators Based on Zinc Oxide Nanowire Arrays, *Science* **312**, 242–246 (2010).
- [51] G. Conache, S. M. Gray, A. Ribayrol, L. E. Fröberg, L. Samuelson, H. Pettersson, L. Montelius, Friction Measurements of InAs Nanowires on Silicon Nitride by AFM Manipulation, *Small* **5**, 203–207 (2009).
- [52] J. Chen, G. Conache, M.-E. Pistol, S. M. Gray, M. T. Borgström, H. Xu, H. Q. Xu, L. Samuelson, U. Håkanson, Probing Strain in Bent Semiconductor Nanowires with Raman Spectroscopy, *Nano Letters* **11**, 1280–1286 (2010).
- [53] K. Johnson, K. Kendall, A. Roberts, Surface energy and the contact of elastic solids, *Proceeding of the Royal Society of London A* **324**, 301–313 (1971).
- [54] B. Derjaguin, V. Muller, Y. P. Toporov, Effect of contact deformations on the adhesion of particles, *Journal of Colloid and Interface Science* **53**, 314–326 (1975).
- [55] J. P. Hirth, J. Lothe, *Theory of Dislocations* (Wiley, New-York, 1982).
- [56] A. T. Kosilov, A. Malivanchuk, E. Mikhailov, Molecular dynamics simulation of Cu-Ni and Cu-Pd binary clusters, *Physics of the Solid State* **50**, 1392–1396 (2008).
- [57] F. Baletto, C. Mottet, R. Ferrando, Growth simulations of silver shells on copper and palladium nanoclusters, *Physical Review B* **66**, 155420 (2002).
- [58] V. Rybin, *Large plastic deformations and fracture of metals* (Metalurgia, in Russian, Moscow, 1986).

- [59] A. L. Kolesnikova, A. E. Romanov, *Circular dislocation-disclination loops and their application to solution of the boundary value problems in the theory of defects* (USSR's Academy of Sciences, in Russian, Leningrad, 1986).
- [60] A. L. Kolesnikova, A. E. Romanov, Virtual Circular Dislocation-Disclination Loop Technique in Boundary Value Problems in the Theory of Defects, *Journal of Applied Mechanics* **71**, 409–417 (2004).
- [61] N. J. Salamon, G. G. Walter, Limits of Lipschitz-Hankel Integrals, *Journal of the Institute of Mathematics and Its Applications* **24**, 237–254 (1979).
- [62] N. Salamon, J. Dundurs, Elastic fields of a dislocation loop in a two-phase material, *Journal of Elasticity* **1**, 153–164 (1971).
- [63] J. C. Butcher, *Numerical methods for ordinary differential equations* (John Wiley & Sons, 2003).
- [64] A. J. Melmed, The art and science and other aspects of making sharp tips, *Journal of Vacuum Science & Technology B* **9**, 601–608 (1991).
- [65] S. Rozhok, V. Chandrasekhar, Application of commercially available cantilevers in tuning fork Scanning Probe Microscopy (SPM) studies, *Solid State Communications* **121**, 683–686 (2002).
- [66] S. C. Fain, K. A. Barry, M. G. Bush, B. Pittenger, R. N. Louie, Measuring average tip-sample forces in intermittent-contact (tapping) force microscopy in air, *Applied Physics Letters* **76**, 930–932 (2000).
- [67] C. Su, L. Huang, K. Kjoller, Direct measurement of tapping force with a cantilever deflection force sensor, *Ultramicroscopy* **100**, 233–239 (2004).
- [68] S. M. Cook, T. E. Schäffer, K. M. Chynoweth, M. Wigton, R. W. Simmonds, K. M. Lang, Practical implementation of dynamic methods for measuring atomic force microscope cantilever spring constants, *Nanotechnology* **17**, 2135–2145 (2006).
- [69] S. Vlassov, B. Polyakov, L. M. Dorigin, A. Löhmus, A. E. Romanov, I. Kink, E. Gnecco, R. Löhmus, Real-time manipulation of gold nanoparticles inside a scanning electron microscope, *Solid State Communications* **151**, 688–692 (2011).
- [70] J. Dietrich, Time-dependent friction and the mechanics of stick slip, *Pure and Applied Geophysics* **116**, 790–806 (1978).
- [71] D. Dietzel, C. Ritter, T. Mönninghoff, H. Fuchs, A. Schirmeisen, U. D. Schwarz, Frictional Duality Observed during Nanoparticle Sliding, *Physical Review Letters* **101**, 125505 (2008).
- [72] R. W. Carpick, M. Salmeron, Scratching the Surface: Fundamental Investigations of Tribology with Atomic Force Microscopy, *Chemical Reviews* **97**, 1163–1194 (1997).
- [73] D. Tabor, Surface forces and surface interactions, *Journal of Colloid and Interface Science* **58**, 2–13 (1977).
- [74] A. Cottrel, *Dislocations and Plastic Flowing Crystals* (Oxford University Press, Oxford, 1953).
- [75] R. Resch, A. Bugacov, C. Baur, B. E. Koel, A. Madhukar, A. A. G. Requicha, P. Will, Manipulation of nanoparticles using dynamic force microscopy: simulation and experiments, *Applied Physics A: Materials Science & Processing* **67**, 265–271 (1998).
- [76] Z. Zhu, T.-L. Chen, Y. Gu, J. Warren, R. M. J. Osgood, Zinc Oxide Nanowires Grown by Vapor-Phase Transport Using Selected Metal Catalysts: A Comparative Study, *Chemistry of Materials* **17**, 4227–4234 (2005).

- [77] M. Manoharan, A. Desai, G. Neely, Synthesis and elastic characterization of zinc oxide nanowires, *Journal of Nanomaterials* **2008**, 1–7 (2008).
- [78] J. Song, X. Wang, E. Riedo, Z. L. Wang, Elastic property of vertically aligned nanowires, *Nano Letters* **5**, 1954–1958 (2005).
- [79] A. Desai, M. Haque, Mechanical properties of ZnO nanowires, *Sensors and Actuators A* **134**, 169–176 (2007).
- [80] M. Manoharan, M. Haque, Role of adhesion in shear strength of nanowire–substrate interfaces, *Journal of Physics D: Applied Physics* **42**, 095304 (2009).
- [81] B. Polyakov, L. M. Dorogin, S. Vlassov, I. Kink, A. Lohmus, A. E. Romanov, R. Lohmus, Real-time measurements of sliding friction and elastic properties of ZnO nanowires inside a scanning electron microscope, *Solid State Communications* **151**, 1244–1247 (2011).
- [82] S. Hoffmann, F. Östlund, J. Michler, H. J. Fan, M. Zacharias, S. H. Christiansen, C. Ballif, Fracture strength and Young’s modulus of ZnO nanowires, *Nanotechnology* **18**, 205503 (2007).
- [83] L. M. Dorogin, B. Polyakov, A. Petruhins, S. Vlassov, R. Lohmus, I. Kink, A. E. Romanov, Modeling of kinetic and static friction between an elastically bent nanowire and a flat surface, *Journal of Materials Research* **27**, 580–585 (2012).
- [84] Z. L. Wang, R. Yang, J. Zhou, Y. Qin, C. Xu, Y. Hu, S. Xu, Lateral nanowire/nanobelt based nanogenerators, piezotronics and piezo-phototronics, *Materials Science and Engineering R* **70**, 320–329 (2010).
- [85] L. M. Dorogin, A. L. Kolesnikova, A. E. Romanov, Misfit Layer Formation in Icosahedral Nanoparticles, *Technical Physics Letters* **34**, 779–781 (2008).
- [86] C. Langlois, D. Alloyeau, Y. L. Bouar, A. Loiseau, T. Oikawa, C. Mottet, C. Ricolleau, Growth and structural properties of CuAg and CoPt bimetallic nanoparticles, *Faraday Discussions* **138**, 375–391 (2008).

## **ACKNOWLEDGEMENTS**

First of all I would like to thank my supervisors Dr. Ilmar Kink and Prof. Alexey Romanov for involving and valuable support of my research activity. I am also grateful to Dr. Rünno Lõhmus for managing and coordination of the nanomanipulation project.

I would also like to thank all the coauthors for pleasant team-work. Especially I am thankful to Dr. Boris Polyakov and Dr. Sergei Vlassov for strong experimental management, to Dr. Anna Kolesnikova for extensive theoretical support, Dr. Ants Lõhmus for all kinds of support and advising during my studies in the University of Tartu, to Dr. Vambola Kisand for help on educational side and paperwork, and to all other colleagues. I am also grateful to Madis Lobjakas for technical assistance.

Many thanks to Dr. Enrico Gnecco for warm welcome at the Madrid Institute for Advanced Studies (IMDEA Nanociencia) and for sharing his knowledge and experience in the field of nanotribology. Warm thanks to my parents and grandparents for their profound support and care. I would also express gratitude to my little for kindness and wholehearted support.

The work was supported by the Estonian Science Foundation grants no. 8428, 8377 and 8420; Estonian research targeted project SF0180058s07; Graduate School on Functional Materials and Technologies; EU Social Funds project 1.2.0401.09-0079; University of Tartu; Estonian Nanotechnology Competence Centre and by ESF FANAS program "Nanoparma".

## APPENDIX

### A1. Basic formulas of the linear theory of elasticity

Tensor of small strain  $\varepsilon_{ij}$ :

$$\varepsilon_{ij} = \frac{1}{2} \left( \frac{\partial u_i}{\partial x_j} + \frac{\partial u_j}{\partial x_i} \right), \quad (i, j = x, y, z; \quad x_i, x_j = x, y, z), \quad (\text{A1.1})$$

where  $u_i$  is the field of displacements.

Elastic strains are related to mechanical stresses  $\sigma_{ij}$  in the body by Hook's law. In the framework of isotropic approximation the Hook's law has the following form:

$$\sigma_{ij} = 2G(\varepsilon_{ij} + \frac{\nu}{1-2\nu} \varepsilon \delta_{ij}), \quad \delta_{ij} = \begin{cases} 1, & i = j \\ 0, & i \neq j \end{cases}, \quad i, j = x, y, z, \quad (\text{A1.2})$$

where  $G$  is shear modulus,  $\nu$  is Poisson's ratio, and  $\varepsilon = \text{Tr } \varepsilon_{ij}$ .

It is also possible to represent strain tensor  $\varepsilon_{ij}$  through  $\sigma_{ij}$ :

$$\varepsilon_{ij} = \frac{1}{2G} (\sigma_{ij} - \frac{\nu}{1+\nu} \sigma \delta_{ij}), \quad \delta_{ij} = \begin{cases} 1, & i = j \\ 0, & i \neq j \end{cases}, \quad i, j = x, y, z \quad (\text{A1.3})$$

where  $\sigma = \text{Tr } \sigma_{ij}$ .

Within the condition of absence of volumetric forces, the equations of equilibrium are as following:

$$\nabla_i \sigma_{ij} = 0 \quad (i, j = x, y, z). \quad (\text{A1.4})$$

Tensors  $\sigma_{ij}$  and  $\varepsilon_{ij}$  are symmetric:  $\sigma_{ij} = \sigma_{ji}$ ,  $\varepsilon_{ij} = \varepsilon_{ji}$ .

Elastic energy corresponding to the fields  $\sigma_{ij}$  and  $\varepsilon_{ij}$  is determined by:

$$E = \frac{1}{2} \int_V \sigma_{ij} \varepsilon_{ij} dV, \quad (\text{A1.5})$$

where  $V$  is the volume of the body.

Interaction energy of two elastic fields  $(\sigma'_{ij}, \varepsilon'_{ij})$  and  $(\sigma''_{ij}, \varepsilon''_{ij})$  are yielded in the form:

$$E_{\text{int}} = \int_V \sigma'_{ij} \varepsilon''_{ij} dV = \int_V \sigma''_{ij} \varepsilon'_{ij} dV. \quad (\text{A1.6})$$

In the theory of defects the elastic energy of a defect is determined by the expression:

$$E = -\frac{1}{2} \int_V \sigma_{ij} \varepsilon_{ij}^* dV, \quad (\text{A1.7})$$

where  $\varepsilon_{ij}^*$  the eigenstrain tensor components,  $\sigma_{ij}$  is the stress field of the defect.

Interaction energy of two defects can be found with use of either of these relationships:

$$E_{\text{int}} = -\int_V \sigma'_{ij} \varepsilon''_{ij} dV = -\int_V \sigma''_{ij} \varepsilon'_{ij} dV, \quad (\text{A1.8})$$

where  $\varepsilon'_{ij}$ ,  $\varepsilon''_{ij}$  are eigenstrains of the defects,  $\sigma'_{ij}$ ,  $\sigma''_{ij}$  are the stress fields of the defects.

For instance, interaction energy between a spherical inclusion characterized by the eigenstrain  $\varepsilon_{ii}^* = \varepsilon^*$  ( $i = x, y, z$ ), and the stress field  $\sigma_{ij}$  is determined by a simple expression:

$$E_{\text{int}} = -4\pi \int_0^{R_{\text{core}}} \varepsilon^* \text{Tr} \sigma_{ij} r^2 dr, \quad (\text{A1.9})$$

where  $R_{\text{core}}$  is the radius of the inclusion,  $\text{Tr} \sigma_{ij} = \sum_i \sigma_{ii}$ .

In spherical coordinates  $(R, \theta, \varphi)$  the strain tensor  $\varepsilon_{ij}$  is related to the displacements  $u_{ij}$  as:

$$\begin{aligned} \varepsilon_{RR} &= \frac{\partial u_R}{\partial R}, & \varepsilon_{R\theta} &= \frac{1}{2} \left( \frac{1}{R} \frac{\partial u_R}{\partial \theta} + \frac{\partial u_\theta}{\partial R} - \frac{u_\theta}{R} \right), \\ \varepsilon_{R\phi} &= \frac{1}{2} \left( \frac{1}{R \sin \theta} \frac{\partial u_R}{\partial \phi} + \frac{\partial u_\phi}{\partial R} - \frac{u_\phi}{R} \right), \end{aligned} \quad (\text{A1.10})$$

$$\varepsilon_{\theta\theta} = \frac{1}{R} \frac{\partial u_\theta}{\partial \theta} + \frac{u_R}{R},$$

$$\varepsilon_{\theta\phi} = \frac{1}{2} \left( \frac{1}{R \sin \theta} \frac{\partial u_\theta}{\partial \phi} + \frac{1}{R} \frac{\partial u_\phi}{\partial \theta} - \frac{u_\phi}{R} \operatorname{ctg} \theta \right),$$

$$\varepsilon_{\phi\phi} = \frac{1}{R \sin \theta} \frac{\partial u_\phi}{\partial \phi} + \frac{u_\theta}{R} \operatorname{ctg} \theta + \frac{u_R}{R}.$$

The equations of equilibrium in the spherical coordinates are as following:

$$\left\{ \begin{array}{l} \frac{\partial \sigma_{RR}}{\partial R} + \frac{1}{R \sin \theta} \frac{\partial \sigma_{R\phi}}{\partial \phi} + \frac{1}{R} \frac{\partial \sigma_{R\theta}}{\partial \theta} + \frac{2\sigma_{RR} - \sigma_{\phi\phi} - \sigma_{\theta\theta} + \sigma_{R\theta} \operatorname{ctg} \theta}{R} = 0, \\ \frac{\partial \sigma_{R\phi}}{\partial R} + \frac{1}{R \sin \theta} \frac{\partial \sigma_{\phi\phi}}{\partial \phi} + \frac{1}{R} \frac{\partial \sigma_{\phi\theta}}{\partial \theta} + \frac{3\sigma_{R\phi} + 2\sigma_{\phi\theta} \operatorname{ctg} \theta}{R} = 0, \\ \frac{\partial \sigma_{R\theta}}{\partial R} + \frac{1}{R \sin \theta} \frac{\partial \sigma_{\phi\theta}}{\partial \phi} + \frac{1}{R} \frac{\partial \sigma_{\theta\theta}}{\partial \theta} + \frac{3\sigma_{R\theta} + (\sigma_{\theta\theta} - \sigma_{\phi\phi}) \operatorname{ctg} \theta}{R} = 0, \end{array} \right. \quad (\text{A1.11})$$

where the same designations as in (A1.10) are used.

## A2. Unit quaternions for rotation of a rigid body

Quaternions are 4-component objects of a form  $q = s + v_x \mathbf{i} + v_y \mathbf{j} + v_z \mathbf{k}$ . Multiplication of two quaternions  $q_1 = [s_1, \mathbf{v}_1]$  and  $q_2 = [s_2, \mathbf{v}_2]$  is defined as

$$q_1 q_2 = [s_1 s_2 - \mathbf{v}_1 \cdot \mathbf{v}_2, s_1 \mathbf{v}_2 + s_2 \mathbf{v}_1 + \mathbf{v}_1 \times \mathbf{v}_2]. \quad (\text{A2.1})$$

Norm of a quaternion  $q = s + v_x \mathbf{i} + v_y \mathbf{j} + v_z \mathbf{k}$  is defined as  $\|q\| = \sqrt{s^2 + v_x^2 + v_y^2 + v_z^2}$ .

Unit quaternions with  $\|q\| = 1$  are a convenient way for representation of the rotation of a rigid body in computer simulations. Each unit quaternion can be linked with a rotation matrix. Due to round-off errors, for instance, during solving equations of motion, rotation matrix is corrupted and becomes no longer an exact rotation matrix (that is observed as “distortions” of the rotated body). On the other hand, upon corruption of the quaternion, it can be renormalized to be unit on each step. That guarantees that the rotation will be saved from undesired distortions.

Conversion of a quaternion  $q = [s, \mathbf{v}] = (s, v_x, v_y, v_z) = s + v_x \mathbf{i} + v_y \mathbf{j} + v_z \mathbf{k}$  to a rotation matrix

$$W = \begin{pmatrix} 1 - 2v_y^2 - 2v_z^2 & 2v_x v_y - 2sv_z & 2v_x v_z + 2sv_y \\ 2v_x v_y + 2sv_z & 1 - 2v_x^2 - 2v_z^2 & 2v_y v_z - 2sv_x \\ 2v_x v_z - 2sv_y & 2v_y v_z + 2sv_x & 1 - 2v_x^2 - 2v_y^2 \end{pmatrix}. \quad (\text{A2.2})$$

Therefore the final position of a point in the body is  $\mathbf{r}' = \mathbf{r}_0 + W\mathbf{r}$ , where  $\mathbf{r}_0$  is a fixed point in the body (e.g. center of mass), and  $\mathbf{r}$  is the radius-vector of the point relative to  $\mathbf{r}_0$  in the initial configuration.

The relation between the quaternion derivative with angular velocity  $\boldsymbol{\omega}$  represented by a quaternion  $\omega = [0, \boldsymbol{\omega}]$ :

$$\dot{q} = \frac{1}{2} \boldsymbol{\omega} q. \quad (\text{A2.3})$$

### A3. Solution for disclination in two-phase cylinder

$$\begin{aligned} B_1 = & -(\boldsymbol{\omega} \log(t) \\ & (t^2 (2v_1^2 + v_1 - 1) (t^2 (2v_2 - 1) - 1) G_1^2 + G_2 (-2v_1 - 1) (v_2 + v_1 (4v_2 + 1) - 2) \\ & t^4 + (v_1 + 2(2v_1(v_1 + 1) - 1)v_2 - 1)t^2 - (2v_1 - 1)(v_2 + 1)) G_1 + \\ & (t^2 - 1) G_2^2 (2v_1 - 1) (t^2 (2v_1 - 1) - 1) (v_2 + 1)) / \\ & (4\pi(v_1 - 1) (t^2 (v_1 + 1) (t^2 (2v_2 - 1) - 1) G_1^2 + (t^2 - 1) G_2 \\ & (-v_2 + v_1 (4v_2 + 1) - 2) t^2 + v_2 + 1) G_1 + (t^2 - 1)^2 G_2^2 (2v_1 - 1) (v_2 + 1))) \end{aligned} \quad (\text{A3.1})$$

$$\begin{aligned} B_2 = & (t^2 \boldsymbol{\omega} \log(t) (-t^2 - 1) (2v_1 - 1) (2v_2^2 + v_2 - 1) G_2^2 + \\ & G_1 (-v_1 t^2 + 2t^2 + 2(t^2 + (4t^2 - 2)v_1 - 2)v_2^2 - (5t^2 + 2(t^2 - 2)v_1 - 3)v_2 - 1) \\ & G_2 - t^2 G_1^2 (v_1 + 1) (1 - 2v_2^2)) / \\ & (4\pi(v_2 - 1) (t^2 (v_1 + 1) (t^2 (2v_2 - 1) - 1) G_1^2 + (t^2 - 1) G_2 \\ & (-v_2 + v_1 (4v_2 + 1) - 2) t^2 + v_2 + 1) G_1 + (t^2 - 1)^2 G_2^2 (2v_1 - 1) (v_2 + 1))) \end{aligned} \quad (\text{A3.2})$$

$$\begin{aligned} C_2 = & (t^2 \boldsymbol{\omega} \log(t) R_s^2 \\ & (t^2 (v_1 + 1) (2v_2 - 1) G_1^2 + G_2 (-v_1 (4v_2 + 1) t^2 + 2t^2 + v_2 (-t^2 + 2v_2 + 1) - 1) \\ & G_1 + (t^2 - 1) G_2^2 (2v_1 - 1) (v_2 + 1)) / \\ & (4\pi(v_2 - 1) (t^2 (v_1 + 1) (t^2 (2v_2 - 1) - 1) G_1^2 + (t^2 - 1) G_2 \\ & (-v_2 + v_1 (4v_2 + 1) - 2) t^2 + v_2 + 1) G_1 + (t^2 - 1)^2 G_2^2 (2v_1 - 1) (v_2 + 1))) \end{aligned} \quad (\text{A3.3})$$

$$D = \frac{t^2 \omega \log(t) G_1 G_2 (v_1 - v_2)}{(\pi (t^2 (v_1 + 1) (t^2 (2v_2 - 1) - 1) G_1^2 + (t^2 - 1) G_2 (-(v_2 + v_1 (4v_2 + 1) - 2)t^2 + v_2 + 1) G_1 + (t^2 - 1)^2 G_2^2 (2v_1 - 1) (v_2 + 1)))}$$

(A3.4)

#### A4. Solution for mismatched two-phase cylinder

$$B_1 = \frac{-(G_2 (v_2 + 1) (t^2 - 1) \varepsilon^* (G_2 (2v_1 - 1) (t^2 - 1) + G_1 (t^2 - v_1 (2t^2 + 1))))}{(G_1^2 (v_1 + 1) t^2 (2v_2 t^2 - t^2 - 1) - G_2 G_1 (t^2 - 1) (v_1 (4v_2 + 1) t^2 + v_2 (t^2 - 1) - 2t^2 - 1) + G_2^2 (2v_1 - 1) (v_2 + 1) (t^2 - 1)^2)}$$

(A4.1)

$$D_1 = \frac{-(G_2 (v_2 + 1) (t^2 - 1) \varepsilon^* (G_2 (2v_1 - 1) (t^2 - 1) + G_1 (-2v_1 t^2 + t^2 + 1)))}{(G_1^2 (v_1 + 1) t^2 (2v_2 t^2 - t^2 - 1) - G_2 G_1 (t^2 - 1) (v_1 (4v_2 + 1) t^2 + v_2 (t^2 - 1) - 2t^2 - 1) + G_2^2 (2v_1 - 1) (v_2 + 1) (t^2 - 1)^2)}$$

(A4.2)

$$B_2 = \frac{(G_1 (v_1 + 1) t^2 \varepsilon^* (G_1 (v_2 (2t^2 + 1) - t^2) - G_2 (2v_2 - 1) (t^2 - 1)))}{(G_1^2 (v_1 + 1) t^2 (2v_2 t^2 - t^2 - 1) - G_2 G_1 (t^2 - 1) (v_1 (4v_2 + 1) t^2 + v_2 (t^2 - 1) - 2t^2 - 1) + G_2^2 (2v_1 - 1) (v_2 + 1) (t^2 - 1)^2)}$$

(A4.3)

$$C_2 = \frac{-(G_1 (v_1 + 1) (v_2 + 1) t^2 \varepsilon^* ((G_1 - G_2) t^2 + G_2) R_s^2)}{(G_1^2 (v_1 + 1) t^2 (2v_2 t^2 - t^2 - 1) - G_2 G_1 (t^2 - 1) (v_1 (4v_2 + 1) t^2 + v_2 (t^2 - 1) - 2t^2 - 1) + G_2^2 (2v_1 - 1) (v_2 + 1) (t^2 - 1)^2)}$$

(A4.4)

$$D_2 = \frac{(G_1 (v_1 + 1) t^2 \varepsilon^* (G_1 (2v_2 t^2 - t^2 - 1) - G_2 (2v_2 - 1) (t^2 - 1)))}{(G_1^2 (v_1 + 1) t^2 (2v_2 t^2 - t^2 - 1) - G_2 G_1 (t^2 - 1) (v_1 (4v_2 + 1) t^2 + v_2 (t^2 - 1) - 2t^2 - 1) + G_2^2 (2v_1 - 1) (v_2 + 1) (t^2 - 1)^2)}$$

(A4.5)

$$\varepsilon_{rr(\varepsilon^*)}^{(1)} = \frac{-(G_2 (v_2 + 1) (t^2 - 1) \varepsilon^* (G_2 (2v_1 - 1) (t^2 - 1) + G_1 (t^2 - v_1 (2t^2 + 1))))}{(G_1^2 (v_1 + 1) t^2 (2v_2 t^2 - t^2 - 1) - G_2 G_1 (t^2 - 1) (v_1 (4v_2 + 1) t^2 + v_2 (t^2 - 1) - 2t^2 - 1) + G_2^2 (2v_1 - 1) (v_2 + 1) (t^2 - 1)^2)}$$

(A4.6)

$$\mathcal{E}_{rr(\varepsilon^*)}^{(2)} = \frac{(G_1(v_1+1)t^2\varepsilon^*(G_1(r^2(v_2+2v_2t^2-t^2)+(v_2+1)t^2R_s^2) - G_2(t^2-1)((2v_2-1)r^2+(v_2+1)R_s^2)))/}{(r^2(G_1^2(v_1+1)t^2(2v_2t^2-t^2-1) - G_2G_1(t^2-1)(v_1(4v_2+1)t^2 + v_2(t^2-1) - 2t^2-1) + G_2^2(2v_1-1)(v_2+1)(t^2-1)^2))} \quad (\text{A4.7})$$

$$\mathcal{E}_{\varphi\varphi(\varepsilon^*)}^{(1)} = \frac{-(G_2(v_2+1)(t^2-1)\varepsilon^*(G_2(2v_1-1)(t^2-1) + G_1(t^2-v_1(2t^2+1))))/}{(G_1^2(v_1+1)t^2(2v_2t^2-t^2-1) - G_2G_1(t^2-1)(v_1(4v_2+1)t^2 + v_2(t^2-1) - 2t^2-1) + G_2^2(2v_1-1)(v_2+1)(t^2-1)^2)} \quad (\text{A4.8})$$

$$\mathcal{E}_{\varphi\varphi(\varepsilon^*)}^{(2)} = \frac{(G_1(v_1+1)t^2\varepsilon^*(G_2(t^2-1)((1-2v_2)r^2+(v_2+1)R_s^2) + G_1(r^2(v_2+2v_2t^2-t^2) - (v_2+1)t^2R_s^2)))/}{(r^2(G_1^2(v_1+1)t^2(2v_2t^2-t^2-1) - G_2G_1(t^2-1)(v_1(4v_2+1)t^2 + v_2(t^2-1) - 2t^2-1) + G_2^2(2v_1-1)(v_2+1)(t^2-1)^2))} \quad (\text{A4.9})$$

$$\mathcal{E}_{zz(\varepsilon^*)}^{(1)} = \frac{-(G_2(v_2+1)(t^2-1)\varepsilon^*(G_2(2v_1-1)(t^2-1) + G_1(-2v_1t^2+t^2+1)))/}{(G_1^2(v_1+1)t^2(2v_2t^2-t^2-1) - G_2G_1(t^2-1)(v_1(4v_2+1)t^2 + v_2(t^2-1) - 2t^2-1) + G_2^2(2v_1-1)(v_2+1)(t^2-1)^2)} \quad (\text{A4.10})$$

$$\mathcal{E}_{zz(\varepsilon^*)}^{(2)} = \frac{(G_1(v_1+1)t^2\varepsilon^*(G_1(2v_2t^2-t^2-1) - G_2(2v_2-1)(t^2-1)))/}{(G_1^2(v_1+1)t^2(2v_2t^2-t^2-1) - G_2G_1(t^2-1)(v_1(4v_2+1)t^2 + v_2(t^2-1) - 2t^2-1) + G_2^2(2v_1-1)(v_2+1)(t^2-1)^2)} \quad (\text{A4.11})$$

## A5. Solution for Marks-Yoffe disclination in two-phase spheroid

$$B_I = \frac{(2\chi(G_1(v_1+1)(v_2(4t^3-1) - 2t^3-1)(v_1(2\log(tR_s)+1) - \log(tR_s) - 1) - G_2(2v_1-1)(v_2+1)(v_1((4t^3-1)\log(tR_s) - 3\log(R_s) + 2t^3-2) - (2t^3+1)\log(tR_s) + 3\log(R_s) - 2t^3+2)))/}{(3(v_1-1)(2G_2(2v_1-1)(v_2+1)(t^3-1) - G_1(v_1+1)(v_2(4t^3-1) - 2t^3-1)))} \quad (\text{A5.1})$$

$$\begin{aligned}
B_2 = & -(2 \chi (G_1 (\nu_1 + 1) (\nu_2^2 (8 t^3 \log(t R_\zeta) - 2 \log(R_\zeta) + 4 t^3 - 1) - \nu_2 (2 t^3 (4 \log(t R_\zeta) + 3) + \log(R_\zeta)) + \\
& 2 t^3 \log(t R_\zeta) + \log(R_\zeta) + 2 t^3 + 1) - 2 G_2 (2 \nu_1 - 1) (\nu_2 + 1) \\
& (\nu_2 (2 t^3 \log(t R_\zeta) - 2 \log(R_\zeta) + t^3 - 1) + t^3 (-\log(t R_\zeta)) + \log(R_\zeta) - t^3 + 1))) / \\
& (3 (\nu_2 - 1) (G_1 (\nu_1 + 1) (\nu_2 (4 t^3 - 1) - 2 t^3 - 1) - 2 G_2 (2 \nu_1 - 1) (\nu_2 + 1) (t^3 - 1)))
\end{aligned} \tag{A5.2}$$

$$C_1 = 0 \tag{A5.3}$$

$$C_2 = \frac{2 (\nu_2 + 1) t^3 \chi (G_2 (2 \nu_1 - 1) (\nu_2 + 1) - G_1 (\nu_1 + 1) (2 \nu_2 - 1)) R_\zeta^3 \log(t)}{3 (\nu_2 - 1) (G_1 (\nu_1 + 1) (\nu_2 (4 t^3 - 1) - 2 t^3 - 1) - 2 G_2 (2 \nu_1 - 1) (\nu_2 + 1) (t^3 - 1))} \tag{A5.4}$$

## **PUBLICATIONS**

# CURRICULUM VITAE

## Leonid Dorogin

### General data

Date and place of birth: 08.11.1984, Leningrad, USSR  
Citizenship: Russian Federation  
Address: Institute of Physics, University of Tartu, Riia 142, 51014,  
Tartu, Estonia  
Telephone: +372 56 292482  
E-mail: dorogin@ut.ee

### Education

- 2001–2005 Student of Physics Department at St. Petersburg State University (Russia). Degree: Bachelor of Physics with Excellence. Thesis in Statistical Physics “Surface scattering in resistance of thin conductive films”. Thesis advisor Prof. A. E. Kuchma (Physics Department at St. Petersburg State University).
- 2005–2008 Graduate student of Physics Department at St. Petersburg State University (Russia). Degree: Master of Physics. Thesis in Solid State Physics “Formation of mismatched layers in pentagonal nanoparticles”. Thesis advisor Prof. A. E. Romanov (Institute of Physics, University of Tartu, Estonia and Ioffe Physico-Technical Institute, Russian Academy of Sciences, St. Petersburg).
- 2008–2012 PhD student in Materials Science in the Faculty of Science and Technology at University of Tartu (Estonia). Thesis advisors Dr. Ilmar Kink and Prof. A. E. Romanov.

### Professional development

- 2012 “PhD Winter School in Nano Tribology” (Technical University of Denmark)

# ELULOOKIRJELDUS

## Leonid Dorogin

### Üldandmed

Sünniaeg ja koht: 08.11.1984, Leningrad, NSVL  
Kodakondsus: Venemaa  
Kontaktandmed: Tartu Ülikooli Füüsika Instituut, Riia 142,  
51014, Tartu, Eesti  
Telefon: +372 56292482  
E-mail: dorogin@ut.ee

### Haridus

- 2001–2005 Üliõpilane Peterburi Riikliku Ülikooli (Venemaa) füüsika osakonnas. Kraad: Füüsika bakalaureus, *cum laude*. Lõputöö statistilistes füüsikas “Surface scattering in resistance of thin conductive films”, juuli 2005. Juhendaja prof. A. E. Kutšma (Füüsika osakond, Peterburi Riiklik Ülikool).
- 2005–2008 Kraadiõppur Peterburi Riikliku Ülikooli (Venemaa) füüsika osakonnas. Kraad: Füüsikamagister. Lõputöö tahkisefüüsikas “Formation of mismatched layers in pentagonal nanoparticles”. Juhendaja prof. A. E. Romanov (Füüsika Instituut, Tartu Ülikool, Eesti ja Ioffe füüsikalise-tehniline Instituut, Vene Teaduste Akadeemia, Peterburg).
- 2008–2012 Materjaliteaduse doktorant Tartu Ülikooli Teaduse ja Tehnoloogia teaduskonnas (Eesti). Lõputöö juhendajad dr. Ilmar Kink ja prof. A. E. Romanov.

### Erialane enesetäiendus

- 2012 Talvekool “PhD Winter School in Nano Tribology” (Technical University of Denmark)

## DISSERTATIONES SCIENTIAE MATERIALIS UNIVERSITATIS TARTUENSIS

1. **Martin Järvekülg.** Tubular microstructures by Hf-, Zr- and Ti-butoxide gel sheet rolling. Tartu, 2011, 112 p.
2. **Sergei Vlassov.** Investigation of nanoscale interactions and mechanical properties of nanostructures using quartz tuning fork based real-time measurements. Tartu, 2011, 171 p.
3. **Margus Kodu.** Pulsed Laser Deposition of Magnesium Oxide and Barium Ternary Oxides for Plasma Display Protective Layers. Tartu, 2011, 89 p.
4. **Rainer Pärna.** Surface studies of some oxide films. Tartu, 2011, 129 p.
5. **Jevgeni Šulga.** Self-assembly and interaction of nanostructures. Tartu, 2011, 114 p.
6. **Wojciech Kuznik.** Quantum-chemical computer simulations of the linear and non-linear optical properties of pyrazoloquinoline and dicyanopyrazine derivatives. Tartu, 2012, 89 p.